NOVEL MULTI-BAND METAMATERIALS IN MICROWAVE REGION WITH APPLICATIONS IN ANTENNAS

A THESIS SUBMITTED TO
THE GRADUATE SCHOOL OF NATURAL AND APPLIED SCIENCES
OF
MIDDLE EAST TECHNICAL UNIVERSITY

BY

ÖZNUR KÜÇÜKSARI

IN PARTIAL FULFILLMENT OF THE REQUIREMENTS
FOR
THE DEGREE OF DOCTOR OF PHILOSOPHY
IN
ELECTRICAL AND ELECTRONICS ENGINEERING

JULY 2014

Approval of the Thesis:

NOVEL MULTI-BAND METAMATERIALS IN MICROWAVE REGION WITH APPLICATIONS IN ANTENNAS

submitted by **ÖZNUR KÜÇÜKSARI** in partial fulfillment of the requirements for the degree of **Doctor of Philosophy in Electrical and Electronics Engineering Department, Middle East Technical University** by,

Prof. Dr. Canan Özgen
Dean, Graduate School of **Natural and Applied Sciences** ____________

Prof. Dr. Gönül Turhan Sayan
Head of Department, **Electrical and Electronics Engineering** ____________

Prof. Dr. Gönül Turhan Sayan
Supervisor, **Electrical and Electronics Engineering Dept., METU** ____________

Examining Committee Members

Prof. Dr. Mustafa Kuzuoğlu
Electrical and Electronics Engineering Dept., METU ________________

Prof. Dr. Gönül Turhan Sayan
Electrical and Electronics Engineering Dept., METU ________________

Prof. Dr. Gülbin Dural
Electrical and Electronics Engineering Dept., METU ________________

Assist. Prof. Dr. Özgür Ergül
Electrical and Electronics Engineering Dept., METU ________________

Assoc. Prof. Dr.Asım Egemen Yılmaz
Electronics Engineering Dept., Ankara University ________________

Date: 31.07.2014

I hereby declare that all information in this document has been obtained and presented in accordance with academic rules and ethical conduct. I also declare that, as required by these rules and conduct, I have fully cited and referenced all material and results that are not original to this work.

Name, Last Name : Öznur Küçüksarı

Signature :

ABSTRACT

NOVEL MULTI-BAND METAMATERIALS IN MICROWAVE REGION WITH APPLICATIONS IN ANTENNAS

Küçüksarı, Öznur
Ph.D., Department of Electrical and Electronics Engineering
Supervisor: Prof. Dr. Gönül Turhan Sayan

July 2014, 176 pages

This dissertation is focused on the design, fabrication, and characterization of multi-band metamaterials in microwave region with novel applications in antennas with the following outcomes:

In the first part of dissertation, important concepts that have to be considered during the design, simulation and characterization of planar metamaterial arrays are investigated. All investigations are performed using the planar dual band nested U-ring resonator (2-NURR) metamaterial array that is a novel exemplar of the planar metamaterial arrays. First, effects of different electromagnetic excitation types on the behavior of planar 2-NURR metamaterial array are examined. Then, the effects of using different boundary conditions and different computational volume dimensions in numerical simulations of periodic planar 2-NURR metamaterial arrays are investigated. Next, the commonly used parameter retrieval methods are reviewed with a special focus on the widely used Nicholson-Ross-Weir (NRW) algorithm. Finally, the important shortcomings of NRW algorithm are demonstrated for dense metamaterial arrays.

In the second part of dissertation, the M-band nested split ring resonator (M-NSRR) having a small and geometrically simple unit cell is introduced as a novel multi-band MNG type metamaterial. Then, design and simulation procedures, fabrication and measurement processes for the M-band nested U-ring resonator (M-NURR) are given as the modified simpler version of the M-NSRR topology. Next, the single-sided and double-sided (in broadside-coupled configuration) versions of the M-NURR are demonstrated on a comparative basis for further miniaturization of the M-NURR topologies. At the end of this part, performances of nested ring resonators with different topologies are compared.

In the last part of dissertation, metamaterial-inspired electrically small, single-, dual- and triple-band antennas with steerable radiation patterns and high radiation efficiencies at the GSM (1.93-1.99GHz), ISM (2.43-2.4835GHz), and WIMAX (3.3-3.6GHz) frequencies are introduced. First, performance characteristics of these single-band and multi-band antennas are investigated numerically. Then, three different single band antennas having their maximum directivities in the vertical, diagonal and horizontal directions at the GSM (1.93-1.99GHz) frequencies are fabricated as the exemplars of the antennas with steerable radiation pattern and experimental results from these antennas are reported. Finally, experimental results for fabricated dual- and triple-band antennas having their maximum directivities in the vertical directions are demonstrated as examples to multi-band metamaterial antenna applications.

Keywords: multi-band metamaterials, nested U-ring resonators, nested split ring resonators, retrieval methods, metamaterial-inspired antennas, electrically small antennas, multi-band antennas.

ÖZ

MİKRODALGA BÖLGESİNDE ÇALIŞAN ÖZGÜN ÇOK-BANTLI METAMALZEMELER VE ANTEN UYGULAMALARI

Küçüksarı, Öznur
Doktora, Elektrik ve Elektronik Mühendisliği Bölümü
Tez Yöneticisi: Prof. Dr. Gönül Turhan Sayan

Temmuz 2014, 176 sayfa

Bu tez mikrodalga frekanslarında çalışan çok bantlı metamalzemelerin tasarımı, üretimi ve karakterizasyonu üzerinde yoğunlaşmış olup, tasarlanan metamalzemeler özgün anten tasarımlarına uygulanmış ve aşağıda sıralanan sonuçlar elde edilmiştir:

Tezin ilk kısmında, düzlemsel metamalzeme dizilerinin tasarımı, benzetimi ve karakterizasyonu için gerekli olan önemli kavramlar incelenmiştir. Tüm incelemeler düzlemsel metamalzeme dizilerinin özgün bir örneği olan ve iki frekans bandında çalışan iç içe geçmiş U halkalı rezonatörlerden oluşan metamalzeme (2-NURR) dizisi kullanılarak gerçekleştirilmiştir. İlk olarak değişik elektromanyetik uyarım çeşitlerinin düzlemsel 2-NURR metamalzeme dizilerinin davranışı üzerindeki etkisi araştırılmıştır. Daha sonra değişik sınır koşullarının ve değişik hesaplama hacim boyutlarının periyodik düzlemsel 2-NURR metamalzeme dizilerinin sayısal benzetimine etkileri incelenmiştir. Ardından, yaygın olarak kullanılan parametre çıkarım yöntemleri, Nicholson-Ross-Weir (NRW) algoritması üzerinde odaklanılarak, gözden geçirilmiştir. Son olarak, NRW yönteminin sık metamalzeme dizilerine uygulanması durumunda ortaya çıkan önemli zafiyetler gösterilmiştir.

Tezin ikinci kısmında, çok bantlı özgün bir MNG tipi metamalzeme olan, küçük ve geometrik olarak basit birim hücre yapısına sahip, M tane frekans bandında çalışan, iç içe geçmiş yarıklı halkalı rezonatör (M-NSRR) yapısı önerilmiş ve sayısal olarak incelenmiştir. Daha sonra M-NSRR yapısının daha basit bir çeşidi olan iç içe geçmiş U halkalı rezonatör (M-NURR)'ün benzetim yöntemleri, üretim ve ölçüm basamakları verilmiştir. Ardından, M-NURR yapısını daha fazla küçültmek için M-NURR yapısının tek taraflı ve çift taraflı (düzleme dik bağlaşmış şekilde) durumları karşılaştırılmalı olarak gösterilmiştir. Bu kısmın sonunda, değişik şekillerdeki iç içe geçmiş halkalardan oluşan rezonatörlerin performansları karşılaştırılmıştır.

Tezin son kısmında, GSM (1.93-1.99GHz), ISM (2.43-2.4835GHz), ve WIMAX (3.3-3.6GHz) frekanslarında çalışan, metamalzemelerden esinlenen, elektriksel olarak küçük ve yönlendirilebilir yayılım örüntüsüne sahip bir, iki ve üç bantlı antenler gösterilmiştir. İlk olarak, bu antenlerin performans karakteristikleri sayısal olarak incelenmiştir. Daha sonra, yönlenmiş yayınım örüntüsüne sahip antenlere örnek olarak GSM (1.93-1.99GHz) frekansında çalışan ve maksimum yayınım yönü dikey, köşegen ve yatay konumda olan üç farklı anten üretilmiş ve bu antenler için ölçüm sonuçları rapor edilmiştir. Son olarak, çok bantlı çalışma frekansına sahip antenlere örnekleri olarak üretilmiş olan dikey konumda yayınım örüntüsüne sahip iki ve üç bantlı antenler için ölçüm sonuçları verilmiştir.

Anahtar Kelimeler: çok bantlı metamalzemeler, iç içe geçmiş yarıklı halkalı rezonatör, iç içe geçmiş U halkalı rezonatör, çıkarım yöntemleri, metamalzemelerden esinlenen antenler, elektriksel olarak küçük antenler, çok bantlı antenler.

to my dear brother Mustafa…

ACKNOWLEDGEMENTS

First and foremost, I would like to express my gratitude to my supervisor, Prof. Dr. Gönül Turhan Sayan for her endless support and prospective guidance throughout this dissertation. She has always been more than a supervisor, and this dissertation would not have been possible without her great and patient guidance. Words can never be enough to explain my gratitude to her.

I am extremely grateful to Prof. Dr. Richard W. Ziolkowski for his great academic and social support, motivation, friendly approach and encouragement throughout my studies in The University of Arizona, and for accepting me to The University of Arizona for 1 year and for his guidance about metamaterial inspired antennas which constitutes the 5^{th} chapter of this study. It was pleasure for me to work with him, and I feel very lucky to know him.

I would like to express my special thanks to Prof. Dr. Mustafa Kuzuoğlu, Prof. Dr. Adnan Köksal and Assoc. Prof. Dr. Asım Egemen Yılmaz for their valuable guidance and contributions throughout my dissertation progress meetings.

I also would like to utter my special thanks to Prof. Dr. Gülbin Dural, Prof. Dr. Özlem Aydın Çivi, and Assist. Prof. Dr. Özgür Ergül for being in my dissertation defense committee and for their contributions and to Prof. Dr. Sencer Koç and Prof. Dr. Şimşek Demir for their help in antenna measurements.

I also would like to thank my friends from the ECE department of The University of Arizona, Sawyer D. Campbell, Ning Zhu, Ryan Cutshall and Ming-Chun Tang for their help, support and friendship throughout my stay in Arizona.

Special thanks to Evren Ekmekçi, Hayrettin Yüzer, Ömer Bayraktar, Çağrı Çetintepe for sincerely sharing their experience and knowledge and helping me at any time without hesitation.

I feel really very lucky to have friends and colleagues like Reyhan Zengin, Yasemin Özkan Aydın, Aslıhan Anlar, Seda Kartal and İmren Yelmiş. Their sincere friendship has always been of great value to me. Many thanks to them.

I would like to thank Erdinç Yurdakul and Adem Ateş, the technicians in the Department of Engineering at METU, Şebnem Saygıner from ASELSAN for their help in fabrication and measurement processes.

Last but not least, I would like to thank every member of my dear families, Türkmen and Küçüksarı, for their invaluable support throughout the writing process of this dissertation. I would like to express my deepest gratitude to my lovely husband, Mehmet for always being with me and for his support to reach this point.

TABLE OF CONTENTS

LIST OF TABLES

TABLES

LIST OF FIGURES

FIGURES

CHAPTER 1

INTRODUCTION

Artificial materials having negative or near-zero values of permittivity and/or permeability over certain frequency bands are called metamaterials whose electromagnetic properties are quite different from natural materials. Backward-wave propagation, anti-parallel phase and group velocities, and negative refraction are observed for metamaterials when they have simultaneously negative values of permittivity and permeability. Metamaterials have drawn the attention of many researchers due to these unusual properties which possibly make them candidate structures not only for use in the improvement of present devices but also for the development of new devices and the design of new systems.

The earliest study known in the area of metamaterials was a completely theoretical work done by Veselago in late 1960's [1]. In this study, he stated the possibility of having negative index of refraction (i.e. simultaneous values of negative permittivity and permeability parameters) for anisotropic materials. He also stated that phenomena such as refraction, Doppler effect and Cherenkov radiation have different characteristics in negative index materials as compared to natural materials. For thirty years after Veselago's pioneering study, there had been no considerable interest in metamaterials.

There had been some efforts to obtain negative real permittivity in metallic structures in microwave region since nineties [2-5]. Plasma-like effects in 3D wire mesh photonic crystals were studied by Sievenpiper et al. in 1996 [2] and in 1998 [4] and it was reported that these structures could have negative permittivity at microwave frequencies. The negative effective permittivity (i.e. ε-negative (ENG) medium) was realized below plasma frequency using a periodic array of thin gold plated tungsten wires which is also known as wire media by Pendry et al. in 1998 [5].

On the other hand, to the best of our knowledge, first observation of negative permeability was made by Lagarkov et al. using two-element bi-helix particle in 1997 [6]. Another well-known study which is commonly referred as the first realization of structures having an effective negative permeability (i.e. μ-negative (MNG) medium) was performed by Pendry et al. They reported effective negative permeability function below magnetic plasma frequency using nonmagnetic conducting sheets in 1999 [7]. In accordance with this study, MNG structures can be constructed with conductors shaped into split rings. The planar version of split rings as well as the Swiss roll topology are also proposed in this study.

A double negative (DNG) metamaterial having simultaneously negative effective permittivity and negative effective permeability was designed and experimentally verified for the first time by combining the wire media and the planar split ring resonator (SRR) structure in 2000 [8]. In this study, negative refractive index was obtained over a narrow frequency band which is the cross-section of ENG band of the wire media and MNG band of the planar split ring structure. After this initial experiment on DNG metamaterials, two further basic experiments reported in [9] and [10], are performed. The presence of negative refraction are directly verified by measuring the deflection of a beam of microwave radiation from prism-shaped sample in [10].

After realization of negative refractive index, researchers turned their attention to explaining different aspects of metamaterials by theoretical [11-15], numerical and experimental studies [16-18] in microwave frequencies and in terahertz frequencies [19-24]. Various types of ENG [25-29], MNG [30-54] and DNG [55-81] metamaterials have been studied. Single-negative (i.e. MNG or ENG) and double-negative (DNG) as well as μ-near-zero (MNZ) and ε-near-zero (ENZ) metamaterials are found useful in many applications including absorbers [82-95], miniaturized antennas with high directivities or improved efficiencies [96-115], cloaking devices [116-130], lenses [131-152], etc.

This dissertation is focused on the design, fabrication, and characterization of multi-band metamaterials in microwave region. Novel electrically small and highly efficient multi-band antennas with steerable radiation patterns are also demonstrated as applications of the proposed multi-band metamaterials.

1.1 Brief Summary of the Topics Studied in This Dissertation

Brief summary of the novel topics studied in this dissertation are given in this section.

1.1.1 Effects of Boundary Conditions and Computational Domain Dimensions in Metamaterial Simulations

In general, metamaterials are designed as periodic arrays of sub-wavelength unit cells to realize unusual electromagnetic properties such as negative values for permittivity and/or permeability over certain frequency bands [1, 8, 10]. Such properties are determined not only by a specific metamaterial unit cell design but also by electromagnetic coupling effects between array elements [35, 153-156]. It is a common practice to analyze metamaterial arrays using numerical techniques prior to fabrication and experimental characterization. Use of commercial electromagnetic full-wave solvers such as CST Microwave Studio (MWS) [157] is found practical especially when a large periodic metamaterial array is to be simulated. During this computational procedure, an infinitely large metamaterial array can be simulated instead, as a good approximation, by using proper boundary conditions imposed at the boundaries of a finite sized computational volume that contains a representative metamaterial unit cell.

Periodic boundary conditions as well as perfect electric conductor (PEC) type or perfect magnetic conductor (PMC) type boundary conditions are frequently implemented in the simulations of periodic metamaterial arrays. Type of the boundary conditions should be selected carefully to simulate the intended metamaterial array topology that is compatible with real-life scenarios of applications and/or measurement set-ups to be realized. This issue is important particularly when the metamaterial unit cell has a structural asymmetry with respect to the boundaries.

Furthermore, dimensions of the computational volume determine the spatial periods for the simulated metamaterial array, which affect the level of electromagnetic coupling between array elements. Importance of these issues will be demonstrated in detail in section 3.2 by carefully designed numerical simulations.

1.1.2 Effects of Having Dense Metamaterial Arrays on the Retrieved Effective Parameters Obtained by the NRW method

Electromagnetic constitutive parameters of metamaterials cannot be measured directly but retrieved numerically using several different methods such as those based on the averages of the fields inside the metamaterial [158-160], parameter fitting to dispersive models [161], use of simulated or measured complex scattering parameters, S11 and S21 [15, 162-174].

It is very common in metamaterial literature to use the simple homogenization procedure based on the so called Nicholson-Ross-Weir (NRW) algorithm for parameter retrieval using simulated or measured complex scattering parameters. In this method, an array of resonant unit cells (i.e. a slab of metamaterial) is treated as a slab of a homogeneous material. Then, the refractive index, impedance, effective permeability and effective permittivity parameters of this homogeneous metamaterial slab are retrieved using the complex valued transmission and reflection spectra (i.e. S11 and S21) [162-167] under the assumption of a normally incident uniform plane wave excitation.

In order to run this algorithm, scattering parameters are needed, which can be computed easily by using electromagnetic full wave solvers such as ANSOFT HFSS or CST MWS. Although implementation of this parameter retrieval algorithm is relatively easy and straightforward, unphysical results such as the “anti-resonant effects” (i.e. the presence of negative imaginary part for permittivity which contradicts with the “passivity” requirement under the $e^{-i\omega t}$ convention) have been observed in the retrieved parameters [175-179]. Importance of spatial dispersion and magnetoelectric coupling effects for a trustable metamaterial homogenization procedure have been discussed especially for densely packed arrays [180].

In section 3.3, the commonly used NRW retrieval algorithm and its improved versions will be reviewed and the questionable issues about this algorithm will be discussed. The effect of structural periodicity (i.e. spatial dispersion effects) of a metamaterial array on the strength of anti-resonant phenomenon will be investigated using the parameter retrieval approach based on the NRW method and Kramers Kronig (K-K) relation [15]. The real parts of the permittivity and permeability will be calculated from the retrieved imaginary parts for varying periodicity values (along the applied magnetic field direction) using the K-K relation to check for the condition of “causality”.

1.1.3 Design of Novel Multi-Band Metamaterials: Nested Ring Resonators

It has been demonstrated that design of conventional SRR or spiral resonator (SR) unit cells with increased number of rings (or turns) helps to realize considerable amounts of miniaturization, however, the resulting metamaterial structures still display the single-band MNG behavior [31]. Compact multi-band MNG unit cells can be designed by using metallic inclusions having more complicated geometries as compared to the conventional SRR or SR structures [37, 181-185]. Or alternatively, MNG topologies resonating at two or three different frequencies can be designed by using periodic arrays of super cells, which are composed of two or more slightly different or asymmetrical individual unit cell structures [35, 186-188]. Multi-band metamaterials are obtained by these approaches in the expense of either increased electrical size or increased structural complexity. In metamaterial design, having small electrical size is important not only for miniaturization concern but also to satisfy the conditions for the effective medium approach. Simplicity of the unit cell geometry is another design requirement needed for lower fabrication errors especially at shorter wavelengths of terahertz regime.

1.1.3.1 M-Band Nested Split Ring Resonators (M-NSRR)

In section 4.2, the M-band nested split ring resonator (M-NSRR) topologies having a small and geometrically simple unit cell will be introduced and investigated numerically as a multi-band MNG type metamaterial in microwave regime. Single (1-NSRR), dual (2-NSRR), and triple (3-NSRR) band nested SRRs are presented in Figure 1.1 as the examplers of the introduced M-NSRR topologies.

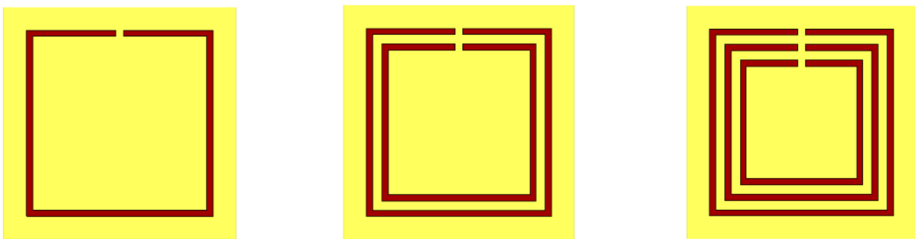

(a) **(b)** **(c)**

Figure 1.1: Single, dual, and triple band nested split ring resonators: **(a)** 1-NSRR. **(b)** 2-NSRR. **(c)** 3-NSRR.

1.1.3.2 M-Band Nested U-Ring Resonators (M-NURR)

The *M*-band nested U-ring resonator (M-NURR) will be introduced in section 4.3 as the modified simpler version of the M-NSRR topology. Design, simulation procedures, fabrication and measurement processes for the symmetrical single (1-NURR), dual (2-NURR) and triple (3-NURR) band nested U-ring resonators will be given in detail. The asymmetrical 3-NURR unit cell and the 3-NURR with merged frequencies will also be introduced for the purpose of showing the controllability of the resonance frequencies individually and also for the purpose of enhancing the MNG bandwidth, respectively. The symmetrical 3-NURR, asymmetrical 3-NURR and 3-NURR with merged frequencies are presented in Figure 1.2 as the exemplars of these M-NURR topologies.

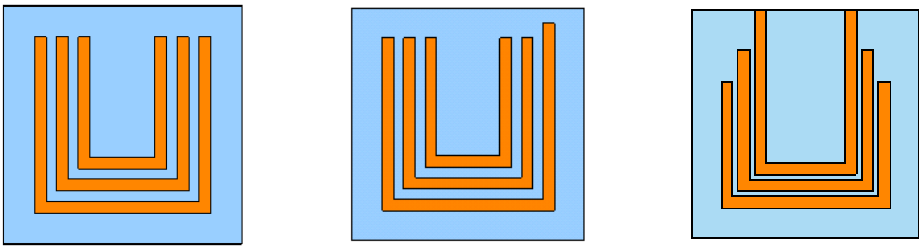

(a) **(b)** **(c)**

Figure 1.2: Three different 3-NURR unit cells. **(a)** Symmetrical 3-NURR **(b)** asymmetrical 3-NURR (c) 3-NURR with merged frequencies.

1.1.3.3 Further Miniaturization of U-Shaped Multi-Band Metamaterial Structures

Transmission characteristics of single-sided and double-sided (in broadside-coupled configuration) versions of *M*-NURR presented in Figure 1.3 will be investigated on a comparative basis for the purpose of improved miniaturization in Section 4.4. Transmission spectra (i.e. $|S_{21}|$ versus frequency curves) of both single and double sided *M*-NURR topologies will be computed by CST Microwave Studio for the special cases of unit cells with single ring (1-NURR) and double concentric rings (2-NURR). The comparison of the electrical sizes of these *M*-NURR topologies will be presented in detail.

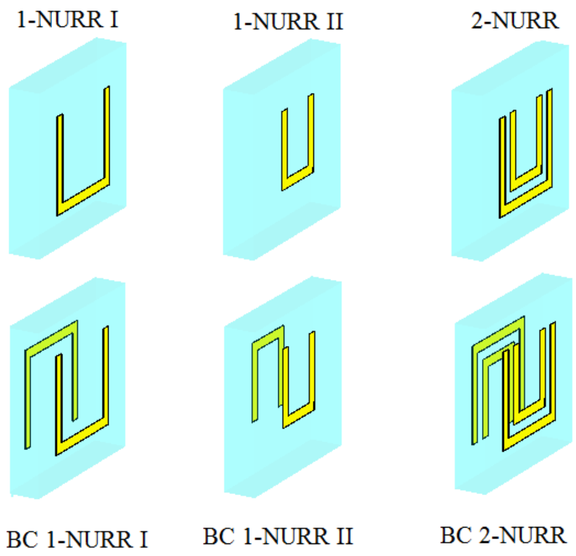

Figure 1.3 : Single-sided and double-sided (in broadside-coupled (BC) configuration) versions of simulated *M*-NURR.

1.1.4 Single-, Dual- and Triple-Band Electrically Small Metamaterial Antennas

Metamaterial-inspired electrically small, single-, dual- and triple-band antennas with steerable radiation patterns and high radiation efficiencies at the GSM (1.93-1.99GHz), ISM (2.43-2.4835GHz), and WIMAX (3.3-3.6GHz) frequencies will be introduced in Chapter 5 with the help of the design concepts of nested ring resonators reported in Chapter 4. Performance characteristics of all antennas will be investigated numerically using a commercial full-wave electromagnetic solver (HFSS). Design, simulation procedures, fabrication and measurement processes for the reported antennas will be given in detail. The single, dual and triple band antennas having their maximum directivities in the vertical direction are presented in Figure 1.4 as the exemplars of these antennas.

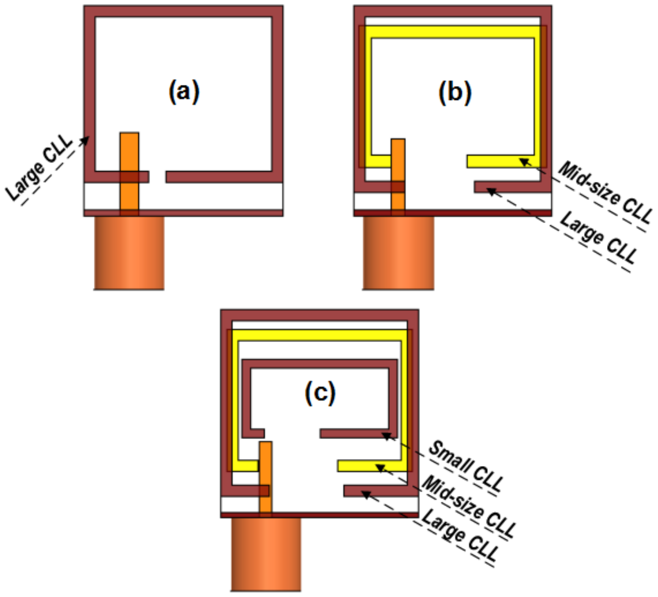

Figure 1.4 : (a) Single-band; **(b)** dual-band; and **(c)** triple-band antenna designs.

1.2 Novel Contributions of This Dissertation to Metamaterial Literature

In this dissertation, different aspects of metamaterials are studied with a particular focus on multi-band metamaterials with novel applications in antennas. Three journal papers [49, 189-190] and six conference papers [43-45, 115, 178, 191] are already published in well-known, SCI journals and international conferences as the outcomes of this dissertation. Three more journal papers are planned to be submitted to international journals based on the remaining novel results produced in this study. Chapters of this dissertation are organized using the already published papers by the permission of the co-authors of the papers.

Novel contributions of this dissertation to metamaterial literature are summarized as follows.

Effects of Boundary Conditions and Spatial Periodicity in Metamaterial Simulations in [189] and [191]:

- The effects of using different boundary conditions and different computational volume dimensions in numerical simulations of periodic metamaterial arrays are demonstrated.

- It is demonstrated that use of different boundary conditions may result in the simulation of dissimilar periodic array topologies with completely different electromagnetic responses especially in the case of unit cells having structural asymmetry with respect to the boundaries.

- It is also demonstrated that dimensions of the computational volume may strongly affect the overall response of the metamaterial structure due to varying electromagnetic coupling between the array elements.

Drawbacks of the NRW Parameter Retrieval Method in [178]:

- The parameter retrieval procedures in literature with a special focus on the widely used NRW retrieval method are reviewed.

- The effects of changing metamaterial array periodicity on the retrieved parameters are investigated to demonstrate the presence of unphysical results such as the "anti-resonant effects" (i.e. the presence of negative imaginary part for permittivity which contradicts with the "passivity" requirement under the $e^{-i\omega t}$ convention) produced by NRW retrieval method.

- The real part of the permittivity and permeability are also calculated from the retrieved imaginary parts for varying periodicity values along the applied magnetic field direction using the K-K relation to check for the condition of "causality".

- It is shown that as the metamaterial array becomes denser by reducing the periodicity, the conditions for passivity and causality are violated more strongly.

Multi-Band Metamaterials: Nested Ring Resonators in [43], [45] and [49]:

- Two novel MNG type multi-band metamaterial designs in microwave regime are introduced; an M-band nested split ring resonator (*M*-NSRR) and an *M*-band nested U-ring resonator (*M*-NURR).

- The proposed topologies have *M* nested and unconnected metal rings printed on a dielectric substrate.

- Single-, dual-, and triple-band versions of the *M*-NURR topology are fabricated and measured.

- It is shown that the number of magnetic resonances can easily be adjusted by the number of concentric rings.

- It is also shown that proposed *M*-NSRR and *M*-NURR are electrically small multi-band metamaterial structures as compared to the alternative supercell structures.

- Results reveal that resonances of an M-NURR metamaterial can be adjusted almost independently and in a highly controllable manner.

- It is demonstrated that the 3-NURR with merged frequencies enhances the MNG bandwidth.

Miniaturization in [44]:

- Single-sided and double-sided (in broadside-coupled configuration) versions of the *M*-NURR are investigated on a comparative basis for the purpose of improved miniaturization.

- Results reveal that broadside-coupled (BC) *M*-NURR has much smaller resonance frequencies (hence considerably smaller electrical sizes) as compared to their single-sided counterparts.

Metamaterial-Inspired Antennas in [115] and [190]:

- Metamaterial-inspired electrically small multi-band antennas are proposed.

- These antennas are based on a coaxially-fed printed dipole integrated in a planar configuration with capacitively loaded loops (CLLs).

- Performance characteristics of the proposed antennas are investigated both numerically and experimentally.

- It is shown that the number of operating frequencies can easily be adjusted by the number of CLLs in the proposed antenna topology.

- It is also shown that all the proposed antennas provide simple and electrically small geometry as well as high radiation efficiencies, above 77 percent in simulations.

- Results reveal that radiation patterns can be steered to desired directions by simply adjusting the relative positions of the feed and the gap of the CLLs.

1.3 Organization of This Dissertation

Organization of the chapters of this dissertation is as follows:

In Chapter 2, fundamental concepts of metamaterials are outlined. First, the possibility of having materials with simultaneously negative-valued permittivity and permeability is discussed as originally predicted by Veselego in the 60's. Then, the metamaterial terminology commonly used in literature and in this dissertation is presented. Third, unique properties of negative index metamaterials such as backward-wave propagation, anti-parallel phase and group velocities, and negative refraction are discussed under uniform plane-wave excitation in a simple (i.e. linear, homogeneous, and isotropic) medium. Finally, design and realization aspects of canonical metamaterial topologies are briefly discussed.

In Chapter 3, important concepts that must be considered during the design, simulation and characterization of planar metamaterial arrays are investigated. All investigations are performed using the planar dual band nested U-ring resonator (2-NURR) metamaterial array that is a novel exemplar of the planar metamaterial arrays. First, effects of different electromagnetic excitation types on the behavior of planar 2-NURR metamaterial array are examined. Then, the effects of using different boundary conditions and different computational volume dimensions in numerical simulations of periodic planar 2-NURR metamaterial arrays are investigated. Next, the commonly used parameter retrieval methods are reviewed with a special focus on the widely used NRW algorithm. Finally, the important shortcomings of the NRW algorithm are demonstrated for dense metamaterial arrays.

In Chapter 4, the M-band nested split ring resonator (M-NSRR) having a small and geometrically simple unit cell is introduced as a novel multi-band MNG type metamaterial. Then, design and simulation procedures, fabrication and measurement processes for the M-band nested U-ring resonator (M-NURR) are given as the modified simpler version of the M-NSRR topology. Next, the single-sided and double-sided (in broadside-coupled configuration) versions of the M-NURR are demonstrated on a comparative basis for further miniaturization of the M-NURR topologies. At the end of this part, performances of nested ring resonators with different topologies are compared.

In Chapter 5, metamaterial-inspired electrically small, single-, dual- and triple-band antennas with steerable radiation patterns and high radiation efficiencies at the GSM (1.93-1.99GHz), ISM (2.43-2.4835GHz), and WIMAX (3.3-3.6GHz) frequencies are introduced. First, performance characteristics of these single-band and multi-band antennas are investigated numerically. Then, three different single-band antennas having their maximum directivities in the vertical, diagonal and horizontal directions at the GSM (1.93-1.99GHz) frequencies are fabricated as the exemplars of the antennas with steerable radiation pattern, and experimental results are reported for these antennas. Finally, experimental results for fabricated dual-band and triple-band antennas having their maximum directivities in the vertical directions are demonstrated as examples to multi-band metamaterial antenna applications.

In Chapter 6, overall conclusions are presented emphasizing the novel aspects of the dissertation outcomes. The chapter is concluded with a brief discussion on the future work.

CHAPTER 2

THEORY OF METAMATERIALS

In this chapter, fundamental concepts of metamaterials are outlined. First, the possibility of having materials with simultaneously negative-valued permittivity and permeability is discussed as originally predicted by Veselego in the 60's [1]. Then, the metamaterial terminology commonly used in literature and in this dissertation is presented. Third, unique properties of negative index metamaterials such as backward-wave propagation, anti-parallel phase and group velocities, and negative refraction are discussed under uniform plane-wave excitation in a simple (i.e. linear, homogeneous and isotropic) medium. Finally, design and realization aspects of canonical metamaterial topologies are briefly discussed.

2.1 Simultaneously Negative Values of Permittivity and Permeability Parameters: Predictions of Veselago

Solution of electromagnetic waves in a given medium is governed by the Maxwell's equations together with the constitutive relations which define the medium. When we consider a simple (i.e. linear, homogeneous, and isotropic) medium, for simplicity, permittivity $\varepsilon = \varepsilon_0\, \varepsilon_r$ and permeability $\mu = \mu_0\, \mu_r$ become simple constants where ε_0 and μ_0 are the permittivity and permeability of free space, respectively. The relative permittivity (ε_r) and the relative permeability (μ_r) are related to the refractive index (n) of the medium as

$$n = \sqrt{\varepsilon_r\, \mu_r} \tag{2.1}$$

For such a medium, the dispersion relation between the propagation constant (k) and the radian frequency ($\omega = 2\pi f$) is known to be

$$k^2 - \omega^2 \frac{n^2}{c^2} = 0 \tag{2.2}$$

The parameters n, ε and μ have real values for a lossless medium. It is clear that simultaneous change of the signs of ε and μ does not affect the relations (2.1) and (2.2). Therefore, it can be stated that wave propagation is still possible in a medium having $\varepsilon < 0$ and $\mu < 0$ simultaneously. However, as predicted by Veselago in 1964 [1], properties of electromagnetic waves in such media are different from the properties of waves propagating in media with positive ε and μ. Almost four decades after these initial predictions of Veselago, in late 90's, possibility of having negative-index media was demonstrated experimentally [8]. Since then, there has been an enormous and continuously growing interest of scientists in metamaterial related studies. Different terminologies have been established in the area of metamaterials by different researchers. Commonly used metamaterial terminology in literature and also throughout this dissertation is outlined in the following section.

2.2 Common Terminology Used in Metamaterial Studies

Materials can be classified according to the sign of their medium parameters as shown in Figure 2.1. Materials with negative permittivity are called ε-negative (ENG) materials while materials with negative permeability are called μ-negative (MNG) materials. When only one medium parameter has negative sign, such materials are called single negative (SNG) materials. Materials with ε or μ parameters being very close to zero are called zero index materials. The abbreviation ENZ stands for "permittivity near zero", and MNZ stands for "permeability near zero".

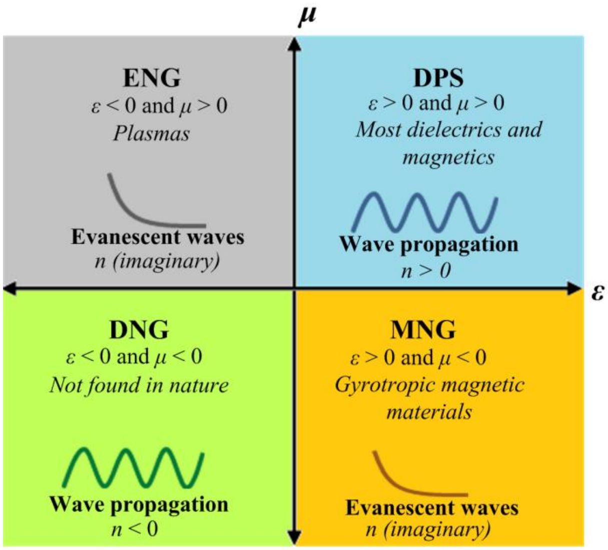

Figure 2.1: Material classification based on the signs of medium parameters ε and μ [192].

There are four possible sign combinations for ε and μ leading to four different classes of materials as summarized in Figure 2.1. Under the assumption of simple and lossless materials, media with $\varepsilon > 0$ and $\mu > 0$ are common materials found in nature and, dielectrics and magnetic materials are within this group. Wave propagation occurs in these media with parallel phase velocity and group velocity vectors. Such materials are called double positive (DPS) materials and they have positive real refractive index $n > 0$ as emphasized in Figure 2.1. Secondly, ENG materials with $\varepsilon < 0$ and $\mu > 0$ cannot support propagating waves; only evanescent waves occur in such media as the refractive index n is purely imaginary. Plasma medium is an example of ENG media. Another material group is composed of double negative (DNG) materials having $\varepsilon < 0$ and $\mu < 0$ simultaneously. The refractive index n is negative for DNG materials. Although such materials are not naturally found in nature, they can be constructed artificially. Wave propagation in a DNG material has unusual properties; having antiparallel phase and group velocities and negative refraction are perhaps the most striking differences. The last group is composed of materials with $\varepsilon > 0$ and $\mu < 0$ which are called MNG materials. Gyrotropic magnetic materials are examples for this group. Similar to the case of ENG materials, the refractive index n is purely imaginary for MNG materials under the assumption that ε and μ are real valued. Therefore, wave propagation is not supported in MNG media.

Some of the alternative terminology used for double-negative (DNG) materials are left-handed medium (LHM), negative-index materials (NIM), backward-wave (BW) media and negative-phase-velocity (NPV) media [192-194]. In this dissertation, the terms DNG, ENG, MNG, ENZ and MNZ metamaterials are preferred for metamaterial classes and DPS material is used for common materials with positive permittivity and permeability.

Unusual properties of wave propagation in DNG metamaterials are outlined in the next section.

2.3 Properties of DNG Metamaterials: Backward-Wave Propagation, Anti-Parallel Phase and Group Velocities, and Negative Refraction

In this section, unique properties of DNG metamaterials such as backward-wave propagation, anti-parallel phase and group velocities, and negative refraction are presented by starting with Maxwell's equations.

The most general form of time-domain Maxwell's equations for an arbitrary medium are stated as follows [192]:

$$\nabla \times \overline{\mathcal{E}} = -\frac{\partial \overline{\mathcal{B}}}{\partial t} \qquad \text{(Faraday's Law)} \tag{2.3}$$

$$\nabla \times \overline{\mathcal{H}} = \frac{\partial \overline{\mathcal{D}}}{\partial t} + \bar{\mathcal{J}} \qquad \text{(Ampere's Law)} \tag{2.4}$$

$$\nabla \cdot \overline{\mathcal{D}} = \rho_{\mathcal{V}} \qquad \text{(Gauss' Law)} \tag{2.5}$$

$$\nabla \cdot \overline{\mathcal{B}} = 0 \qquad \text{(Conservation of magnetic flux)} \tag{2.6}$$

In the above, $\overline{\mathcal{E}}$ (V/m) and $\overline{\mathcal{H}}$ (A/m) are the electric and magnetic field intensity vectors, respectively, $\overline{\mathcal{B}}$ (Weber/m^2) and $\overline{\mathcal{D}}$ (C/m^2) are the magnetic flux density and displacement vectors, respectively. In addition, $\bar{\mathcal{J}}$ (A/m^2) is free volume current density and ρ_v (C/m^3) is free volume charge density.

Also, the continuity equation is expressed as

$$\nabla \cdot \bar{\mathcal{J}} = -\frac{\partial \rho_v}{\partial t} \qquad \text{(Conservation of charge)} \qquad (2.7)$$

When time dependence $e^{j\omega t}$ is adopted for phasor domain representations, the relation between a generic time harmonic field $\overline{\mathcal{F}}(\bar{r}, t)$ and its phasor domain representation $\bar{F}(\bar{r})$ can be expressed as given

$$\overline{\mathcal{F}}(\bar{r}, t) = Re\{\bar{F}(\bar{r})\, e^{j\omega t}\} \qquad (2.8)$$

For monochromatic fields, Maxwell's equations and continuity equation given in equations 2.3 through 2.7 are expressed in phasor domain as

$$\nabla \times \bar{E} = -j\omega \bar{B} \qquad (2.9)$$

$$\nabla \times \bar{H} = j\omega \bar{D} + \bar{J} \qquad (2.10)$$

$$\nabla . \bar{D} = \rho_v \qquad (2.11)$$

$$\nabla . \bar{B} = 0 \qquad (2.12)$$

$$\nabla . \bar{J} = -j\omega \rho_v \qquad (2.13)$$

Also, constitutive relations are simplified for a linear and nondispersive medium as follows:

$$\overline{D} = \varepsilon_0 \overline{E} + \overline{P} = \varepsilon_0(1+\chi_e)\,\overline{E} = \varepsilon_0\,\varepsilon_r\,\overline{E} = \varepsilon\,\overline{E} \tag{2.14}$$

$$\overline{B} = \mu_0 \overline{H} + \overline{M} = \mu_0\,(1+\chi_m)\,\overline{H} = \mu_0\,\mu_r\,\overline{H} = \mu\,\overline{H} \tag{2.15}$$

with

$$\varepsilon_r = 1 + \chi_e = \varepsilon' - j\,\varepsilon'' \qquad \text{(relative permittivity)} \tag{2.16}$$

$$\mu_r = 1 + \chi_m = \mu' - j\,\mu'' \qquad \text{(relative permeability)} \tag{2.17}$$

where $\overline{P}$ and $\overline{M}$ denote the polarization and magnetization vectors, respectively, while χ_e and χ_m denote the electric and magnetic susceptibilities.

In (2.16) and (2.17), complex valued ε_r and μ_r are expressed in terms of their real parts (ε' and μ') and imaginary parts (ε'' and μ'') where ε'' and μ'' are related to loss mechanisms, in general.

Backward wave propagation, and Antiparallel Phase and Group Velocities:

Using the Maxwell's curl type equations, it can be shown that the $\bar{E}$ and $\bar{H}$ fields of a uniform plane wave satisfy the following equations

$$\bar{k} \times \bar{E} = \omega\,\mu\,\bar{H} \tag{2.18}$$

$$\bar{k} \times \bar{H} = -\omega\,\varepsilon\,\bar{E} \tag{2.19}$$

in a double-positive (DPS) material. In a DNG metamaterial, however, equations (2.18) and (2.19) need to be written as

$$\bar{k} \times \bar{E} = -\omega\,|\mu|\,\bar{H} \tag{2.20}$$

$$\bar{k} \times \bar{H} = \omega\ |\varepsilon|\ \bar{E} \tag{2.21}$$

From equations 2.18-2.21, it is seen that $\bar{k}$, $\bar{E}$ and $\bar{H}$ build a right handed triad in the DPS material while they build a left handed triad in the DNG metamaterial. In other words, propagation vector $\bar{k}$ in the DPS and in the DNG material are in the opposite directions.

In both DPS and DNG media, the expression for complex Poynting's vector $\bar{S}$ is given as

$$\bar{S} = \bar{E} \times \bar{H}^* \tag{2.22}$$

From equations 2.18 and 2.19, the $\bar{E}$ and $\bar{H}$ fields can be expressed as

$$\bar{E} = \frac{-1}{\omega\ \varepsilon}\,\bar{k} \times \bar{H} \tag{2.23}$$

$$\bar{H} = \frac{1}{\omega\ \mu}\,\bar{k} \times \bar{E} \tag{2.24}$$

Substituting equations 2.23 and 2.24 into equation 2.22, the expression for complex Poynting's vector in DPS media is given as

$$\bar{S}_{DPS} \triangleq \bar{E} \times \bar{H}^* = \frac{-1}{\omega\ \varepsilon}\left(\bar{k} \times \bar{H}\right) \times \frac{1}{\omega\ \mu}\left(\bar{k} \times \bar{E}^*\right)$$

$$= \frac{-1}{\omega^2\ \mu\ \varepsilon}\left(\bar{k} \times \bar{H}\right) \times \left(\bar{k} \times \bar{E}^*\right) \tag{2.25}$$

Let $\bar{A} = \bar{k} \times \bar{H}$, $\bar{B} = \bar{k}$ and $\bar{C} = \bar{E}^*$. Using the vector triple product identity $\bar{A} \times (\bar{B} \times \bar{C}) = (\bar{A} \cdot \bar{C})\bar{B} - (\bar{A} \cdot \bar{B})\bar{C}$, equation 2.25 can be written as

$$\bar{S}_{DPS} \triangleq \bar{E} \times \bar{H}^{*} = \frac{-1}{\omega^2\ \mu\ \varepsilon}\ \left\{\left[\left(\bar{k} \times \bar{H}\right) \cdot \bar{E}^{*}\right]\bar{k} - \left[\left(\bar{k} \times \bar{H}\right) \cdot \bar{k}\right]\bar{E}^{*}\right\} \tag{2.26}$$

Since $\bar{k} \times \bar{H}$ is perpendicular to $\bar{k}$, $\left[\left(\bar{k} \times \bar{H}\right) \cdot \bar{k}\right]\ \bar{E}^{*}$ term in equation 2.26 becomes zero. Substituting equation 2.19 into equation 2.26, $\bar{S}_{DPS}$ can be written as

$$\bar{S}_{DPS} = \frac{1}{\omega\ \mu}\ \bar{k}\ |\bar{E}|^2 \tag{2.27}$$

Therefore the Poynting's vector $\bar{S}_{DPS}$ is in the same direction as the propagation vector $\bar{k}$ in DPS media. Similarly, from equations 2.20 and 2.21, the $\bar{E}$ and $\bar{H}$ fields in DNG media can be expressed as

$$\bar{E} = \frac{1}{\omega\ |\varepsilon|}\ \bar{k} \times \bar{H} \tag{2.28}$$

$$\bar{H} = \frac{-1}{\omega\ |\mu|}\ \bar{k} \times \bar{E} \tag{2.29}$$

Substituting 2.28 and 2.29 into 2.22, the expression for complex Poynting's vector in DNG media $\bar{S}_{DNG}$ can be expressed as

$$\bar{S}_{DNG} \triangleq \bar{E} \times \bar{H}^{*} = \frac{1}{\omega\ |\varepsilon|}\left(\bar{k} \times \bar{H}\right) \times \frac{-1}{\omega\ |\mu|}\left(\bar{k} \times \bar{E}^{*}\right)$$

$$= \frac{-1}{\omega^2\ |\mu|\ |\varepsilon|}\ \left\{\left[\left(\bar{k} \times \bar{H}\right) \cdot \bar{E}^{*}\right]\bar{k} - \left[\left(\bar{k} \times \bar{H}\right) \cdot \bar{k}\right]\bar{E}^{*}\right\} \tag{2.30}$$

Considering $(\bar{k} \times \bar{H}) \perp \bar{k}$ and using equation 2.21, $\bar{S}_{DNG}$ becomes

$$\bar{S}_{DNG} = \frac{-1}{\omega\ |\mu|}\ \bar{k}\ |\bar{E}|^2 \tag{2.31}$$

As seen equation 2.31, the Poynting's vector $\bar{S}_{DNG}$ is in the opposite direction to the propagation vector $\bar{k}$ in DNG media. It is also known that phase velocity is the same as the direction of propagation vector $\bar{k}$, group velocity however is parallel to the Poynting's vector $\bar{S}$ [192]. Phase velocity and group velocity are therefore opposite to each other (anti-parallel) in DNG media. This unusual phenomenon of having opposite directions for $\bar{k}$ and $\bar{S}$ is known as "backward wave propagation".

In summary, the propagation direction of phase fronts (i.e. the direction of propagation vector $\bar{k}$) and the direction of power flow (i.e. the direction of Poynting's vector $\bar{S}$) are opposite to each other (anti-parallel) in a DNG material as opposed to the case that $\bar{k} // \bar{S}$ which is normally observed in DPS media as summarized in Figure 2.2.

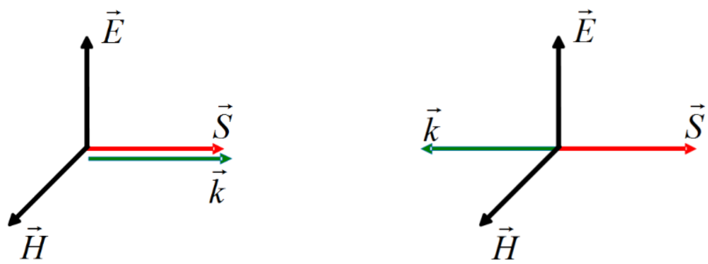

(a) (b)

Figure 2.2: Directions of the field vectors ($\bar{E}$ and $\bar{H}$), the propagation vector ($\bar{k}$) and the Poynting's vector $\bar{S}$ **(a)** in a DPS material, and **(b)** in a DNG metamaterial.

Negative Refraction:

Electromagnetic boundary conditions are expressed in their general form as follows:

$$\hat{n} \times (\bar{E}_2 - \bar{E}_1) = 0 \qquad (2.32)$$

$$\hat{n} \times (\bar{H}_2 - \bar{H}_1) = \bar{J} \qquad (2.33)$$

$$\hat{n} \, . \, (\bar{D}_2 - \bar{D}_1) = \rho \qquad (2.34)$$

$$\hat{n}\,.\,(\bar{B}_2 - \bar{B}_1) = 0 \tag{2.35}$$

where $\hat{n}$ is unit normal vector (pointing away from the first medium) at the boundary surface.

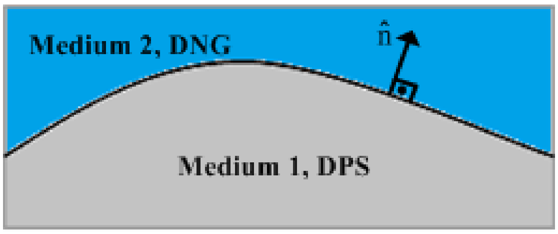

Figure 2.3: The interface between the DPS material (with ε_1 and μ_1) and the DNG metamaterial (with ε_2 and μ_2).

Considering an interface between a DPS medium and a DNG medium as shown in Figure 2.3, the boundary conditions can be applied in the absence of the sources ($\bar{J}$=0, ρ=0) as follows:

$$E_{1t} = E_{2t} \tag{2.36}$$

$$H_{1t} = H_{2t} \tag{2.37}$$

$$E_{1n} = -\frac{|\,\varepsilon_2\,|}{\varepsilon_1} E_{2n} \tag{2.38}$$

$$H_{1n} = -\frac{|\,\mu_2\,|}{\mu_1} H_{2n} \tag{2.39}$$

The refractive index of the DPS material is

$$n_1 = \sqrt{\varepsilon_{r1}\,\mu_{r1}} \tag{2.40}$$

Since $\varepsilon_{r2} < 0$ and $\mu_{r2} < 0$ for the DNG metamaterial, the refractive index of the DNG metamaterial will be

$$n_2 = \sqrt{\varepsilon_{r2}\, \mu_{r2}} = \sqrt{|\varepsilon_{r2}|\, e^{j\pi}\, |\mu_{r2}|\, e^{j\pi}} = -\sqrt{|\varepsilon_{r2}|}\, \sqrt{|\mu_{r2}|} \tag{2.41}$$

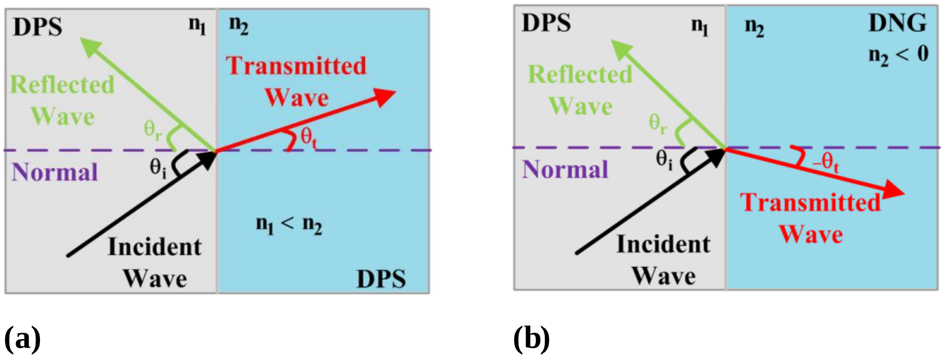

Figure 2.4: Incident, reflected and transmitted (refracted) waves at the boundary between **(a)** two DPS materials, **(b)** a DPS material and a DNG metamaterial.

Snell's Law of refraction is expressed, in general, as

$$n_1 sin\theta_i = n_2 sin\theta_t \tag{2.42}$$

in a DPS material with both n_1 and n_2 being positive.

Since the refractive index in the DNG metamaterial is negative, negative refraction occurs in the DNG metamaterial to satisfy Snell's Law as seen in Figure 2.4 and is justified mathematically as

$$|n_1| sin\theta_i = -|n_2| sin\theta_t = |n_2| sin(-\theta_t) \tag{2.43}$$

Since the design of DNG metamaterial is usually achieved by combining of ENG and MNG type metamaterial topologies [8], the next subsections will present the analysis, design and realization approaches for the canonical ENG, MNG, and DNG metamaterial structures.

2.4 Canonical ENG Metamaterials

In this section, we will outline the basic concepts behind the analysis, design, and realization of canonical ENG metamaterials.

A plasmon which is created by oscillation of free electrons in metals is a well-known example of ENG media. In the optical region of high frequencies ranging from the near-infrared to the visible and near ultraviolet, imaginary part of the permittivity of the plasmon becomes very small. In this region, permittivity of the metal is therefore approximately associated with a negative real number below the plasma frequency (ω_p) [195]. On the other hand, dissipation in the plasmon becomes dominant in the lower-frequency regions ranging from radio frequencies to far infrared frequencies and the permittivity of the metal becomes almost purely imaginary. In other words, metals do not have negative real permittivity in the lower-frequency region. Therefore, there have been some efforts to obtain negative real permittivity in metallic structures in microwave regime since nineties [2-5].

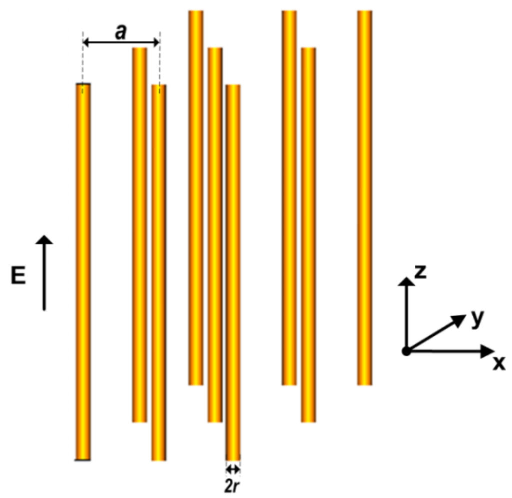

Figure 2.5: A periodic array of metallic thin wires to simulate the plasma effect [5].

Plasma-like effects in 3D wire mesh photonic crystals were studied by Sievenpiper et al. in 1996 [2] and in 1998 [4] and it was reported that these structures could have negative permittivity at microwave frequencies. The negative effective permittivity was realized below plasma frequency using a periodic array of thin gold plated tungsten wires (see Figure 2.5) by Pendry et al. [5] where the excitation field was polarized in the direction parallel to wires.

Effective relative permittivity of this medium can be expressed as [3,5]

$$\varepsilon_{eff} = 1 - \frac{{\omega_p}^2}{\omega\,(\,\omega + j\,\gamma\,)} \tag{2.44}$$

using the Drude model where ω_p and γ represent the plasma frequency and damping parameter, respectively. The plasma frequency (ω_p) can be computed in terms of the geometrical parameters of thin periodic lattice as

$${\omega_p}^2 = \frac{2\pi {c_0}^2}{a^2 \ln({}^{a}/_{r})} \tag{2.45}$$

where a and r are the lattice constant (i.e. array period) and the radius of the wire, respectively, while c_0 is the velocity of light in free space.

Considering the resistance of wires, the damping term (γ) can be expressed as

$$\gamma = \frac{\varepsilon_0\, a^2\, {\omega_p}^2}{\pi\, r^2\, \sigma} \tag{2.46}$$

where ε_0 and σ are the permittivity of free space and the conductivity of the metal, respectively. The real (${\varepsilon_{eff}}'$) and imaginary (${\varepsilon_{eff}}''$) parts of ε_{eff} can be expressed as

$$\varepsilon_{eff} = {\varepsilon_{eff}}' + j\,{\varepsilon_{eff}}'' = \underbrace{1 - \frac{{\omega_p}^2}{(\,\omega^2 + \gamma^2\,)}}_{{\varepsilon_{eff}}'} + j\underbrace{\frac{\gamma\,{\omega_p}^2}{\omega\,(\,\omega^2 + \gamma^2\,)}}_{{\varepsilon_{eff}}''} \tag{2.47}$$

using equation 2.46. Using the original dimensions of the wire array reported in [5], real $(\varepsilon_{eff}{}')$ and imaginary $(\varepsilon_{eff}{}'')$ parts of the effective permittivity are computed and plotted as shown in Figure 2.6.

As shown in Figure 2.6, real part of the effective permittivity has negative values below $\omega_p = 5.15 \text{ x } 10^{10} \mathrm{rad/s}$ (8.2 GHz). Values of the real and imaginary part of the permittivity vary as a function of frequency. In other words, the wire media is inherently a dispersive medium. Another observation is that the real part of effective permittivity converges to one and the imaginary part of effective permittivity converges to zero as we move to higher frequencies.

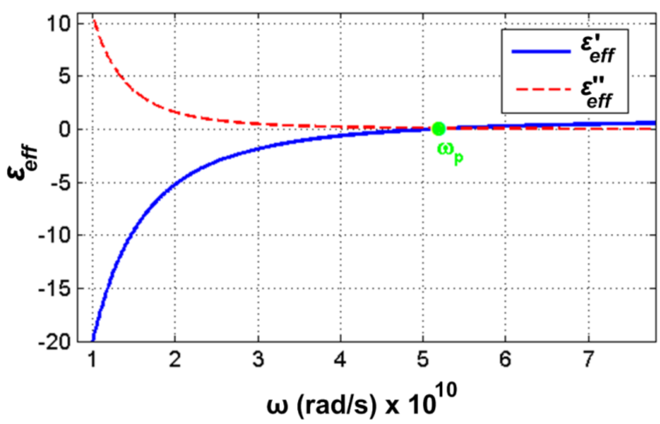

Figure 2.6: Real $(\varepsilon_{eff}{}')$ and imaginary $(\varepsilon_{eff}{}'')$ parts of the effective permittivity for the wire media reported in [5].

After the realization of negative permittivity using this wire media, further ENG metamaterials having various planar configurations have been proposed in microwave frequencies as shown in Figure 2.7. With the help of Babinet Principle, complementary split ring resonator (CSRR) is proposed as in Figure 2.7(a) [26]. Electric-LC (ELC) resonator and its miniaturized version [27], and ELC with two gaps [28] with the benefit of not requiring continuous current wires between the unit cells are designed to obtain negative permittivity as an alternative to the wire media as shown in Figure 2.7(b) through (d). I-shaped resonator and Z-shaped resonator topologies are also studied [29] as the transformed versions of the previously proposed ELC resonator as presented in Figure 2.7(e-f). It should be noted that such kinds of resonator topologies provide negative permittivity under proper excitation conditions.

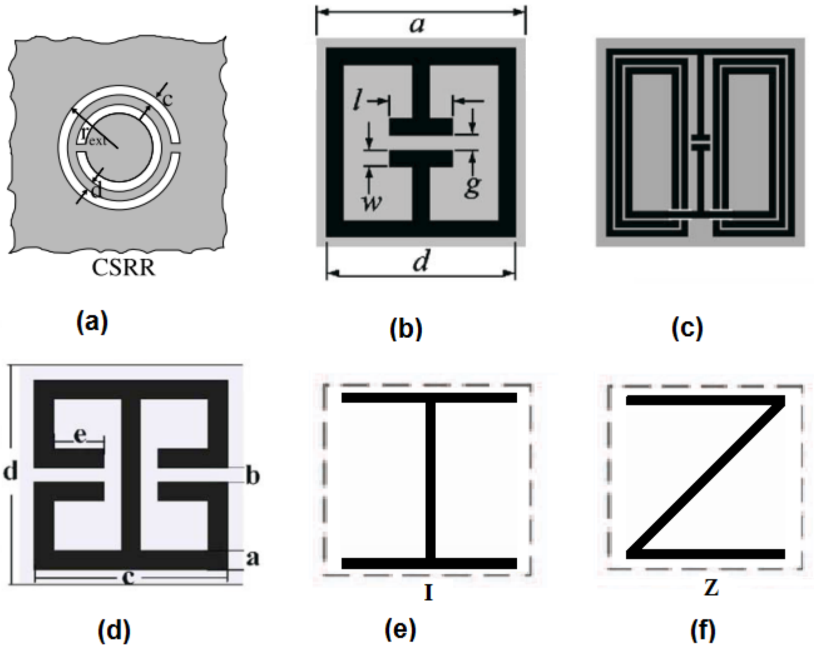

Figure 2.7: Electric resonators with negative permittivity: **(a)** CSRR [26], **(b)** ELC [27], **(c)** Miniaturized ELC [27], **(d)** ELC with two gaps [28], **(e)** I-shaped resonator [29], **(f)** Z-ELC resonator [29].

2.5 Canonical MNG Metamaterials

In this section, we will investigate the basic approaches for the analysis, design, and realization of MNG metamaterials.

It is known that negative permeability is not observed in nature. Due to this reason, researchers have tried to obtain artificial magnetic materials showing this unusual property. To the best of our knowledge, first observation of negative permeability was made by Lagarkov et al. using two-element bi-helix particle [6]. Another well-known study which is commonly referred as the first realization of structures having an effective negative permeability (i.e. μ-negative (MNG) metamaterials) was performed by Pendry et al. They reported effective negative permeability function below magnetic plasma frequency using nonmagnetic conducting sheets [7]. In accordance with this study, MNG structures can be constructed with conductors shaped into split rings. The planar version of split rings and the swiss roll topology are also proposed as shown in Figure 2.8 (a)-(c).

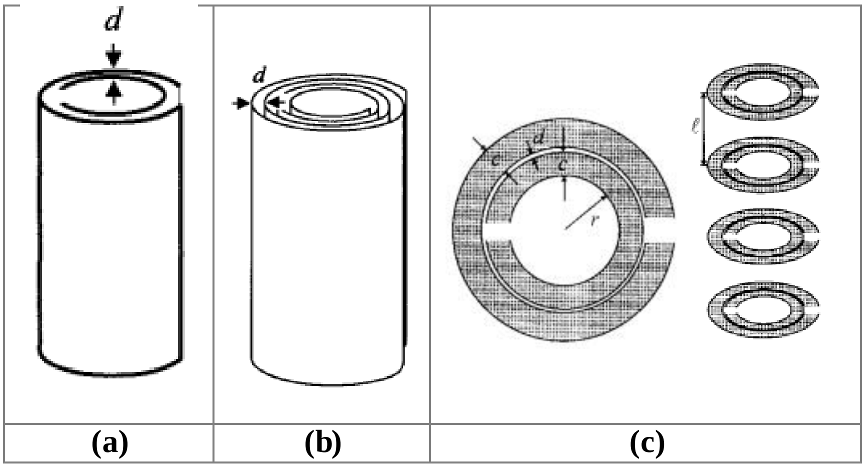

Figure 2.8: Magnetic resonators with negative permeability: **(a)** ‘Split ring’ structure,**(b)** ‘Swiss Roll’ capacitor,**(c)** Planar Split-ring structure with thin sheets of metal and its stacking sequence [7].

Effective permeability function μ_{eff} of the planar split ring structure, shown in Figure 2.8(c), is derived in [7]. Throughout the derivation, the cell dimension is assumed to be much smaller than the wavelength. Assuming r ≫ c, r ≫ d, l < r and $\ln(\frac{c}{d}) \gg \pi$, μ_{eff} is given as follows [7]:

$$\mu_{eff} = 1 - \frac{\frac{\pi r^2}{a^2}}{1+\frac{2l\sigma_1}{\omega r\mu_o}j - \frac{3lc_0{}^2}{\pi\omega^2 \ln\left(\frac{2c}{d}\right)r^3}} = \mu_{eff}{}' + j\,\mu_{eff}{}'' \tag{2.48}$$

The real ($\mu_{eff}{}'$) and imaginary ($\mu_{eff}{}''$) parts of the effective permeability μ_{eff} can be expressed as

$$\mu_{eff}{}' = 1 - \frac{\frac{\pi r^2}{a^2}\left(1 - \frac{3lc_0{}^2}{\pi\omega^2 \ln\left(\frac{2c}{d}\right) r^3}\right)}{\left(1 - \frac{3lc_0{}^2}{\pi\omega^2 \ln(\frac{2c}{d}) r^3}\right)^2 + \left(\frac{2l\sigma_1}{\omega r \mu_o}\right)^2} \tag{2.49}$$

$$\mu_{eff}{}'' = \frac{\frac{\pi r^2}{a^2}\frac{2l\sigma_1}{\omega r \mu_o}}{\left(1 - \frac{3lc_0{}^2}{\pi\omega^2 \ln(\frac{2c}{d}) r^3}\right)^2 + \left(\frac{2l\sigma_1}{\omega r \mu_o}\right)^2} \tag{2.50}$$

In equation 2.48, a and l are the lattice spacing and stacking distance between cells, respectively, in a two-dimensional split ring array. The parameters r, c and d represent inner radius, width of each ring and spacing between the ring sheets, respectively; σ_1 is the resistance of unit length of the sheets measured around the circumference; c_0 and μ_o are universal constants for velocity of the light in free space and permeability of free space in this expression.

The resonance frequency ω_0 at which μ_{eff} diverges (i.e. the real part of the denominator in equation 2.48 becomes zero) can be given as

$$\omega_0{}^2 = \frac{3lc_0{}^2}{\pi \ln(\frac{2c}{d}) r^3} \tag{2.51}$$

The magnetic plasma frequency ω_{mp} being the frequency below which the real part of effective permeability is negative can be expressed as

$$\omega_{mp}{}^2 = \frac{3\, l\, c_0{}^2}{\left(1 - \frac{\pi r^2}{a^2}\right) \pi \ln\left(\frac{2\,c}{d}\right) r^3} \tag{2.52}$$

Using the original dimensions of the planar split ring structure given in [7], real ($\mu_{eff}{}'$) and imaginary ($\mu_{eff}{}''$) parts of the effective permeability are computed and plotted as shown in Figure 2.9.

Permeability function shown in Figure 2.9 displays a typical Lorentzian behavior. It has a negative real part over a very narrow band between the magnetic plasma frequency $f_{mp} = \omega_{mp}/2\pi$= 14.4 GHz and the resonance frequency $f_0 = \omega_0/2\pi$= 13.5 GHz. As the real and imaginary parts of the permeability function vary with frequency, this split ring array is inherently a dispersive medium.

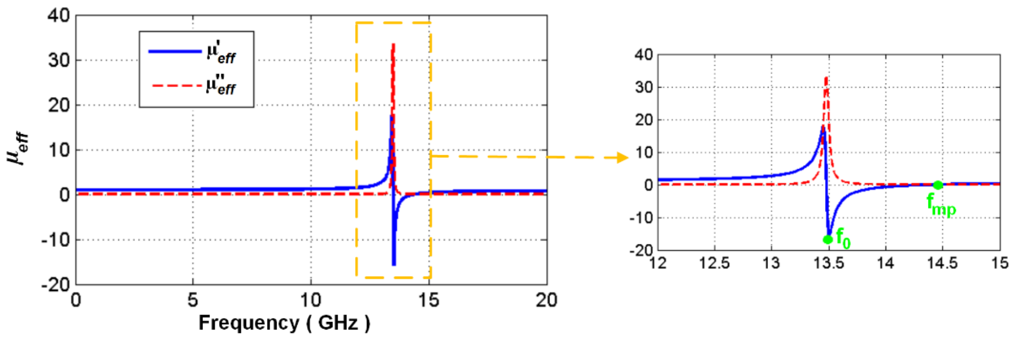

(a) **(b)**

Figure 2.9: (a) Real ($\mu_{eff}{}'$) and imaginary ($\mu_{eff}{}''$) parts of the effective permeability for the planar split ring structure given in [7]. **(b)** Zoomed version of the effective permeability plot.

After the realization of negative permeability using the conductors shaped into split rings, various MNG metamaterials having desirable capabilities such as multi-band operation, broad-band permeability characteristic, and miniaturized geometry at GHz, as well as at THz frequencies have become possible [30-54].

2.6 Design and Realization of DNG Metamaterials

It is known that the wire media which is an ENG metamaterial provides negative ε_{eff} over a wide frequency band, while split ring structures which are MNG metamaterials provide negative μ_{eff} over a narrow frequency band. A DNG metamaterial with negative refractive index can be obtained over a narrow frequency band (which is the cross-section of ENG and MNG bands) when these two types of metamaterial topologies are combined. Using this basic approach, a DNG metamaterial having simultaneous negative effective permittivity and negative effective permeability was designed and experimentally verified for the first time by combining the wire media and planar split ring structure [8]. The unit cell for this combined structure is shown in Figure 2.10(a). An array of unit cells consisting of 17 split rings along the direction of magnetic field H and 8 elements along the direction of propagation vector k is fabricated and measured using a two-dimensional microwave scattering chamber [8]. Negative refractive index is verified for the direction of propagation presented in Figure 2.10(a).

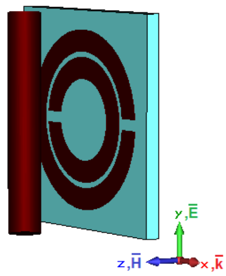

(a)

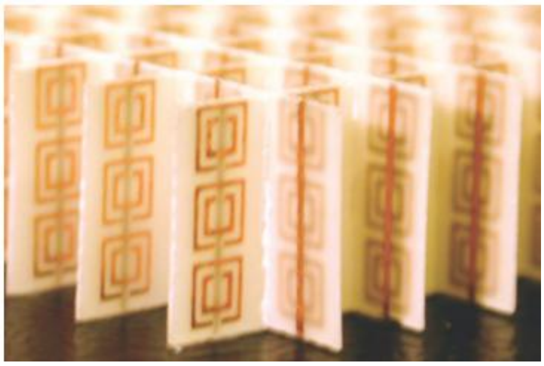

(b)

Figure 2.10: (a) Unit cell of the DNG metamaterial as a combination of the wire media and ‘‘split-ring’’ structure [8]. **(b)** The sample of the DNG metamaterial consisting of square shaped split-ring resonator and wire strips printed on opposite sides of the fiber glass circuit board [10].

After this initial experiment on DNG metamaterials, two further basic experiments given in [9] and [10] are performed using the array of a modified unit cell which consists of a square-shaped split ring resonator and a wire strip printed on the opposite sides of a fiber glass circuit board. The sample used for the experimental study in [10] is presented in Figure 2.10(b). The presence of negative refraction is directly verified by measuring the deflection of a beam of microwave radiation from prism-shaped sample in [10].

After these experimental verifications of negative refractive index, numerous further DNG designs have been demonstrated [55-81].

CHAPTER 3

DESIGN, SIMULATION AND CHARACTERIZATION OF PLANAR METAMATERIAL ARRAYS

In this chapter, important concepts that have to be considered during the design, simulation and characterization of planar metamaterial arrays are investigated. All investigations are performed using the planar dual band nested U-ring resonator (2-NURR) metamaterial array [49] that is a novel exemplar of the planar metamaterial arrays. Firstly, effects of different electromagnetic excitation types on the planar 2-NURR metamaterial array are examined. Then, the effects of using different boundary conditions and different computational volume dimensions in numerical simulations of periodic planar 2-NURR metamaterial arrays are investigated. Next, the commonly used parameter retrieval methods are reviewed with a special focus on the widely used Nicholson-Ross-Weir algorithm. Finally, the effects of having dense metamaterial arrays on the retrieved parameters are presented when these common retrieval algorithms are utilized.

The content of this chapter is mainly composed of three already published papers [178, 189, 191], which are the outcomes of this dissertation.

3.1 Excitation of Planar Metamaterials

Electromagnetic behavior of a metamaterial structure is a strong function of propagation direction and polarization of the electromagnetic excitation. In this subsection, it will be demonstrated that a metamaterial array may be excited electrically and/or magnetically under different types of excitations, or it may not be excited at all under certain excitation conditions. The novel planar dual band nested

U-ring resonator (2-NURR) will be used as the tested metamaterial array in the simulations of this subsection.

Metamaterials are usually designed as periodic arrays of sub-wavelength unit cells. Due to run time and computer memory constrains of the computers, the intended metamaterial may be simulated as an infinitely large array by using proper boundary conditions imposed at the boundaries of a finite computational volume which contains only a single unit cell. As an exemplar of such simulations, the unit cell of the planar 2-NURR metamaterial array is placed within a prism shaped computational volume with side lengths p_x, p_y and p_z as shown in Figure 3.1(a). If this unit cell is excited by a normally incident uniform plane wave, for example, an equivalent two-dimensional (2D) metamaterial array is formed in the plane perpendicular to the incidence direction. Proper boundary conditions must be imposed at the boundaries perpendicular to the directions of the E field and H field of the wave for that purpose. Under a proper excitation, the simulated metamaterial array can result in two LC type resonances, one for each U-ring of the unit cell [49]. Each of these resonances is mainly due to the self inductance (L_{self}) of the associated U-ring and the capacitance (C) between the arms of this ring. Electromagnetic coupling has secondary effects on the values of developed resonance frequencies as to be discussed in Chapter 4. Unusual electromagnetic properties such as having negative values for permittivity and/or permeability can be realized over certain frequency bands at the proximity of these two resonance frequencies of the metamaterial array.

As shown in Figure 3.1 (b), there exist six possible excitation types for this 2-NURR structure where the excitation signal is assumed to be a uniform plane wave. The presence and nature of the resulting resonances are determined by the directions of the E and H fields relative to the orientation of the U-rings. Electric LC resonances of the equivalent array are created by the current activities in the rings when the E field is perpendicular to the arms of the rings. On the other hand, magnetic LC resonances of the equivalent array are created by the induced currents flowing in the rings when the H field is perpendicular to the plane of the unit cell. The latter case is obviously explained by the Faraday's Law. While the electric LC resonances lead to negative values of permittivity within a narrow frequency band around the resonances, the magnetic LC resonances lead to negative values of permeability over such limited bandwidths.

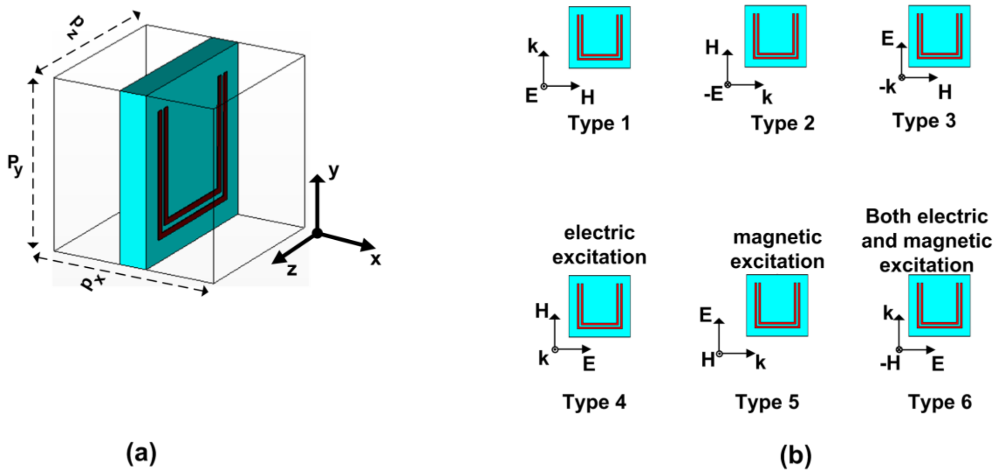

Figure 3.1: (a) Schematic view of the 2-NURR unit cell placed within a computational volume of side lengths p_x, p_y and p_z in the x, y and z directions, respectively. **(b)** Six different cases of excitation for the 2-NURR unit cell.

For the excitation types 1, 2 and 3, H is in the direction parallel to the plane of the U-rings and E field is either parallel to the arm of the U-rings or perpendicular to the ring plane. Therefore, excitation of any electric or magnetic LC resonances is not possible under these excitations. For the excitation type 4, known as the electric excitation, only E field contributes to the resonating response of the metamaterial. The electrically induced LC resonances occur due to the currents flowing through the rings as the E field is perpendicular to the arm of the rings. Thus, the equivalent array is considered as a planar ENG metamaterial having negative permittivity around its LC resonances. On the other hand, only H field contributes to the resonating response of the metamaterial array for the excitation type 5, known as the magnetic excitation. The magnetically induced LC resonances occur due to the circulating induced currents on the rings resulting from the time varying magnetic flux due to H field, which is perpendicular to the plane of the rings. Thus, the equivalent array is considered as a planar MNG metamaterial having negative permeability around its LC resonances. As for the excitation type 6, both electric and magnetic fields contribute to the excitation mechanism of the metamaterial creating LC type resonances due to circulating ring currents.

When the E field direction is parallel to the arms of the rings, circulating currents cannot be developed due to the symmetry of the U-ring topology, but only dipole-type resonances are developed usually at higher frequencies. Values of such dipole-type resonance frequencies depend on the separation between the arms of an individual U-ring and on the periodicity of the U-ring array.

The MNG and ENG regions which can be created in the case of Type-6 excitation are both narrow-band regions. Besides, modeling and characterization of this metamaterial structure under Type-6 excitation in much more complicated (as compared to the case for Type-4 and Type 5 excitations) due to electromagnetic coupling effects. If a DNG metamaterial is going to be designed, the method of placing a metallic strip at the back side of the substrate is much more reasonable. In that case, an array of metallic strips is simulated to provide an ENG region with a very wide bandwidth. Type-5 excitation is suitable for this purpose.

Results of metamaterial array simulations are also strongly affected by the applied boundary conditions and chosen computational domain dimensions especially in the case of unit cells having structural asymmetry with respect to the boundaries. These effects will be investigated in detail in the next subsection using the 2-NURR unit cell under the magnetic excitation.

3.2 Effects of Boundary Conditions and Computational Domain Dimensions in Metamaterial Simulations

This subsection aims to demonstrate the effects of using different boundary conditions and different computational volume dimensions in numerical simulations of periodic metamaterial arrays. The double band metamaterial unit cell (2-NURR) design will be utilized to show that use of different boundary conditions may result in the simulation of dissimilar periodic array topologies with completely different electromagnetic responses. It will also be shown that dimensions of the computational volume may strongly affect the overall response of the metamaterial structure due to varying electromagnetic coupling between the array elements.

In general, metamaterials are designed as periodic arrays of sub-wavelength unit cells to realize unusual electromagnetic properties such as negative values for permittivity and/or permeability over certain frequency bands [1, 8, 10]. Such properties are determined not only by a specific metamaterial unit cell design but also by electromagnetic coupling effects between array elements [35, 153-156]. It is a common practice to analyze metamaterial arrays using numerical techniques prior to fabrication and experimental characterization. Use of commercial electromagnetic full-wave solvers such as CST Microwave Studio (MWS) [157] is found practical especially when a large periodic metamaterial array is to be simulated. During this computational procedure, an infinitely large metamaterial array can be simulated by using proper boundary conditions imposed at the boundaries of a finite sized computational volume that contains a representative metamaterial unit cell.

Periodic boundary conditions as well as perfect electric conductor (PEC) type and perfect magnetic conductor (PMC) type boundary conditions can be frequently implemented in the simulations of periodic metamaterial arrays. Type of the boundary conditions should be selected carefully to simulate the intended metamaterial array topology that is compatible with real-life scenarios of applications and/or measurements in mind. This issue is important particularly when the metamaterial unit cell has a structural asymmetry with respect to the boundaries.

Furthermore, dimensions of the computational volume determine the spatial periods for the simulated metamaterial array, which affect the level of electromagnetic coupling between array elements. Importance of these issues will be demonstrated in detail in the rest of the section by carefully designed numerical simulations.

3.2.1 Unit Cell Design and Simulation Setup for a Double Band Metamaterial

In this section, we use a recently suggested novel double band magnetic metamaterial topology called nested U-ring resonator (2-NURR) which has the basic unit cell geometry composed of two nested U-shaped metallic rings [49] as described in Figure 3.2. Design parameters for this unit cell are defined as the side length of the substrate along z direction (L_{sz} = 6.2 mm), side length of the substrate along y direction (L_{sy}), base length of the outer U-ring (l = 4.6 mm), arm lengths of the U-rings (h_1 = 4.6 mm and h_2 = 4.2 mm), width of the metal strips (w = 0.2 mm) and separation distance between the rings (s = 0.2 mm). Additional design parameters are conductivity (σ = 5.8×10^7 S/m) and thickness (t = 0.035 mm) of the copper strips as well as relative permittivity (ε_r = 3), thickness (d = 1.016 mm) and loss tangent ($\tan\delta$ = 0.002) of the Arlon AD-300A type dielectric substrate.

Simulation results to be presented for this structure are obtained by CST Microwave Studio (MWS). The CST MWS setup described in Figure 3.3 is used to simulate a two dimensional infinitely large metamaterial array that is periodic along the x- and y-axes. This array is excited by a linearly polarized incident electromagnetic uniform plane wave such that its E field is directed along the y-axis (i.e. parallel to the arms of the U-rings) and its H field is directed along the x-axis. As the incident H field is perpendicular to the unit cell plane, surface currents are induced along the U-rings as anticipated by Faraday’s law. Input and output ports of the simulation setup are located to be perpendicular to the direction of incident propagation vector k. Complex S-parameters of the metamaterial array are simulated under this magnetic excitation scenario using a computational prism with dimensions (p_H, p_E, p_k) along the (x, y, z) axes as described in Figure 3.3. Herein, p_H and p_E parameters determine the spatial periods of the simulated metamaterial array along the x-axis (parallel to the incident H vector) and y-axis (parallel to the incident E vector), respectively. To provide a continuous substrate along the y- axis, $L_{sy} = p_E$ is used in the design.

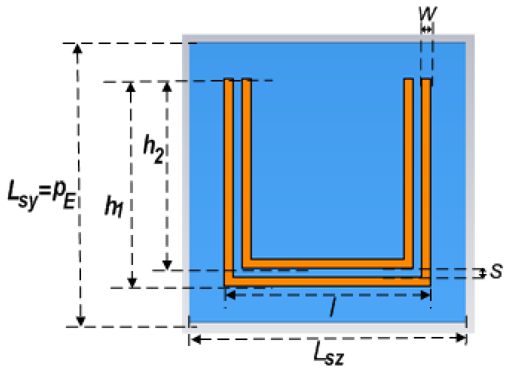

Figure 3.2: Schematic view for the 2-NURR type unit cell.

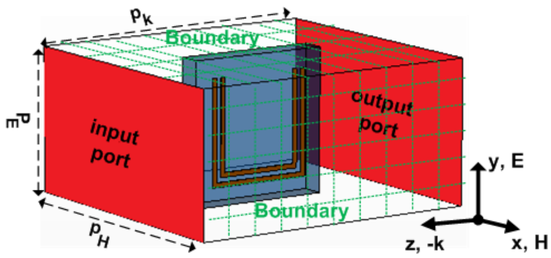

Figure 3.3: Simulation setup and excitation field.

In the next section, results of the metamaterial array simulations for this unit cell structure will be reported for different types of boundary conditions: First, the combination of perfect electric conductor and perfect magnetic conductor (PEC/PMC) type boundary conditions will be imposed at the boundaries of the computational prism. Magnitude and phase spectra of the complex scattering parameters S_{11} and S_{21} (i.e. complex reflection and complex transmission parameters defined at the input port), surface current distributions and normal component of the total E field will be plotted at both resonance frequencies of the resulting double band metamaterial array. Next, similar results will be obtained when the unit cell (UC) boundary condition (a periodic boundary condition provided by the CST MWS) is imposed at the boundaries of the computational prism. Effects of changing computational prism dimensions (i.e. changing the spatial periods of metamaterial array) will also be investigated in both cases. Finally, use of the PEC boundary condition at all four boundaries will be compared to the use of UC and PEC/PMC boundary conditions as the last simulation example.

3.2.2 Simulations of the Double Band Metamaterial Array with PEC/PMC Boundary Conditions

In this section, perfect electric conductor (PEC) boundary condition is imposed at the upper and lower walls of the computational prism (i.e. at the planar boundaries which are perpendicular to the incident E vector) while the perfect magnetic conductor (PMC) boundary condition is imposed at the back and front walls which are perpendicular to the incident H field in the simulation setup seen in Figure 3.3. In CST MWS, “Electric (E_t=0)” and “Magnetic (H_t=0)” terms are used to refer to PEC and PMC, respectively. An infinitely large two-dimensional periodic array, schematically described in Figure 3.4, is effectively simulated by this setup based on the imaging effects of the PEC and PMC type planar boundaries. It is well known that the image of a current element flowing parallel (perpendicular) to the PEC boundary should be formed in the opposite (same) direction.

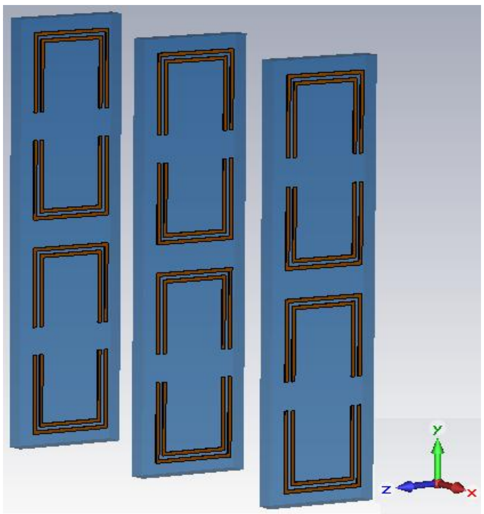

Figure 3.4: Effective metamaterial array simulated by using PEC/PMC boundary conditions in the setup of Figure 3.3.

Due to this effect, the simulated effective unit cell is not the same as the basic nested U-ring type unit cell anymore but it is in the shape of nested rectangular rings each having two aligned cuts on the sides parallel to y-axis as shown in Figure 3.4. Now, the effective periods for this nested rectangular ring type array become ($2p_E$) and (p_H) along the y- and x-axes, respectively. Also, circulating currents should be expected in rectangular rings of this effective unit cell at resonance frequencies. Furthermore, this rectangular unit cell structure is repeated along the x-axis preserving the same current directions due to the fact that mirror image of a current element flowing parallel to a PMC boundary is formed in the same direction. Simulation results obtained for the metamaterial array (seen in Figure 3.4) are presented in Figure 3.5 for the parameters $p_E = 6.2$ mm and $p_H = 12$ mm.

Magnitude and phase plots of the complex scattering parameters S_{11} and S_{21} are shown in Figures 3.5(a) and 3.5(b), respectively, revealing two distinct resonance frequencies at 8.358 GHz and 9.462 GHz, which are consistent with the presence of two nested rings [49]. Figure 3.5(c) presents the surface current density plots at each resonance frequency confirming the presence of circulating currents (i.e. induced magnetic dipoles) along the rectangular rings. Finally, Figure 3.5(d) plots the amplitude of E_{normal} that is the measure of surface charge density on the metal traces. Induced current directions in figure 3.5(c) and induced charge polarities in Figure 3.5(d) clearly reveal the mirror imaging effects due to the use of PEC boundary conditions.

As shortly mentioned before, dimensions of the computational prism should be selected carefully in numerical simulations as these dimensions determine the simulated array periods and hence the level of electromagnetic coupling between neighboring elements of the metamaterial array. To demonstrate this point, transmission curve of the metamaterial array (seen in Figure 3.4) is computed for different values of computational prism dimensions p_E and p_H to simulate different array periods. First, p_E is kept at 6.2 mm while reducing p_H from 12 mm to 6 mm and to 2 mm. The resulting transmission curves are plotted in Figure 3.6.

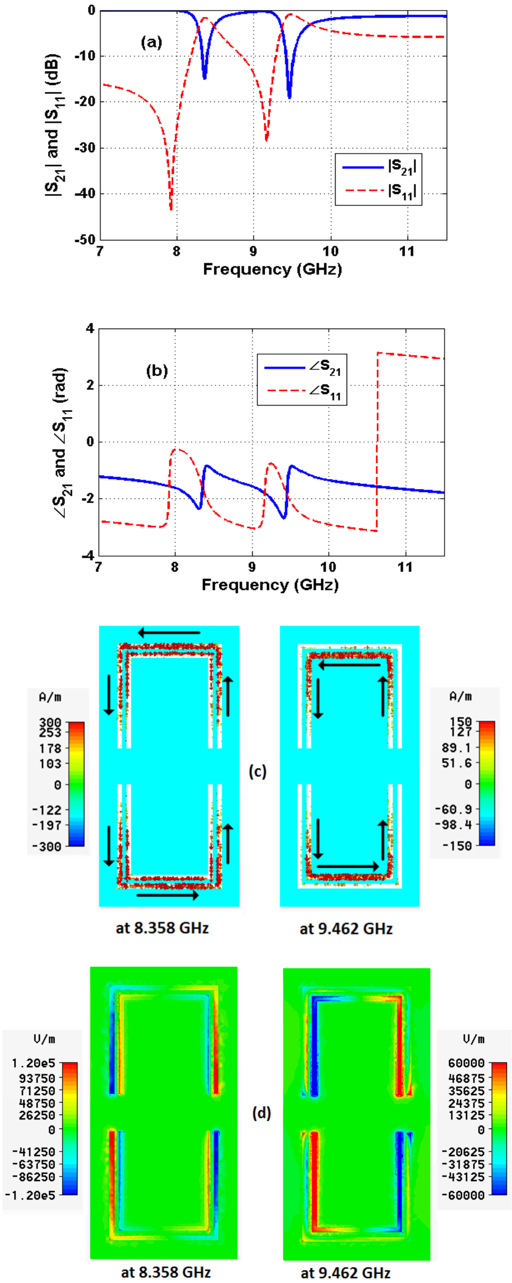

Figure 3.5: Simulation results for the metamaterial array seen in Figure 3.4 (using PEC/PMC boundary conditions) with parameters p_E = 6.2 mm and p_H = 12 mm. **(a)** Transmission and reflection curves (magnitudes of S_{11} and S_{21}). **(b)** Phase curves of of S_{11} and S_{21}. **(c)** Surface current densities at resonance frequencies. **(d)** Amplitudes of E_{normal} at the cell surface (proportional to surface charge density) at resonance frequencies.

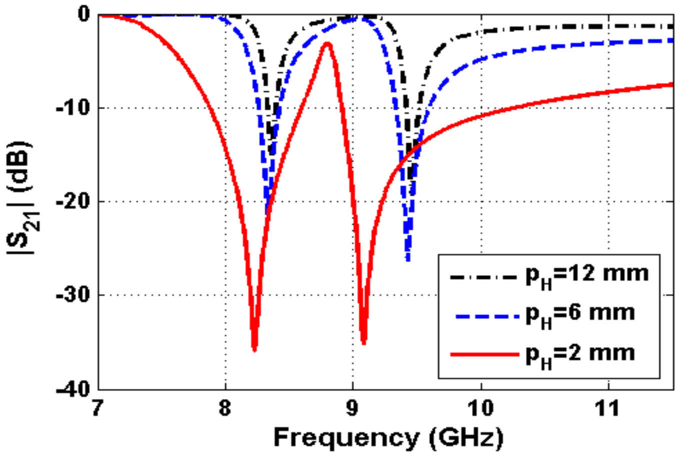

Figure 3.6: Transmission spectra of the effective array (seen in Figure 3.4) that is simulated by using PEC/PMC boundary conditions for p_E = 6.2 mm along the *y*-axis and varying periods p_H along the *x*-axis.

It is seen that frequency and bandwidth of individual resonance curves are strongly affected as the metamaterial array becomes denser along the *x*-axis due to increased coupling of magnetic flux.

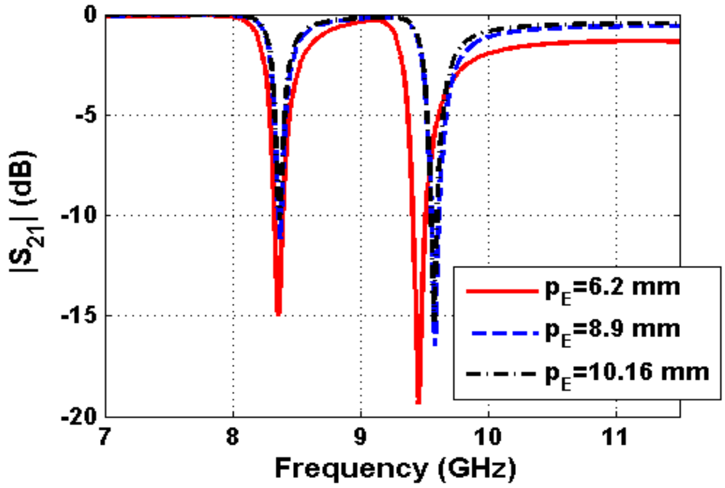

Figure 3.7: Transmission spectra of the effective array (seen in Figure 3.4) that is simulated by using PEC/PMC boundary conditions for p_H = 12 mm along the *x*-axis and varying periods p_E along the *y*-axis.

Next, the transmission curves are computed when p_H is kept at 12 mm while increasing p_E from 6.2 mm to 8.9 mm and to 10.16 mm as presented in Figure 3.7. *S*-parameter changes observed in Figure 3.7 are not as remarkable as the changes observed in Figure 3.6. Increasing the period p_E beyond 8.9 mm does not make additional changes in the resonance curves as the electric coupling through the gap capacitances becomes too weak when the effective gap width (or slit width as also called) is increased.

3.2.3 Simulations of the Double Band Metamaterial Array with Unit Cell (UC) Boundary Conditions

In this section, metamaterial array simulations of the previous section are repeated by using the unit cell (UC) boundary condition instead of the PEC/PMC boundary conditions at all four boundaries of the computational prism. In this case, the basic nested U-ring resonator (2-NURR) structure is periodically repeated along the *x*-axis and *y*- axis with identical current distributions. The resulting effective metamaterial array is seen in Figure 3.8.

Simulation results obtained for this array topology are presented in Figure 3.9 for the parameters p_E = 6.2 mm and p_H = 12 mm. In more detail, Figure 3.9(a) and 3.9(b) show the magnitude and phase of the complex *S*-parameters S_{11} and S_{21} computed under UC boundary conditions. Two distinct magnetic resonances are displayed in Figure 3.9(a), at 8.574 GHz and 10.374 GHz, which are shifted upwards as compared to the resonance frequencies observed in Figure 3.5(a). Also observed, in Figure 3.9(a), that the second resonance is much stronger as compared to the first resonance. As seen in Figure 3.9(c) and 3.9(d), magnetic dipoles are induced along the U-rings with associated induced surface charge densities on the metal strips. Finally in Figures 3.10 and 3.11, effects of changing computational prism dimensions p_H and p_E (to simulate different array periods) on the transmission spectra are presented.

When these two figures are compared to Figures 3.6 and 3.7, it is concluded that electromagnetic coupling between neighboring cells turns out to be much more dominant in the nested U-ring based periodic array (simulated by UC boundary condition). When this array gets denser, especially along the x-axis direction, its resonance frequencies shift to higher frequencies by quite large amounts with a significantly larger separation. This behavior is just the opposite of what we have observed in Figure 3.6 for the nested rectangular ring array (simulated by PEC/PMC boundary conditions). It is seen in Figure 3.6 that resonance frequencies of the array shift to lower frequencies while getting closer to each other as p_H becomes smaller. Similarly, as these two different arrays become denser with smaller p_E values, directions of shifts in their resonance frequencies turn out to be opposite to each other as observed in Figures 3.7 and 3.11.

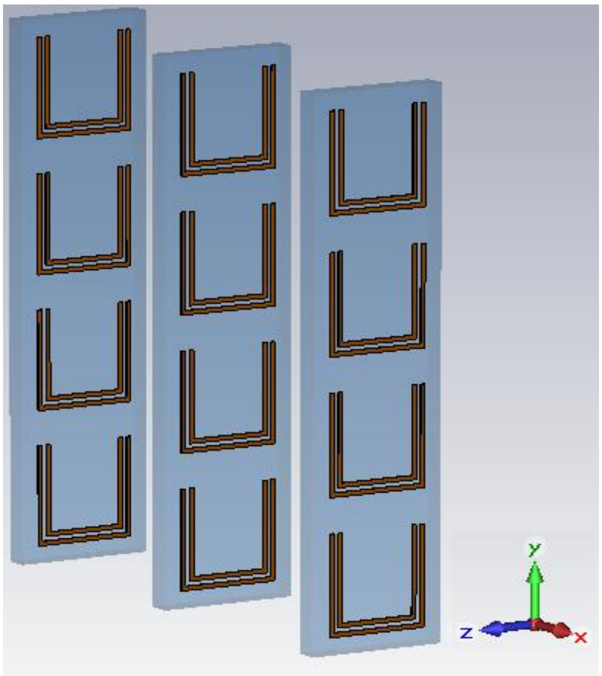

Figure 3.8: Effective metamaterial array simulated by using UC boundary conditions in the setup of Figure 3.3.

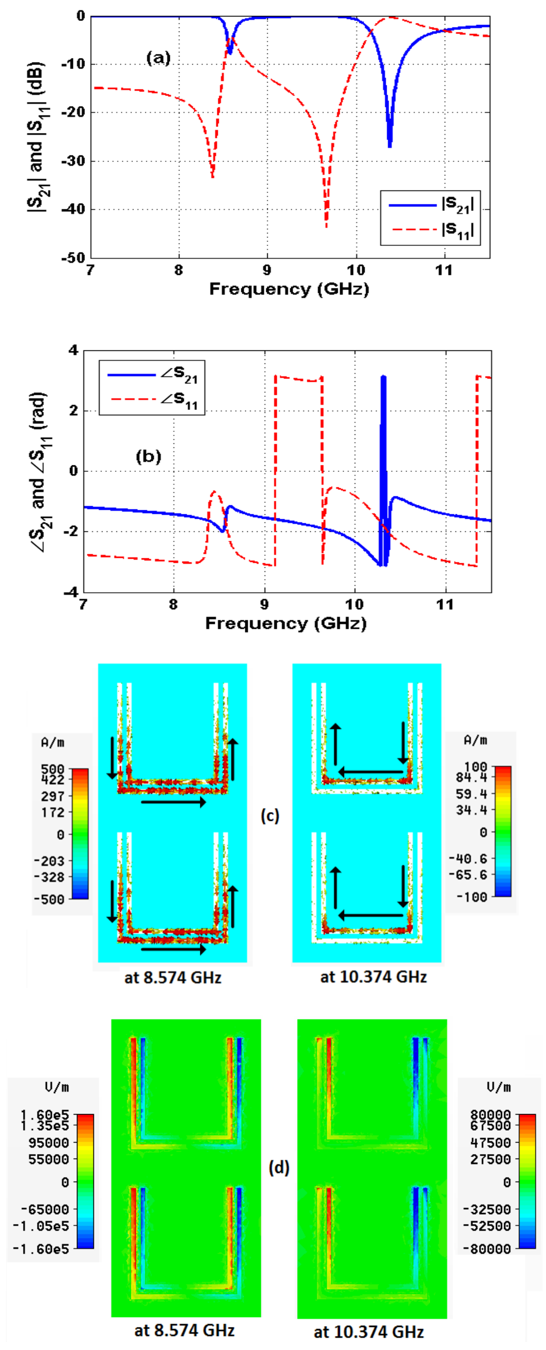

Figure 3.9: Simulation results for the metamaterial array seen in Figure 3.8 (using UC boundary condition) with parameters p_E = 6.2 mm and p_H = 12 mm. **(a)** Transmission and reflection curves (magnitudes of S_{11} and S_{21}). **(b)** Phase curves of S_{11} and S_{21}. **(c)** Surface current densities at resonance frequencies. **(d)** Amplitudes of E_{normal} at the cell surface (proportional to surface charge density) at resonance frequencies.

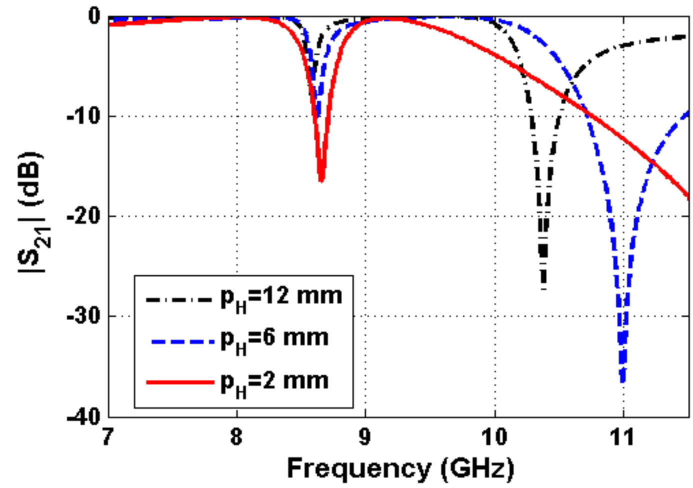

Figure 3.10: Transmission spectra of the effective array simulated by using the UC boundary condition for p_E = 6.2 mm along the *y*-axis and varying periods p_H along the *x*-axis.

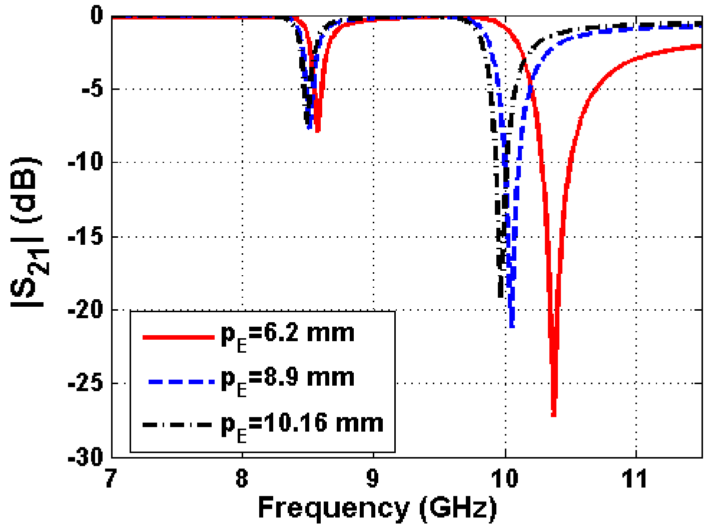

Figure 3.11: Transmission spectra of the effective array simulated by using UC boundary condition for p_H =12 mm and for varying periods p_E.

3.2.4 Use of PEC/PEC, PEC/PMC and UC Boundary Conditions for the Simulation of a Sparse Periodic Array

In this section, sparse periodic arrays will be simulated for the basic nested U-ring type metamaterial unit cell (shown in Figure 3.2) using PEC/PEC, PEC/PMC and UC boundary conditions. Implementation of the PEC/PEC boundary condition would be meaningful when the metamaterial unit cell is placed within a metallic waveguide either for the purpose of experimental characterization [35] or for specific applications involving metamaterial loaded waveguides [196-197]. In such cases, all four metallic walls of the waveguide can be modeled as perfect electric conductor (PEC) surfaces. Clearly, the mirror imaging effect of PEC boundaries are effective in both directions of periodicity when PEC/PEC boundary conditions are implemented. The 2-NURR structure shown in Figure 3.2 resonates in the X-band region. So, it can be conveniently placed within an X-band rectangular waveguide for experimental characterization, for example, if its resonances fall in the single-mode operation range of the waveguide. This condition is satisfied for the cross-sectional waveguide dimensions of 22.86 mm × 10.16 mm along the x and y axes, respectively, providing only the fundamental TE_{10} mode excitation over the frequency band from 6.56 GHZ to 13.73 GHz. When the computational domain in CST MWS setup is defined to be the waveguide volume with PEC walls, a sparse metamaterial array is simulated with large spatial periods p_H = 22.86 mm and p_E = 10.16 mm. Here, especially p_H is large enough to safely neglect electromagnetic coupling between neighboring unit cells along the x-axis direction. Simulation of a sufficiently sparse array is useful to approximate the response of a single isolated metamaterial unit cell or a small size array. This approach is efficiently used in a recent work to characterize electromagnetic behavior of a miniaturized metamaterial sensor that typically composed of a single cell of double sided SRR with a multi-layer substrate [198].

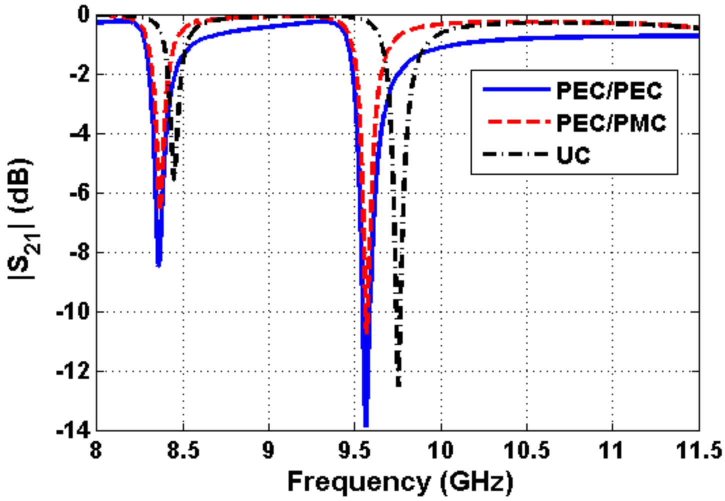

Figure 3.12: Transmission spectra of sparse effective arrays simulated by PEC/PEC, PEC/PMC and UC boundary conditions for p_H = 22.86 mm and p_E = 10.16 mm.

Figure 3.12 shows the transmission spectra belonging to three different sparse metamaterial arrays obtained by using PEC/PEC, PEC/PMC and UC boundary conditions. The same computational domain with periods p_{H} = 22.86 mm and p_{E} = 10.16 mm is used in all three simulations for the sake of fair comparisons. Application of PEC/PEC and PEC/PMC boundary conditions makes a difference only along the *x*-axis direction where the period p_{H} = 22.86 mm is effective. As negligible coupling is expected due to this large period p_{H}, imposing PEC or PMC boundary condition at the boundaries perpendicular to the *x*-axis is not important anymore. Therefore, the transmission spectra simulated for the PEC/PEC and PEC/PMC boundary conditions turn out to be almost the same in Figure 3.12, as expected. Transmission spectra obtained for the UC boundary condition, on the other hand, is found slightly different than the other two transmission curves with upward shifted resonance frequencies. This small shift may be explained by the fact that the period p_{E} = 10.16 mm is not large enough to simulate a sufficiently sparse array along the *y*-direction.

Till this point, effects of excitation types, boundary conditions and computational domain dimensions in metamaterial simulations are explained in detail in sections 3.1 and 3.2. Now, one can design and simulate an intended metamaterial array using a full wave electromagnetic solver at the light of these explanations. After designing and simulating the intended metamaterial array, determination of the effective medium parameters, which are the dielectric permittivity (ε) and magnetic permeability (μ), is the next step to reveal the electromagnetic behavior of the metamaterial array. Medium parameters of the metamaterial arrays are extracted using a retrieval algorithm, which commonly makes use of S-parameters (i.e. the complex-valued transmission and reflection spectra) which are obtained either from simulations or from measurements. In the next section, a commonly used retrieval algorithm and its improved versions will be reviewed and the questionable issues about these algorithms will be discussed.

3.3 Parameter Retrieval Based on the Nicolson-Ross-Weir (NRW) Algorithm

Aim of this section is to review the parameter retrieval (which is also called as parameter extraction) procedures in literature with a special focus on the widely used NRW retrieval method which is based on the "homogeneous slab" model. Highly debated issues on this method such as non-uniqueness of the solutions and the "anti-resonant effects" are emphasized. To demonstrate the presence of unphysical results produced by this retrieval method, we investigate the effects of metamaterial array periodicity on the retrieved parameters. In simulations, a nested U-ring type double-band metamaterial array (2-NURR) will be magnetically excited to obtain negative permeability bands. Then, the commonly used NRW retrieval method (that treats the metamaterial array approximately as a homogeneous slab) [15] will be used to obtain the complex effective permittivity and permeability curves for this metamaterial topology. It will be shown that when the periodicity along the incident H-field direction is decreased (i.e. when the array gets denser), S-parameter curves are considerably affected due to increased magnetic coupling. Furthermore, the "anti-resonance effect" (i.e. the presence of negative imaginary part for permittivity which contradicts with the "passivity" requirement under the $e^{-i\omega t}$ convention) will be demonstrated to become worse as the array gets denser although the physical dimensions of the metamaterial unit cell remains the same. Also, to check for the condition of "causality", real parts of retrieved permittivity and permeability curves will be calculated from the retrieved imaginary parts of these parameters using the Kramers-Kronig (K-K) relations. The results will show that as the metamaterial array becomes denser, the discrepancy between the retrieved and calculated real parts of parameters will be increasing [178]. This is obviously an indication for the violation of causality.

3.3.1 Overview of the Retrieval Methods

As opposed to natural materials, metamaterials can have negative (or near-zero) values of permeability and/or permittivity over certain bands around their resonance frequencies. These electromagnetic constitutive parameters cannot be measured directly but retrieved using several different methods such as those based on the average fields inside the metamaterial [158-160], parameter fitting of dispersive models [161], use of simulated or measured complex scattering parameters, S_{11} and S_{21} [162-174, 15].

It is very common in metamaterial literature to use the simple homogenization procedure based on the so called Nicholson-Ross-Weir (NRW) algorithm for parameter retrieval using simulated or measured complex scattering parameters. In this method, an array of resonant unit cells (i.e. a slab of metamaterial) is treated as a slab of a homogeneous material. Then, the refractive index, impedance, effective permeability and effective permittivity parameters of this homogeneous metamaterial slab are retrieved using the complex valued transmission and reflection spectra (i.e. S_{11} and S_{21}) [162-167] under the assumption of a normally incident uniform plane wave excitation.

In order to run this algorithm, scattering parameters are needed, which can be computed easily by using electromagnetic full wave solvers such as ANSOFT HFSS or CST MWS. Although implementation of this algorithm is relatively easy and straightforward, unphysical results such as the “anti-resonant effects” have been observed in the retrieved parameters.

Improved and advanced versions of the NRW retrieval algorithm have been generated to pay special attention to bianisotropy [168, 173], causality and use of Kramers-Kronig relations [170, 15], inhomogeneity and asymmetry along propagation direction [199], differences between the edge and inner cells [171] and the excitation under oblique incidence [169, 172].

In spite of all these advanced efforts, the so called "anti-resonant effects" have not been eliminated properly. It has been argued instead that this effect is an intrinsic property of the retrieved medium parameters of the metamaterial and it cannot be removed by decreasing the unit cell size [200]. It is explained in some papers as a result of "finiteness" of the metamaterial composite [200-201]. Woodley et al. is even argued that the anti-resonant effect (i.e. negative imaginary parts of the effective medium parameters) is due to numerical error in the simulations [202].

Additionally, the problem of "non-uniqueness" has also been addressed in some publications [15, 164, 167, 170, 203]. It is known that the imaginary part of refractive index can be determined uniquely, but the real part of refractive index is not unique due to the branch problem. Ghodgaonkar et al. proposed that correct values of permittivity and permeability can be obtained by using the sample thickness to be less than the wavelength [164]. As discussed in [164], to determine the real part of the refractive index uniquely, more than one measurement can be taken using the sample with different thicknesses. An iterative method was proposed to find the correct value of the real part of the refractive index by Chen et al. [167]. Recently, Kramers-Kronig approach [15, 170] and phase unwrapping method [204] were proposed to solve effectively this branch problem.

Validity of all these explanations has been questioned in some recent publications based on the observations that the results of NRW parameter retrieval algorithm violate the basic physical requirements of passivity and causality to some extent [175-179]. Spatial dispersion effects were also discussed in this context [175-177, 180].

Alu stated that spatial dispersion and magnetoelectric coupling have to be taken into account for a trustable metamaterial homogenization especially for densely packed arrays [180]. He proposed a new homogenization procedure which includes spatial dispersion and magnetoelectric coupling effects into modeling. Although his modeling approach is reasonably accurate, its implementation to complicated metamaterial topologies does not look straightforward.

In the next section, the parameter retrieval algorithm based on the use of NRW method and Kramers Kronig (K-K) relation [15] will be outlined as this approach is used for permeability and permittivity calculations throughout this chapter.

3.3.2 Outline of the Parameter Retrieval Algorithm Based on NRW Method and Kramers Kronig (K-K) relation

A given metamaterial sample of thickness d_k (along the propagation direction) can be approximately treated as a homogeneous slab, due to the sub-wavelength size of metamaterial unit cells, as shown in Figure 3.13. Then, under the assumption of a normally incident uniform plane wave (upw) excitation, the effective permeability (ε) and effective permittivity (μ) of a given metamaterial will be retrieved from either simulated or measured *S*-parameters (S_{11} and S_{21}) by using the following procedure.

For the equivalent "homogeneous dielectric slab" problem, the complex S parameters S_{11} and S_{21} can be expressed as [15, 167]

$$S_{11} = \frac{R_{01}(1 - e^{j2nk_0 d_k})}{1 - R_{01}^2 e^{j2nk_0 d_k}} \tag{3.1}$$

$$S_{21} = \frac{(1 - R_{01}^2)e^{jnk_0 d_k}}{1 - R_{01}^2 e^{j2nk_0 d_k}} \tag{3.2}$$

where R_{01}= (z-1)/(z+1), d_k is thickness of metamaterial sample along the propagation direction, k_0 is the free space wave number and $n = n' + j\, n''$ is the complex valued effective refractive index of the metamaterial medium. The complex normalized wave impedance $z = z' + j\, z''$ and the complex exponential $exp(jnk_0d_k)$ can be computed from the S-parameters, S_{11} and S_{21} as [167]

$$z = \pm\sqrt{\frac{(1+S_{11})^2 - S_{21}^2}{(1-S_{11})^2 - S_{21}^2}} \tag{3.3}$$

$$e^{jnk_0d_k} = X \pm j\sqrt{1-X^2} \tag{3.4}$$

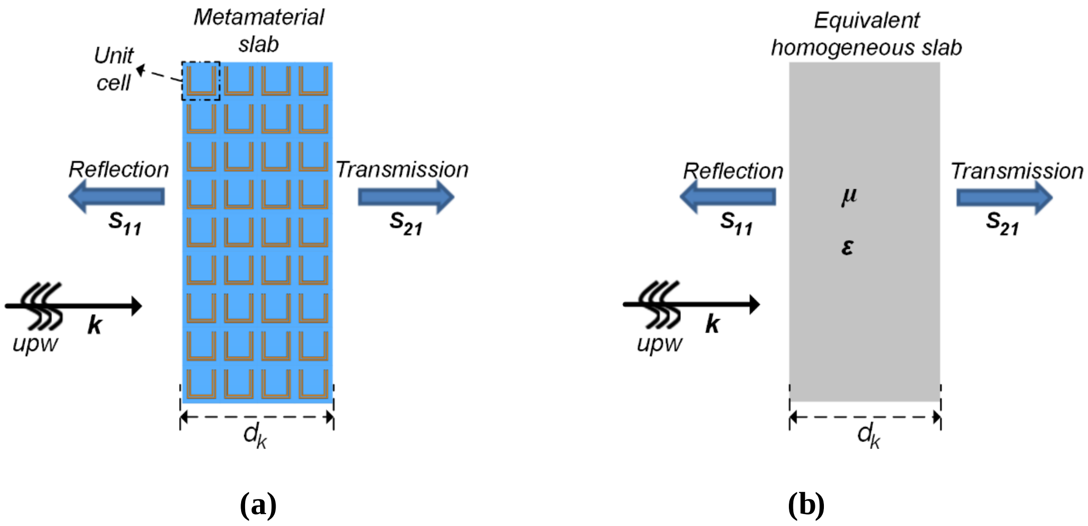

Figure 3.13: Illustration of Nicholson-Ross-Weir (NRW) Method : **(a)** A slab of metamaterial excited by a uniform plane wave (upw) having the propagation vector k, **(b)** The equivalent homogeneous slab having effective medium parameters ε and μ.

where X= 1 / [$2S_{21}(1\text{-}S_{11}^2+S_{21}^2)$] . The ± sign ambiguity occurring in equations 3.3 and 3.4 can be resolved by imposing the conditions $z' \geq 0$ and $n'' \geq 0$ (for $exp(-j\omega t)$ time harmonic convention) as the metamaterial sample is a passive medium [167]. It should be reminded that while the engineering notation (i.e. $exp(j\omega t)$ dependence for time harmonics with $\mu/\mu_0 = \mu_r = \mu' - j\mu''$ and $\varepsilon/\varepsilon_0 = \varepsilon_r = \varepsilon' - j\varepsilon''$ for medium parameters) is used in chapter 2, the physicians notation (i.e. $exp(-j\omega t)$ dependence for time harmonics with $\mu/\mu_0 = \mu_r = \mu' + j\mu''$ and $\varepsilon/\varepsilon_0 = \varepsilon_r = \varepsilon' + j\varepsilon''$ for medium parameters), which is the original notation used in the retrieval algorithm [15], is preferred in this section. Using equation 3.4, the refractive index n can be obtained by computing the natural logarithm of $exp(jnk_0d_k)$ as

$$n = \frac{1}{k_0 d_k}\left[Im\left[ln(e^{jnk_0d_k})\right] + 2m\pi\right] - j\frac{1}{k_0 d_k} Re\left[ln(e^{jnk_0d_k})\right] \qquad (3.5)$$

$$= n' + j\, n''$$

where

$$n' = \frac{Im\left[ln(e^{jnk_0d_k})\right]}{k_0 d_k} + \frac{2m\pi}{k_0 d_k} = n'_0 + \frac{2m\pi}{k_0 d_k} \qquad (3.6)$$

$$n'' = -\frac{Re\left[ln(e^{jnk_0d_k})\right]}{k_0 d_k} \qquad (3.7)$$

and m is an integer. As seen in equation 3.6 and 3.7, although the imaginary part n'' can be uniquely determined, the solution for the real part n' is not unique due to the branching problem that is inherent to the logarithmic function as discussed in [167] and [15]. This problem is essentially caused by the ambiguity in the determination of phase of the transmitted field (S_{21}) due to phase wrapping as discussed in [170].

As suggested for the first time in [170], the causality condition can be enforced to obtain a unique solution to this inverse problem. It is well known that the Kramers-Kronig (K-K) relations relate the real and imaginary parts of the medium parameters such as permittivity and permeability. The K-K relations are conditions for causality to be satisfied in any physical medium. If we know the real part of any medium parameter we can calculate the imaginary part of this parameter using the K-K relation, and vice versa. Therefore, the real part n' can be calculated from the uniquely determined imaginary part n'' as

$$(n')^{KK}(\omega') = 1 + \frac{2}{\pi} P \int_0^{\infty} \frac{\omega\, n''(\omega)}{\omega^2 - \omega'^2} d\omega \tag{3.8}$$

where P denotes the principal value of the improper integral. The integration of (3.8) can be calculated numerically as [15]

$$(n')^{KK}(\omega_i) = 1 + \frac{\Delta\omega}{\pi} \left(\sum_{j=1}^{i-2} \Psi_{i,j} + \sum_{j=i+1}^{N-1} \Psi_{i,j} \right) \tag{3.9}$$

$$\Psi_{i,j} = \frac{\omega_j n''(\omega_j)}{\omega_j^2 - \omega_i^2} + \frac{\omega_{j+1} n''(\omega_{j+1})}{\omega_{j+1}^2 - \omega_i^2} \tag{3.10}$$

Substituting the real part of the refractive index predicted by the Kramers–Kronig relation, $(n')^{KK}$, in equation 3.6, the branch number m can be calculated as

$$m^* = Round\left[((n')^{KK} - n'_0) \frac{k_0 d_k}{2\pi} \right] \tag{3.11}$$

where the function *Round()* means that m^* is an integer nearest to the value of $((n')^{KK} - n'_0) \frac{k_0 d_k}{2\pi}$.

Then, the actual value of the real part of the refractive index is found by substituting the branch number m^* in equation 3.6.

Finally, retrieved relative permeability $\mu/\mu_0 = \mu_r = \mu' + j\mu''$ and relative permittivity $\varepsilon/\varepsilon_0 = \varepsilon_r = \varepsilon' + j\varepsilon''$ parameters can be solved from the computed values of $z = \sqrt{\frac{\mu_r}{\varepsilon_r}}$ and $n = \sqrt{\mu_r \varepsilon_r}$ using the expressions as

$$\mu_r = n\,z \tag{3.12}$$

and

$$\varepsilon_r = n\,/z \tag{3.13}$$

Throughout this thesis, we used a similar approach to the one outlined in this section where the Kramers-Kronig (K-K) relation is utilized to compute n' uniquely by using the unambiguously computed value of n''. The parameter retrieval code provided by [15] is implemented in this thesis for permeability and permittivity computations.

In the following sections, we will investigate the effect of structural periodicity (i.e. the lattice constant or spatial dispersion effects) of a metamaterial array on the strength of undesired anti-resonant phenomenon. Results of this investigation show that as the metamaterial array becomes denser, the anti-resonance effect gets worse even when the physical size of metamaterial unit cell remains the same. As a demonstration, measures of passivity and causality are examined for a magnetically excited 2-NURR metamaterial topology for varying array periods.

3.3.3 Effects of Having Dense Metamaterial Arrays on the Retrieved Parameters Obtained by NRW method

In this section, performance of the NRW method will be tested in the case of dense metamaterial arrays. Retrieval results will be demonstrated using a magnetically excited 2-NURR metamaterial array.

3.3.3.1 Metamaterial Topology and Simulation Setup

The sparse 2-NURR array (previously designed in section 3.2.1) will be used in this section for simulations under the PEC/PMC boundary conditions. The unit cell topology and computational volume geometry are repeated in Figure 3.14 as a quick reminder. The design parameters are also given below for completeness. The 2-NURR array is designed using Arlon AD-300 substrate and copper inclusions with the following design parameters: L_{sy}= L_{sz}=6.2 mm, ε_r = 3, d = 1.016 mm, tanδ = 0.002, σ = 5.8×10^7 S/m, t = 0.035 mm, w = 0.2 mm, h_1 = 4.6 mm, h_2 = 4.2 mm, l = 4.6 mm and s = 0.2 mm. It should be noted that, in this section, L_{sy} is fixed to L_{sz} while it was chosen equal to p_E for the continuity of the substrate along the p_E direction in section 3.2.1. The schematic top view and design parameters of the unit cell structure for 2-NURR are shown in Figure 3.14(a).The parameters p_E, p_k and $p_H$represent the dimensions of the computational prism along the y-, z- and x- axes as shown in Figure 3.14(b), respectively. Here p_E and p_k are 6.2 mm and 12.8 mm, respectively. Based on the simulation setup and the plane-wave excitation described in Figure 3.14(b), complex S-parameters of the 2-NURR array are computed by CST MWS using the PEC and PMC type boundary conditions as also shown in Figure 3.14(b).

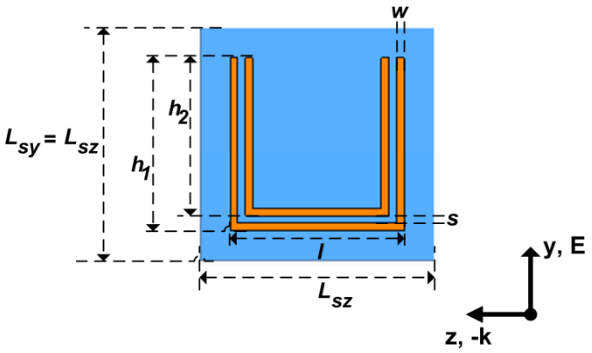

(a)

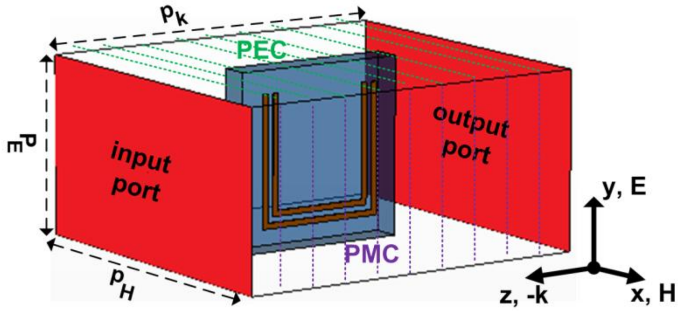

(b)

Figure 3.14: (a) Schematic top view of the 2-NURR unit cell, **(b)** simulation setup.

3.3.3.2 Parameter Retrieval Results for 2-NURR Array for Varying Periodicity, p_H

In this section, we show the effects of changing periodicity along the H field direction, p_H, on the transmission and reflection spectra as well as on the retrieved effective medium parameters, permeability and permittivity.

During the simulations, all design parameters are kept constant except p_H that is changed from 12 mm to 6 mm and then to 2 mm. The resulting S parameter (i.e. $|S_{21}|$ and $|S_{11}|$) curves are plotted in Figure 3.15 displaying two resonance frequencies. Then, the effective relative permeability (μ/μ_0) and effective relative permittivity ($\varepsilon/\varepsilon_0$) are retrieved from the simulated complex S-parameter data for different p_H values using the NRW based improved retrieval algorithm given in [15]. The real (μ') and imaginary (μ'') parts of retrieved (μ/μ_0) are plotted in Figure 3.16 for different p_H

values. Also, real (ε') and imaginary (ε'') parts of retrieved ($\varepsilon/\varepsilon_0$) are presented for the same cases in Figure 3.17.

The simulated metamaterial array is dense along the y-axis but sparse along the x-axis for $p_H = 12$ mm. We make the simulated metamaterial array gradually denser along the x-axis when we change p_H from 12 mm to 6 mm and then to 2 mm. In other words, array elements (i.e., unit cells) get closer to each other along the x-axis when the periodicity p_H is decreased. Thus, magnetic coupling between the array elements become gradually stronger during this procedure.

When we first change p_H from 12 mm to 6 mm, distance between the adjacent unit cells along the x axis is 4.946 mm. For this case, there is no observable change on the position of resonance frequencies while, the transmission curve becomes wider and the resonance dip becomes stronger by only a small fraction as seen in Figure 3.15(a) due to increased coupling between the array elements. When we change p_H from 6 mm to 2 mm, the distance between the adjacent unit cells along the x axis becomes 0.949 mm which is even smaller than the thickness of each unit cell. Thus, for $p_H = 2$ mm, the array becomes very dense causing very strong magnetic coupling between the adjacent unit-cells. For this case, considerable amounts of changes occur in the bandwidths of the transmission and reflection curves, in the strengths of the resonance dips and in the position of resonance frequencies due to these strong coupling effects as shown in Figure 3.15(a).

Before continuing with the retrieval results for permittivity and permeability, the "passivity" requirement (for $e^{-i\omega t}$ convention) will be discussed. It is known that the total dissipated energy W can be expressed as [200]

$$W = \frac{1}{4\pi}\int d\omega\, \omega[\varepsilon''(\omega)|E(\omega)|^2 + \mu''(\omega)|H(\omega)|^2] \qquad (3.14)$$

and $W > 0$ is a compulsory requirement for a passive medium [200]. It is speculated in [200] that this condition does not require that imaginary part for permittivity (ε'') and imaginary part for permeability (μ'') must be simultaneously positive. As long as $W > 0$ is satisfied, having $\varepsilon'' < 0$ or $\mu'' < 0$ does not violate the passive medium condition by itself. On the contrary, Simovski et al. [175] stated that $\varepsilon'' < 0$ and $\mu'' < 0$ mean negative electric and negative magnetic losses, respectively, which are not possible for passive materials. The "passivity" requirement for $e^{-i\omega t}$ convention therefore implies that ε'' and μ'' must be both nonnegative always.

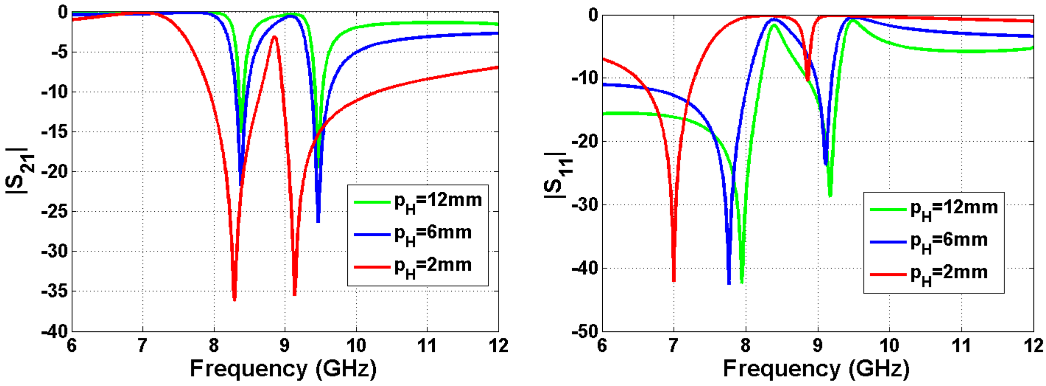

(a) **(b)**

Figure 3.15: (a) $|S_{21}|$ and **(b)** $|S_{11}|$ curves against frequency for varying p_H values.

When we look at the real (μ') and imaginary (μ'') parts of retrieved μ/μ_0 curve plotted in Figure 3.16 for different p_H values, two $\mu' < 0$ (MNG) regions are observed while having $\mu'' > 0$ as required by the passive medium condition. Another observation is that when the array becomes denser (i.e. if we decrease p_H), the MNG bandwidth becomes wider as seen in Figure 3.16(a) where the shape of the μ' curve departs from the expected dispersive "Lorenzian" shape in the case for $p_H = 2$ mm.

On the other hand, resonant behavior of the effective permeability ($\varepsilon/\varepsilon_0$) around resonance frequencies show the anti-resonant behavior (i.e. negative imaginary part for permittivity (ε'') which contradicts with the "passivity" requirement for $e^{-i\omega t}$ convention) as shown in Figure 3.17(b). When we change p_H from 12 mm to 6 mm and then to 2 mm, the anti-resonant behavior becomes gradually stronger. For $p_H = 2\ \mathrm{mm}$, the anti-resonant effect becomes too strong to be neglected.

The cause for anti-resonant effect is commonly but unconvincingly explained in literature as an intrinsic property of a metamaterial array where the unit cell dimensions in not sufficiently small as compared to the wavelength at resonance [205]. When we change p_H, only the coupling effects between the adjacent unit cells are changed while the other factors such as the geometry and physical size of the unit cell remain the same. It is clear that the strong anti-resonant behavior observed around the resonance frequencies for the densely packed array is due to the increased coupling effects between the unit cells which cannot be explained by an over-simplified homogeneous slab model.

In summary, the common retrieval algorithms based on the NRW method may be approximately valid for sparse metamaterial arrays, but they become questionable for densely packed arrays. It is worth to mention that these results are compatible with the results of Alu who also stated that simplistic retrieval approaches fail especially for densely packed arrays [179-180].

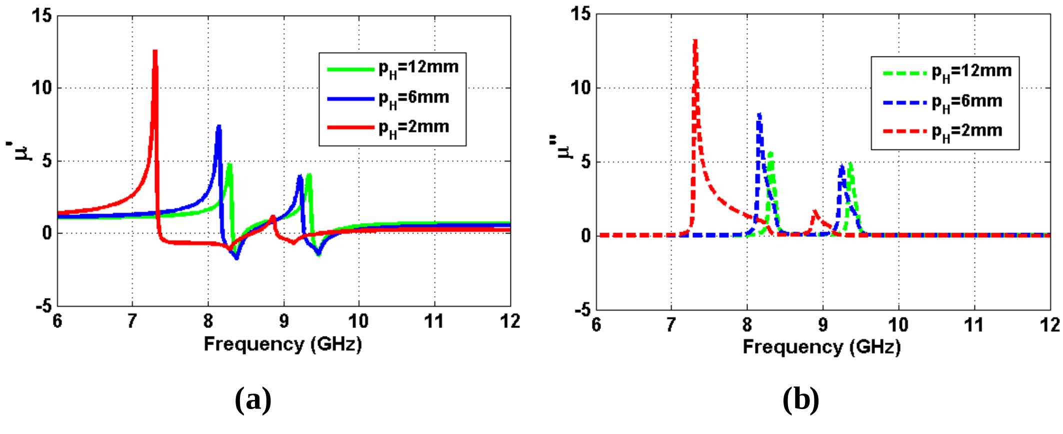

Figure 3.16: (a) Real (μ') and **(b)** imaginary(μ'') part of the retrieved permeability (μ/μ_0) for varying p_H values.

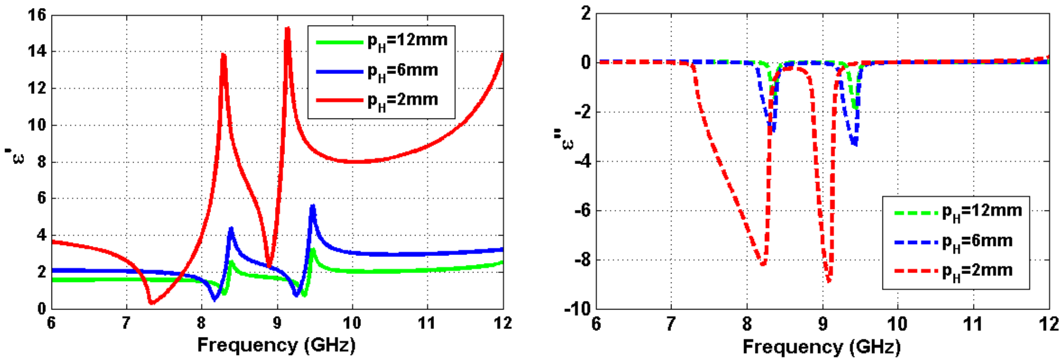

(a) **(b)**

Figure 3.17: (a) Real (ε') and **(b)** imaginary (ε'') part of the retrieved permittivity ($\varepsilon/\varepsilon_0$) for varying p_H values.

3.3.3.3 Checking Causality by Using the Kramers-Kronig Relation

In this section, real parts of retrieved permittivity and permeability curves are calculated from the retrieved imaginary parts of these parameters by using the Kramers-Kronig relation for varying p_H values of the previous section to check for the condition of "causality".

It is well known that the Kramers-Kronig (K-K) relations relate real and imaginary parts of medium parameters, permittivity and permeability. The K-K relations must be satisfied for causality in any physical medium. If we know the real part of any medium parameter we can calculate the imaginary part of this parameter using the K-K relation, and vice versa. In the previous section, the effective relative permeability (μ/μ_0) and effective relative permittivity ($\varepsilon/\varepsilon_0$) curves are retrieved from the simulated complex *S*-parameter data for different p_H values using the common retrieval algorithm given in [15]. Here in this section, we will calculate the real part of the permittivity and permeability from the retrieved imaginary parts for varying p_H values using the K-K relation to check for the condition of "causality".

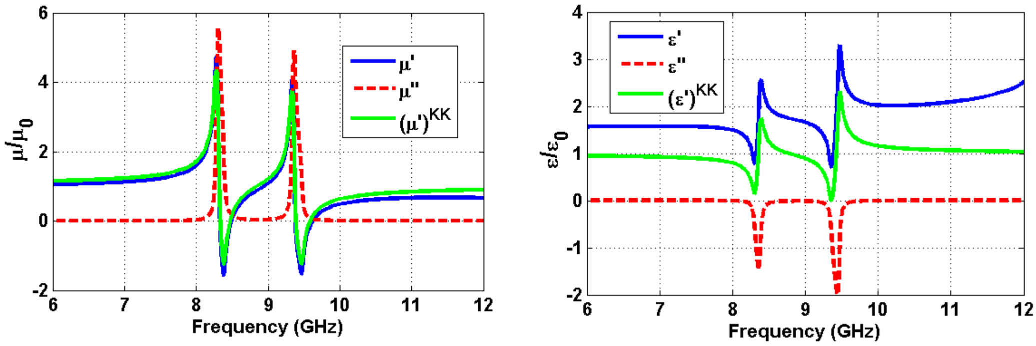

(a) **(b)**

Figure 3.18: For p_H =12mm, **(a)** real (μ') and imaginary (μ'') parts of the μ/μ_0 retrieved by the NRW method and $(\mu')^{KK}$ that is computed from μ'' using the Kramers-Kronig (KK) relation, **(b)** real (ε') and imaginary (ε'') parts of the $\varepsilon/\varepsilon_0$ retrieved by the NRW method and $(\varepsilon')^{KK}$ that is computed from ε'' using the Kramers-Kronig (KK) relation.

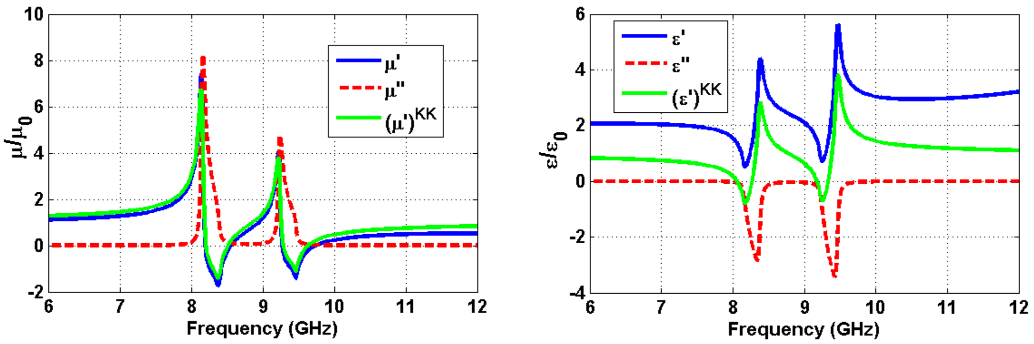

(a) **(b)**

Figure 3.19: For p_H =6mm, **(a)** real (μ') and imaginary (μ'') parts of the μ/μ_0 retrieved by the NRW method and $(\mu')^{KK}$ that is computed from μ'' using the Kramers-Kronig (KK) relation, **(b)** real (ε') and imaginary (ε'') parts of the $\varepsilon/\varepsilon_0$ retrieved by the NRW method and $(\varepsilon')^{KK}$ that is computed from ε'' using the Kramers-Kronig (KK) relation.

For $p_H = 12$ mm, the retrieved real (μ') and imaginary (μ'') parts of the μ/μ_0 are represented as solid blue and dashed red curves, respectively, in Figure 3.18 (a). Similar representations for the retrieved real (ε') and imaginary (ε'') parts of the $\varepsilon/\varepsilon_0$ are shown in Figure 3.18 (b). The real parts of the $\varepsilon/\varepsilon_0$ and μ/μ_0 are calculated from the retrieved imaginary part of these quantities using the K-K relations. The calculated values are represented as solid green curves in Figure 3.18 (a) and Figure 3.18 (b). Superscript "KK" for the $(\varepsilon')^{KK}$ and $(\mu')^{KK}$ imply that these quantities calculated using the K-K relations. Using the similar approach, results for $p_H = 6$ mm and $p_H = 2$ mm are also presented in Figure 3.19 and Figure 3.20, respectively.

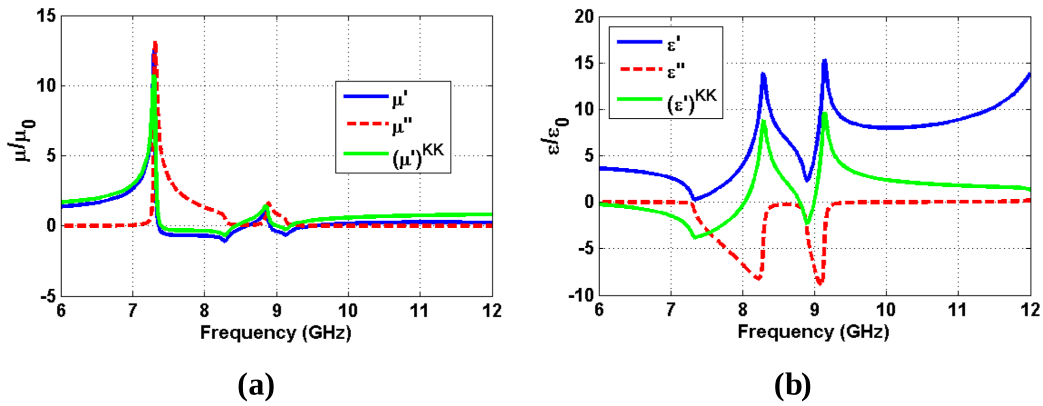

Figure 3.20: For p_H=2mm, **(a)** real (μ') and imaginary (μ'') parts of the μ/μ_0 retrieved by the NRW method and $(\mu')^{KK}$ that is computed from μ'' using the Kramers-Kronig (KK) relation, **(b)** real (ε') and imaginary (ε'') parts of the $\varepsilon/\varepsilon_0$ retrieved by the NRW method and $(\varepsilon')^{KK}$ that is computed from ε'' using the Kramers-Kronig (KK) relation.

As seen in Figure 3.18(a-b) for the sparse array with $p_H = 12$ mm, the calculated $(\mu')^{KK}$ and the retrieved μ' are almost the same while there is a noticeable difference between the retrieved ε' and the calculated $(\varepsilon')^{KK}$. On the other hand, ε'' becomes negative violating the "passivity" condition. When we change p_H from 12 mm to 6 mm, $(\mu')^{KK}$ and μ' are still very similar as seen in Figure 3.19(a) but discrepancy between the retrieved ε' and calculated $(\varepsilon')^{KK}$ increase strongly. Also, ε'' reaches to deeper negative values. This situation becomes even worse, for the case of dense array with $p_H = 2$ mm. The imaginary part of permittivity (ε'') becomes very strongly negative as the metamaterial array becomes denser. The real part of permittivity (ε') shows very strong and physically unexpected variations with frequency, getting very close to zero level, becoming even negative around resonance frequencies. In other words, the condition for causality is violated more strongly for the densely packed arrays (i.e. for the smaller values of p_H).

These observations show that the parameter retrieval results based on the "homogeneous slab model" become more questionable for densely packed metamaterial arrays. These results raise serious doubts for the validity of the NRW parameter retrieval approach, in general, calling for the need for more reliable and topology independent alternative approaches as a future study.

CHAPTER 4

DESIGN OF NOVEL MULTI-BAND METAMATERIALS: NESTED RING RESONATORS

In this chapter, two novel MNG type multi-band metamaterial designs are introduced; an M-band nested split ring resonator (*M*-NSRR) and an *M*-band nested U-ring resonator (*M*-NURR). The single-sided and double-sided (in broadside-coupled configuration) versions of the *M*-NURR are also demonstrated on a comparative basis for the purpose of improved miniaturization. At the end of the chapter, nested ring resonators in different shapes are also presented. This chapter is mainly constructed by combining our results which have been already published in [43-45, 49] as the outcomes of this thesis research.

4.1 Introduction

Metamaterials are designed, not necessarily but usually, as periodic arrays of sub-wavelength unit cells in microwave and terahertz regions. As opposed to natural materials, they can display negative effective permittivity (ε) and/or negative effective permeability (μ) over certain frequency bands. As discussed in Chapter 2 earlier, artificial plasma type ε-negative (ENG) metamaterials, built by periodic arrays of wires or metallic plates, have been shown to have very broad ENG bands below their plasma frequencies [5]. Arrays of conventional SRR and spiral resonator (SR) unit cells, on the other hand, are well known topologies behaving as μ-negative (MNG) metamaterials under magnetic excitation over narrow frequency bands around their fundamental (*LC*) resonance frequencies [206]. Combining the above mentioned ENG and MNG structures within the same unit cell, metamaterials with negative refractive indices can be realized [10]. Bandwidths of resulting metamaterials are limited by the narrow-band behavior of MNG structures. In the absence of sufficiently broadband metamaterials, design of multi-band structures is highly desired for various applications in microwave and optics regimes.

It has been demonstrated that design of conventional SRR or SR (Spiral resonator) unit cells with increased number of rings (or turns) helps to realize considerable amounts of miniaturization, however, the resulting metamaterial structures still display the single-band MNG behavior [31]. Compact multi-band MNG unit cells can be designed by using metallic inclusions having more complicated geometries as compared to the conventional SRR or SR structures [37, 181-185]. Or alternatively, MNG topologies resonating at two or three different frequencies can be designed by using periodic arrays of super cells, which are composed of two or more slightly different or asymmetrical individual unit cell structures [35, 186-188]. Multi-band metamaterials are obtained by these approaches in the expense of either increased electrical size or increased structural complexity. In metamaterial design, having small electrical size is important not only for miniaturization concern but also to satisfy the conditions for the effective medium approach more closely. Simplicity of the unit cell geometry is another design requirement needed for lower fabrication errors especially at shorter wavelengths of terahertz regime. In section 4.2, the *M*-band nested split ring resonator (M-NSRR) having a small and geometrically simple unit cell is introduced and investigated numerically as a multi-band MNG type metamaterial. In section 4.3, design and simulation procedures, fabrication and measurement processes for the *M*-band nested U-ring resonator (*M*-NURR) are given as the modified simpler version of the M-NSRR topology. In section 4.4, further miniaturization of the M-NURR topology is demonstrated. In section 4.5, nested ring resonators with different topologies are compared.

4.2 *M*-band Nested Split Ring Resonators: Multi-Ring SRR Type Metamaterial Design with Multiple Magnetic Resonances

In this section, a new *M*-band nested SRR (*M*-NSRR) unit cell design is introduced for multi-band metamaterial applications. The suggested unit cell structure consists of *M* number of concentric split rings with aligned gap positions to obtain magnetic resonances at M distinct frequencies. Value of each distinct resonance frequency can be adjusted by changing design parameters. For a given substrate material, design parameters are the side lengths, widths of metal strips, gap distances for each ring, and the separation distances between the rings. As a proof of concept, several M-NSRR arrays are designed and simulated in this section for three different cases as M = 1, 2 and 3 by using CST Microwave Studio. Complex transmission and reflection spectra (i.e. the complex S-parameters S_{21} and S_{11}) of the proposed M-NSRR arrays are obtained by CST, and then they are used to extract the effective medium parameters μ and ε of the designed metamaterials to verify the nature of resulting resonances. The basic retrieval procedure given in [164] is used for parameters estimation, which provides approximately valid results in the case of reasonably sparse metamaterial arrays.

4.2.1 Design and Simulations

The schematic view of the proposed multi-ring unit cell M-NSRR for the case of M = 3 and the associated simulation setup are shown in Figure 4.1(a) and (b) together with the excitation details where wave propagation is in the direction of x-axis, incident H field is perpendicular to the SRR plane (i.e. in the direction of z-axis) and the incident E field is perpendicular to the gap containing edges of the SRR rings (i.e. in the direction of y-axis). A cubic computational region with a side length of 7.5 mm is used in the simulation procedure as shown in Figure 4.1(b). PEC type boundary conditions are applied at the boundary surfaces perpendicular to E field while PMC type boundary conditions are applied at the boundary surfaces perpendicular to H field. Remaining boundaries are defined as the input and output ports. Using this setup, infinitely large metamaterial arrays are simulated due to the imaging effects of the applied PEC and PMC type boundary conditions as explained in detail in Chapter 3. As examples, M-NSRR arrays are designed and simulated for M= 1, 2, 3 on a planar substrate having the relative permittivity of 4.4 and the loss tangent of 0.001. Metallic inclusions are made of copper with the thickness of 0.035 mm and the conductivity of 5.8×10^7 S/m.

The square-shaped substrate has side length D =7.5 mm along the x and y directions with thickness of 0.6mm in the z direction as shown in Figure 4.1 (a). Design parameters for square-shaped rings are the side lengths (L), gap distances (g) and metal strip widths (w) of the SRR metal rings as well as rings-to-ring separations s.

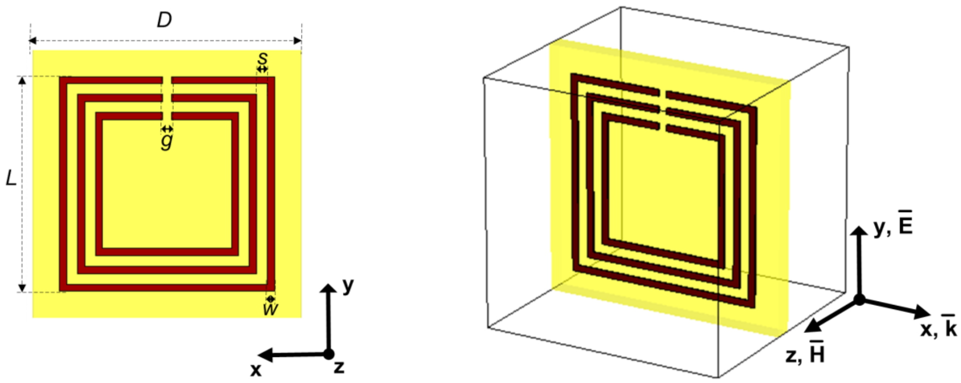

(a) **(b)**

Figure 4.1: (a) The schematic view of 3-NSRR. **(b)** Simulation setup and the excitation.

Each one of the 1-NSRR arrays simulated in the first step of this work are composed of only one size of single-ring square-shaped unit cell shown in Figure 4.2 where the side lengths (L) of the SRR metal rings are chosen to be 6 mm, 5 mm and 4 mm for the SRR-A, SRR-B and SRR-C type unit cells, respectively. The same gap distance g = 0.25 mm and the same metal strip width w = 0.2 mm are used in these three different unit cells.

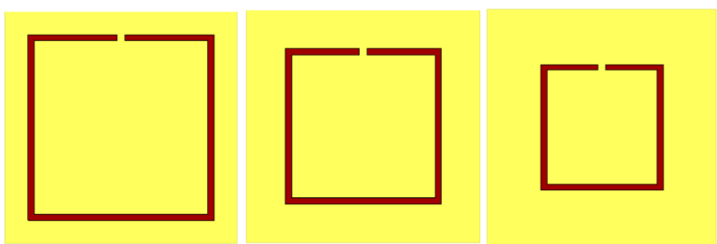

(a) SRR-A **(b)** SRR-B **(c)** SRR-C

Figure 4.2: Front view of the single-ring square-shaped SRR unit cells with different parameters.

In the next step, a two-ring SRR unit cell (2-NSRR) is designed by combining the SRR-A and SRR-B unit cell topologies which are aligned in the gap-to-gap configuration as shown in Figure 4.3(a). Similarly, a three-ring SRR unit cell (3-NSRR) is also designed by combining all three types of unit cells SRR-A, SRR-B and SRR-C as shown in Figure 4.3(b). In both of these configurations, the distance between the rings is chosen to be s=0.3 mm.

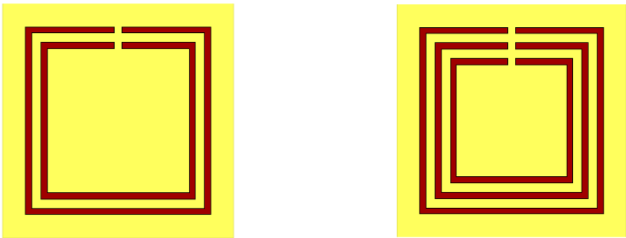

(a) **(b)**

Figure 4.3: Multi-ring SRR unit cell structures with two and three-rings**: (a)** 2-NSRR, and **(b)** 3-NSRR.

4.2.2 Results: Transmission and Reflection Spectra, and the Effective Medium Parameters

Complex S-parameters S_{21} and S_{11} computed for the single-ring array topologies based on the use of SRR-A, SRR-B or SRR-C revealed magnetic resonance frequencies at 4.24 GHz, 5.34 GHz, and 6.77 GHz, respectively. The magnitude and phase plots for these transmission and reflection spectra are shown in Figure 4.4(a) through 4.4(d). Increase in the side length (and hence in the overall length) of the metal ring results in an increase of the self inductance [207] leading to a decrease in the LC resonance frequency of the resonator, as expected.

Next, the magnitude and phase spectra of S_{21} and S_{11} parameters are computed for the 2-NSRR topology of Figure 4.3(a). Resulting plots are given in Figure 4.5 together with the plots for the real and imaginary parts of the retrieved parameters, effective relative permittivity and effective relative permeability. As seen in Figure 4.5, the 2-NSRR array structure has three distinct resonances over the range from 1 GHz to 10

GHz. Two of those frequencies at 4.01 GHz and 5.19 GHz are magnetic *LC* resonances and the last one at 8.96 GHz is an electric dipole resonance.

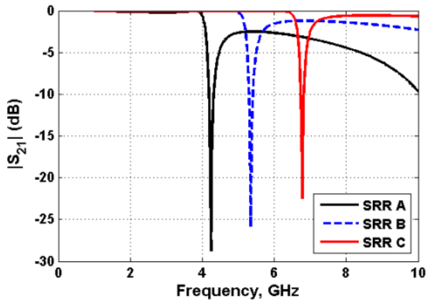

(a) Magnitude of S_{21}

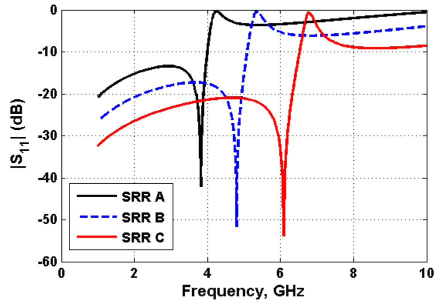

(c) Magnitude of S_{11}

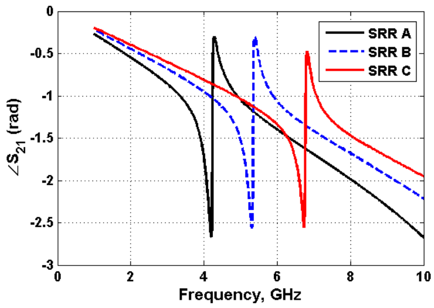

(b) Phase angle of S_{21}

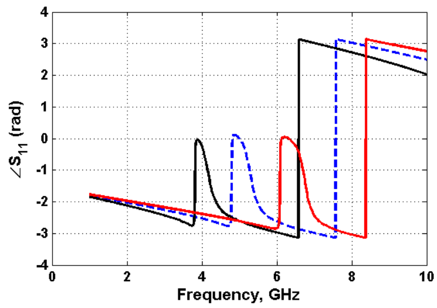

(d) Phase angle of S_{11}

Figure 4.4: Transmission and reflection spectra of the 1-NSRR arrays shown in Figure 4.2.

As shown in Figure 4.6, on the other hand, the 3-NSRR array has four distinct resonances. Three of them (at 4.1 GHz, 5.05 GHz and 6.53 GHz) are magnetic *LC* resonances and the one at 8.95 GHz is again an electric dipole resonance. These results demonstrate that a desired number of magnetic resonances can be realized by selecting the number of SRR rings within the limits of geometrical constraints. It is also worth mentioning that resonance frequencies can also be adjusted by changing the design parameters *g*, *w* and *s*.

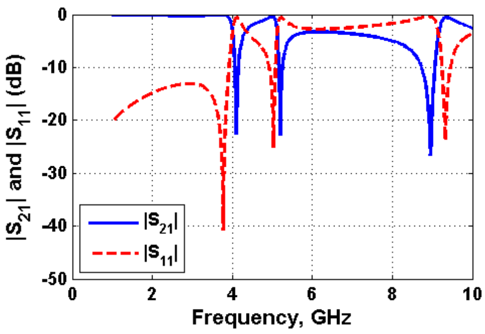

(a) Magnitudes of S_{21} and S_{11}

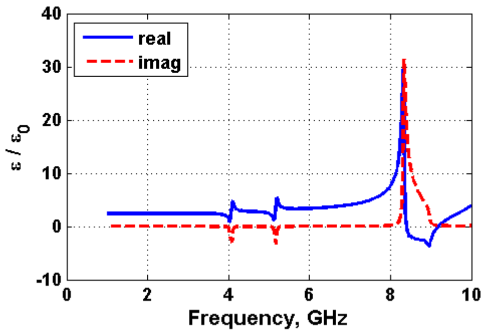

(c) Real and imaginary parts of relative permittivity

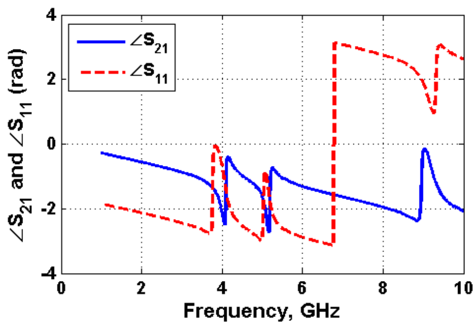

(b) Phase angles of S_{21} and S_{11}

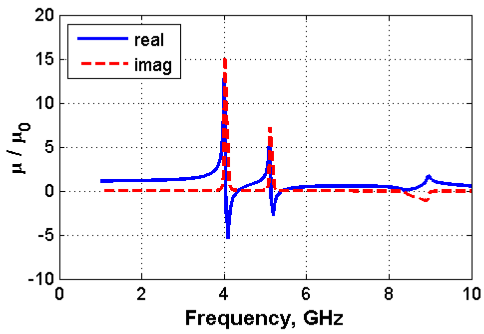

(d) Real and imaginary parts of relative permeability

Figure 4.5: Transmission and reflection spectra, and the effective medium parameters for the 2-NSRR array.

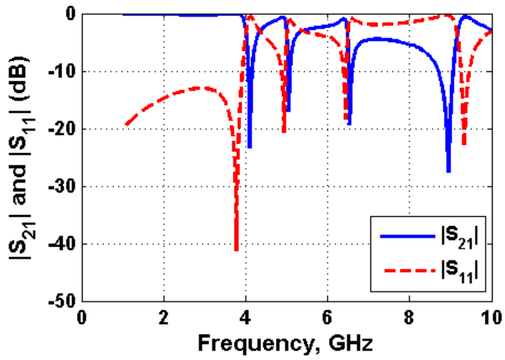

(a) Magnitudes of S_{21} and S_{11}

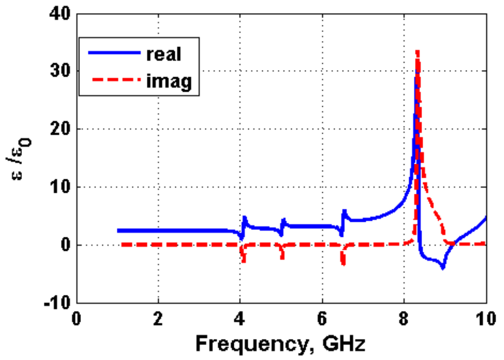

(c) Real and imaginary parts of relative permittivity

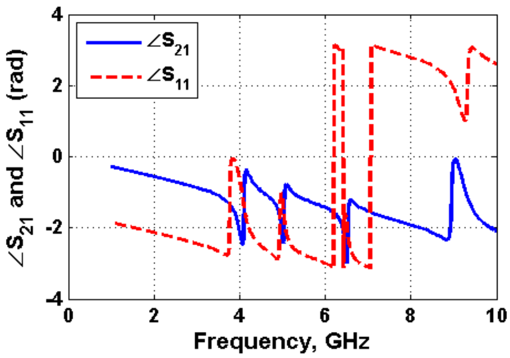

(b) Phase angles of S_{21} and S_{11}

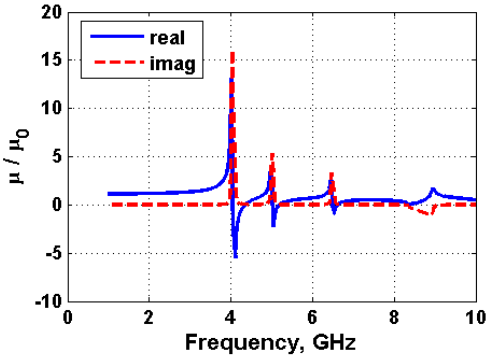

(d) Real and imaginary parts of relative permeability

Figure 4.6: Transmission and reflection spectra, and the effective medium parameters for the 3-NSRR array.

Besides retrieving the effective medium parameters of the structure, two additional methods can be performed to reveal the nature of the resonances. The first one is observing the surface current densities at resonance frequencies. For this purpose, surface current densities for the 3-NSRR at each resonance frequency are presented in Figure 4.7. As shown in this figure, there is a strong circulating current distribution in the outermost ring for the resonance at 4.10 GHz, in the middle ring for the resonance at 5.05 GHz and in the innermost rings for the resonance at 6.53 GHz. In contrast to the first three resonances, there is strong dipole-related current distribution in the outermost ring producing a weak current distribution in the adjacent middle ring due to coupling effects at the fourth resonance at 8.95 GHz. The first three resonances are magnetic *LC* resonances arising from inductance of the rings and the capacitance of the gaps created due to the circulating current induced along the rings. On the other hand, the last one is an electrical resonance arising from dipole-related current distributions on the vertical arms of the outermost and middle rings while the innermost ring is not affected significantly during this procedure. Furthermore, while only one ring is responsible for creating each magnetic *LC* resonance, slight current activities are observed in the adjacent rings due to coupling affects. For example, the first *LC* resonance at 4.10 GHz is associated basically with the induced current in the outermost ring while the resulting magnetic flux is coupled to the middle ring resulting in an oppositely directed and weaker secondary induced current. The coupling effects observed in the inner ring is negligible. Due to the effects of these "secondary" induced currents, the resonance frequency shifts from 4.24 GHz (for the SRR-A type 1-NSRR array) to 4.10 GHz (for 3-NSRR array). Similarly, the second resonance at 5.05 GHz is primarily associated with the middle ring while current activities in the adjacent outermost and innermost rings are the results of magnetic coupling mechanism, which in turn leads to the shift of middle ring resonance frequency 5.34 GHz to 5.05 GHz. As for the third resonance at 6.53 GHz, it is dominantly related to the current activities in the innermost ring while its value is somewhat affected by the secondary current activities in the adjacent middle ring, resulting a resonance frequency shift from 6.77 GHz to 6.53 GHz

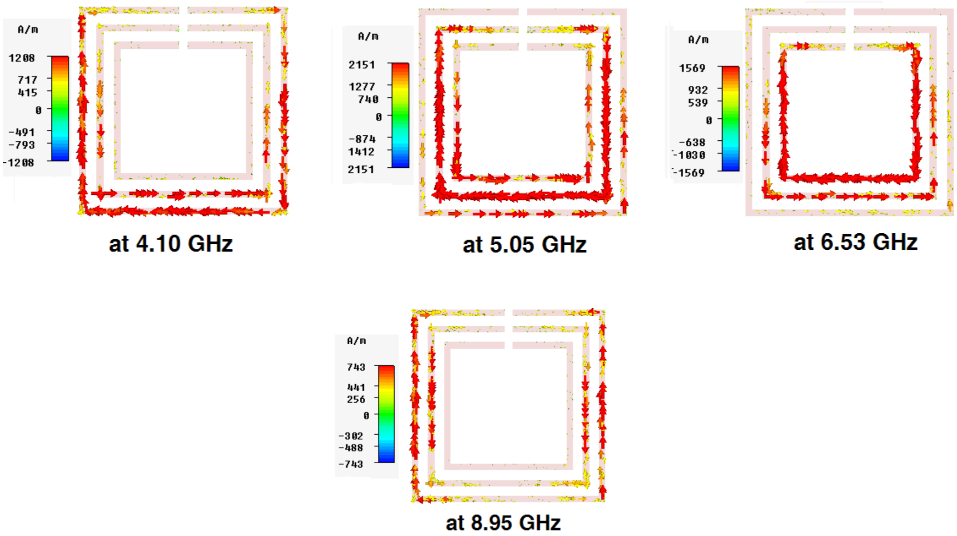

Figure 4.7: Surface current densities for the 3-NSRR at each resonance frequency

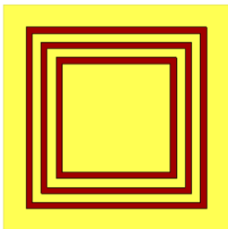

(a)

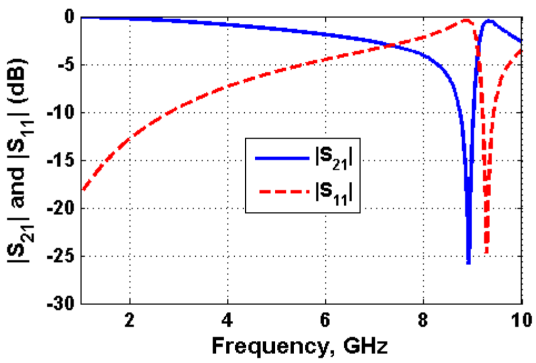

(b)

Figure 4.8: (a) 3-NSRR with closed gaps. **(b)** Transmission and reflection spectra for the 3-NSRR with closed gaps.

The simple alternative method to verify the presence of LC resonances is to complete the rings by removing the gaps. We know that, by closing a ring, the gap capacitance is removed, hence the inductive-capacitive (LC) resonance of the structure disappears. For the proof of this concept, the 3-NSRR structure without any gaps is presented in Figure 4.8(a). Magnitudes of transmission and reflection spectra of the simulated 3-NSRR with closed gaps are presented in Figure 4.8(b) displaying only the dipole resonance around 8.95 GHz. The other three resonances of the 3-NSRR structure disappear when the gaps are closed. This test verifies that disappeared resonances of the 3-NSRR at 4.10GHz, 5.05 GHz and 6.53 GHz are indeed LC type resonances.

4.2.3 Effects of the Design Parameters on the Resonance Behavior of the 3-NSRR Structure

In this section, we will demonstrate the effects of changing design parameters g, w and s on the resonance frequencies of the 3-NSRR structure. During all the parametric studies, the side length (L) of the outermost ring is kept fixed.

Before presenting the results of parametric studies, expression for the LC resonance frequencies will be examined in detail to clarify the reasons behind the changes in resonance frequencies that will occur in response to parameter variations.

A given magnetic resonance frequency (ω_{res}) of the 3-NSRR topology is expressed as

$$\omega_{res} = 2\pi f_{res} = 1/\sqrt{L_T C_T} \qquad (4.1)$$

due to series-LC resonant circuit nature of single-SRR rings. In this expression, L_T is dominantly composed of the self inductance (L_{self}) of the associated split ring, although its value is somewhat affected by mutual inductance term (L_{mut}) caused by the magnetic coupling due to nearby split rings. The term C_T in equation (4.1) is composed of the parallel plate capacitance C_{pp} and co-planar capacitance C_{cp} terms. When capacitive coupling between neighboring ring is negligible, the total capacitance C_T can be approximated by the gap capacitance (C_{gap}) only. The expressions for L_{self} [208] and C_{gap} [209-210] can be given as

$$L_{self} \approx \frac{2\mu_0 L}{\pi}\left[sinh^{-1}\left(\frac{L}{w/2}\right) - 1\right] \tag{4.2}$$

where L is the side length of the metal ring, w is the ring width and μ_0 is the permeability of free space,

$$C_{gap} = C_{pp} + C_{cp}$$

$$= \varepsilon \frac{wt}{g} + \frac{(\varepsilon_r+1)\varepsilon_0}{2\pi} ln\left[2\frac{1+\sqrt{k'}}{1-\sqrt{k'}}\right] \quad \text{F/m} \tag{4.3}$$

$$k' = \sqrt{\left(1-\left(\frac{p}{p+2q}\right)^2\right)} \tag{4.4}$$

In the above, t is the thickness of the metal ring layer, g is the gap width, $\varepsilon = \varepsilon_r\varepsilon_0$ is the permittivity of the substrate. In equation 4.4, p = gap width and $q = \frac{L-g}{2}$ must be used.

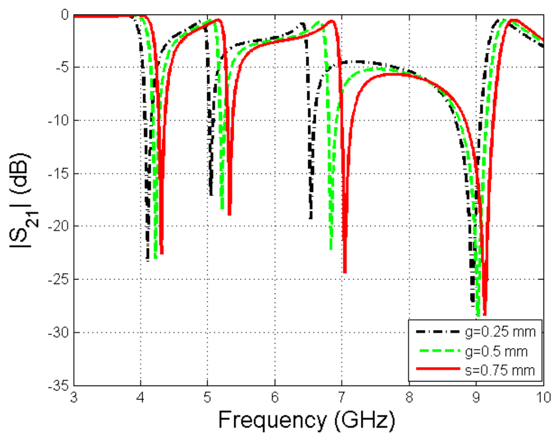

Figure 4.9: Transmission spectra of the 3-NSRR topology for different values of the gap distance (g).

As the first parametric study, the effects of gap distance (g) on the values of resonance frequencies are investigated. The transmission spectra shown in Figure 4.9 are obtained for g=0.25 mm, g=0.5 mm and g=0.75 mm. When g is simultaneously increased by the same amount for each ring, capacitances at the gap locations (see Equation 4.3) decrease leading to higher resonance frequencies for as shown in Figure 4.9. Despite the same amount of increase in g for each ring, the highest change is observed for the third magnetic LC resonance which is strongly related to the innermost ring. Since the innermost ring is smaller compared to the other two rings, the percentage change in the ring inductance (caused by the gap width change) of this inner ring is larger. Therefore, the relative increase in the resonance frequency f_{res} becomes more pronounced.

Next, the simulation results are obtained for three different ring-to-ring separation (s) values. Black, green and red curves show the transmission spectra of the 3-NSRR structure for the ring- to-ring separation s = 0.2 mm, s = 0.3 mm and s = 0.4 mm, respectively, in Figure 4.10. When we increase the ring-to-ring separation, resonance frequencies of the structure are shifted to higher values as presented in Figure 4.10. Since the length of outermost ring is fixed during the parametric study, the value of the first resonance (f_1) which is strongly related to the current activity on this ring is almost the same. Very small amount of change in its value is due to the decrease in weakened magnetic coupling between the rings in response to the movement of the outermost and middle rings away. As s is increased, besides the decrease in the coupling effects, there is also a decrease in the inductance (see Equation 4.2) of middle and inner rings due to shortened ring lengths. Thus, more pronounced increases in the second resonance (f_2) and especially in the third resonance (f_3) are observed in Figure 4.10. As for the fourth resonance, its value also shifted to higher values with the increase in s. When s is increased, the outermost and middle rings are moved away from each other leading to weakened coupling effect between the effective electric dipoles. Thus, the value of fourth resonance frequency (f_4) slightly changes.

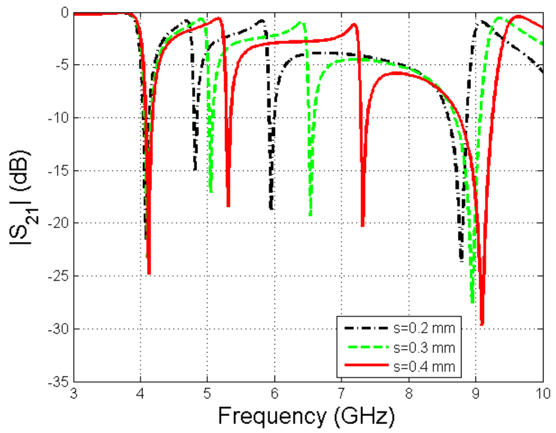

Figure 4.10: Transmission spectra of the 3-NSRR topology for different values of the ring- to-ring separation (s).

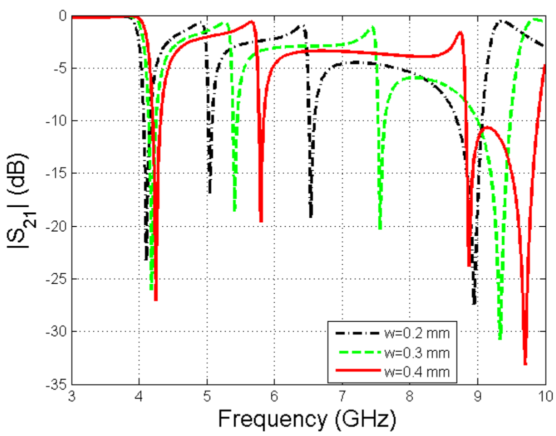

Figure 4.11: Transmission spectra of the 3-NSRR topology for different values of the metal thickness (*w*).

Finally, the width of the metal strip (*w*) of each ring is changed keeping the side length of the outermost ring (*L*) fixed. The black, green and red curves shown in Figure 4.11 demonstrate the transmission results for the simulated structures for *w* taking the values 0.2 mm, 0.3 mm and 0.4 mm, respectively. When we increase *w*, each resonance frequency of the structure is shifted to upper frequencies. Since the length of the outermost ring is kept fixed during the parametric study, the value of the first *LC* resonance is shifted to higher values mainly due to decrease in the inductance (see Equation 4.2) of this ring with its increased *w*. Furthermore, besides the decrease in the self-inductance of each ring with its increased width w, self-inductances of the middle and innermost rings decrease markedly due to smaller ring lengths. Thus, more pronounced increases in the second and third LC resonances are observed in Figure 4.11 due to a higher change in self-inductances of the rings.

As inferred from the preceding parametric study, positions of the resonance frequencies of the 3-NSRR can be shifted to desired values by tuning the design parameters. In other words, based on these parametric analysis results, M-NSRR structure, in general, can be modified to obtain desired effective medium parameters as briefly outlined below:

First, by adjusting design parameters of the individual rings, three distinct magnetic LC resonance curves of the M-NSRR structure can be merged into one resonance curve for the purpose of enhancing the MNG bandwidth. This approach will be presented in detail in the section 4.3.2.4 for 3-NURR structure.

Second, by adjusting design parameters of the innermost ring only (which seems to be contributing to the dipole resonance very weakly), the third magnetic LC resonance of the 3-NSRR structure might be shifted close to the dipole resonance of the structure to obtain negative effective refractive index (n) region around the electric dipole resonance. Thus, the modified 3-NSRR structure may have two MNG regions as well as one DNG region.

Third, the M-NSRR topology can be turned into a DNG type metamaterial having multi-band negative refractive index. As explained in the chapter 2, negative n can be achieved over a specific frequency band by combining a material with negative ε (ENG material such as the periodic wire array media) and another material with negative μ (MNG material such as an SRR array) if their ENG and MNG regions overlap. Using the same idea, the periodic wire media which has a very wide ENG band below the plasma frequency (ω_p) can be combined with the M-NSRR array which has negative μ at N narrow distinct frequencies to obtain negative n at distinct multi frequency regions. Thus, if a metal strip is placed on the back side of the substrate in the *M*-NSRR unit cell, *M* distinct multi-DNG regions can be obtained provided that resonance frequencies $f_1, f_2, \ldots, f_m$ are all smaller than the plasma frequency of the ENG array.

4.3 Nested U-Ring Resonators: A Novel Multi-Band Metamaterial Design in Microwave Region

In this section, a novel metamaterial topology, called *M*-band nested U-ring resonator (*M*-NURR), is proposed to provide multiple band operation with an electrically small and geometrically simple unit cell design. The *M*-NURR unit cell has *M* nested and unconnected U-shaped metal rings printed on a dielectric substrate where each ring is primarily associated with a distinct *LC* type resonance frequency where *L* and *C* stand for inductance and capacitance, respectively. In general, a time-varying incident magnetic field having a component normal to the surface of a split-ring induces a magnetic dipole with a circulating current along the conducting ring. At the same time, charge densities with opposite polarities are induced across the split ends of the ring. Due to the resulting inductive and capacitive effects, the metamaterial cell behaves as a series *LC* resonant circuit with resonance frequency $\omega_0 = 2\pi f_0 = (LC)^{-1/2}$. As discussed in [8, 20] at frequencies well below the resonance, response of the induced magnetic dipole is in phase with the incident field showing paramagnetic response. As the frequency of external field approaches the resonance frequency, magnetic dipole moment begins to lag. At a certain value above the resonance frequency, the induced dipole moment becomes completely out of phase with the excitation field resulting in a diamagnetic response with permeability values smaller than unity or even smaller than zero. This phenomenon is explained by the Lorentz oscillator model and, the real part of the complex-valued effective permeability function has the Lorentzian form displaying negative permeability values over a narrow frequency band. Accordingly, each nested U-ring of the *M*-NURR cell leads to an individual resonance giving rise to a separate negative permeability region. Unless those resonance frequencies are too close to each other (sufficiently close to have overlapping resonance curves), each resonance frequency of the M-NURR topology is strongly associated with a specific U-ring and it can be efficiently tuned by changing the arm length of this U-ring only, with negligible effects on the rest of the resonance frequencies. In conventional SRR based multi-band metamaterial structures, changing any design parameter affects all of the resonance frequencies to some noticeable extent due to both geometry and the inter-cell coupling effects. To the best of our knowledge, having "almost independently controllable resonance frequencies" is an important advantage of the proposed M-NURR structure not demonstrated in the other multi-band metamaterial designs reported in literature.

Here, three different M-NURR structures (for $M = 1, 2, 3$) are designed, fabricated and characterized both numerically and experimentally with very good agreement. The suggested sub-wavelength M-NURR metamaterial topology is anticipated to be useful in the design of miniaturized multi-band mobile communication devices as it makes the fine tuning of operation frequencies possible by a simple parametric adjustment.

4.3.1 Design, Simulations and Measurements

As the first step of design, fabrication and characterization process, basic topology and design parameters of the M-NURR unit cell are defined as shown in Figure 4.12(a) for $M = 3$ case, which are the side length of square-shaped substrate (L_s), base length of the outer U-ring (l), arm lengths of the U-rings (h_{1L}, h_{2L}, h_{3L}) on the left side and (h_{1R}, h_{2R}, h_{3R}) on the right side of the cell, width of the metal strips (w), vertical separation distance between the rings (s_e), horizontal separation distances between the rings (s_{kL}) on the left side and (s_{kR}) on the right side of the 3-NURR cell. Additional design parameters are conductivity (σ) and thickness (t) of the metal traces as well as relative permittivity (ε_r), thickness (d) and loss tangent ($tan\delta$) of the substrate. In this study, we have used Arlon AD-300A type substrate with copper metallization having parameters $\varepsilon_r = 3$, $d = 1.016$ mm, $\tan\delta = 0.002$, $\sigma = 5.8\times10^7$ S/m, $t = 0.035$ mm to design and fabricate three unit cells, 1-NURR, 2-NURR and 3-NURR (for the cases $M = 1, 2, 3$) with parameter values $L_s = 6.5$ mm, $w = 0.32$ mm, $s_e = s_{kL} = s_{kR} = 0.28$ mm, l

= h_{1L} = h_{1R} = 4.8 mm, h_{2L} = h_{2R} = 4.2 mm and h_{3L} = h_{3R} = 3.6 mm by using LPKF-ProtoMat-H100 circuit board plotter. Photographs of the fabricated unit cells are shown in Figure 4.12(b).

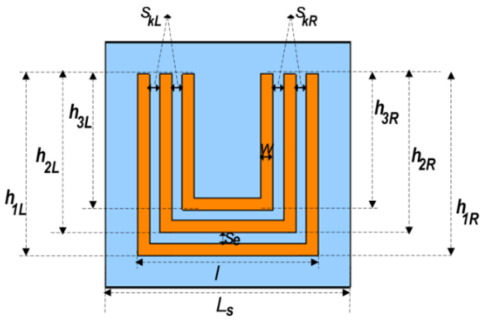

(a)

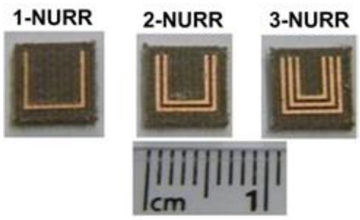

(b)

Figure 4.12: Designed and fabricated *M*-NURR unit cells. **(a)** Design parameters shown for a 3-NURR unit cell. **(b)** Photographs of the fabricated *M*-NURR unit cells for M = 1, 2, and 3.

In this work, we use CST Microwave Studio, for numerical simulation of the designed *M*-NURR arrays within an X-band rectangular waveguide setup that is used for experimental characterization of the fabricated *M*-NURR prototypes. The complex valued *S*-parameters of these metamaterial structures are first computed by CST Microwave Studio and then measured by a network analyzer (Agilent 8750D) that is combined with the waveguide setup. The *M*-NURR unit cell is placed at the centre of the measurement waveguide as shown in Figure 4.13(a) so that its *LC* resonances are magnetically excited by the H_x magnetic field component of the fundamental TE_{10} waveguide mode (as anticipated by the Faraday's law) over the single mode operation range extending from 6.56 GHz to 13.73 GHz. An infinitely large double-periodic *M*-NURR array is simulated by this measurement setup based on the well-known imaging effect of the copper walls of the waveguide. This real-world scenario is modelled in CST simulations by imposing PEC (perfect electric conductor) type boundary conditions at all four boundaries of the computational volume as shown in Figure 4.13(a). Dimensions of this X-band waveguide determine the spatial periods, p_E=10.16 and p_H =22.86 mm, of the simulated *M*-NURR array along the *y* and *x* axes, respectively. Photograph of the waveguide set up is shown in Figure 4.13(b) indicating sample holder part's length as p_k =12.8 mm along the propagation direction.

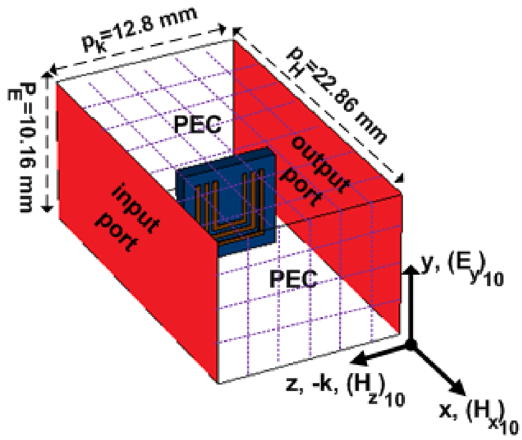

(a)

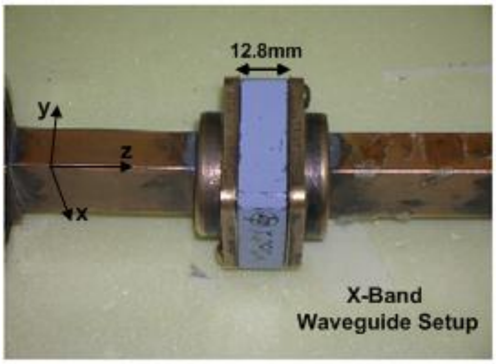

(b)

Figure 4.13: X-band waveguide setup used for numerical and experimental characterizations. **(a)** Simulation setup, and **(b)** measurement setup.

Simulated and measured transmission spectra ($|S_{21}|$ versus frequency) as well as reflection spectra ($|S_{11}|$ versus frequency) for the 1-NURR array are presented in Figure 4.14(a) displaying only one resonance at 8.59 GHz in simulations and at 8.62 GHz in measurements with only 0.35 percent error. Next, similar results for the 2-NURR are presented in Figure 4.14(b) verifying the presence of two closely located resonances at 8.26 GHz and 10.05 GHz in simulations, and at 8.59 GHz and 10.33 GHz in measurements. Finally, the simulated and measured transmission and reflection spectra of 3-NURR are given in Figure 4.14(c) with three distinct resonances at 8.24 GHz, 9.86 GHz and 12.42 GHz in simulations and at 8.58 GHz, 10.31 GHz and 12.79 GHz in experiments, respectively.

In case of 2-NURR and 3-NURR characterizations, errors between simulated and measured resonance frequencies are found within acceptable limits (less than five per cent in the worst case) but they are not as small as the error observed in the case of 1-NURR characterizations. These relatively higher errors can be explained by the presence of small ring-to-ring separations (s_{kL}, s_{kR} and s_e) in the 2-NURR and 3-NURR topologies. It is quite possible that small deviations may occur in the values of design parameters due to fabrication errors. As to be demonstrated in Sec. 4.3.2.1, small variations in these separation distances may cause noticeable shifts in resonance frequencies of the 3-NURR structure. Numerical errors due to mesh generation schemes may also occur in simulations contributing to differences between measured and computed resonance frequencies especially when a simulated M-NURR structure contains very fine details such as those narrow gaps between the nested U-rings.

Simulated and measured absorbance spectra $A(f) = 1 - |S_{11}(f)|^2 - |S_{21}(f)|^2$ of the 3-NURR array are also presented in Figure 4.14(d) to illustrate the extent of overall losses caused by non-zero conductivity of the dielectric substrate material and the finite conductivity of thin layers of copper inclusions. Metamaterials are known to be lossy structures, in general. While their loss characteristics may limit the use of metamaterials in some applications, this drawback can be turned into an advantage in the design of metamaterial absorbers [83].

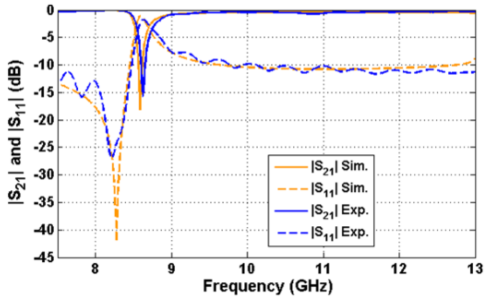

(a)

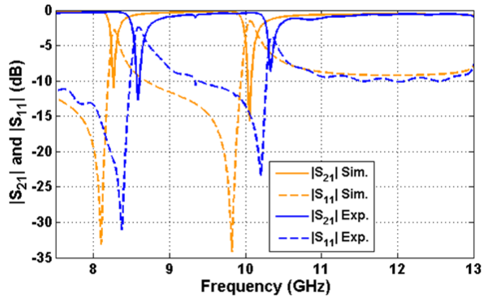

(b)

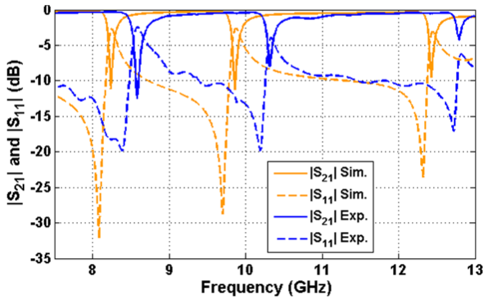

(c)

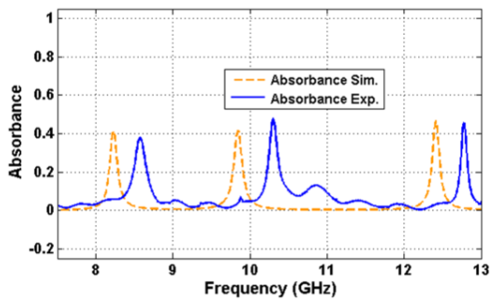

(d)

Figure 4.14: Simulated and measured spectra of transmission, reflection and absorbance. **(a)** Transmission and reflection for the 1-NURR array. **(b)** Transmission and reflection for the 2-NURR array. **(c)** Transmission and reflection for the 3-NURR array. **(d)** Absorbance for the 3-NURR array.

As demonstrated in Figure 4.14(a-c), transmission spectrum of an M-NURR structure contains M distinct and narrow stop bands which make this topology a natural candidate for the design of multiple-stop-band filters and possibly multi-band notch filters. As a matter of fact, with its simple geometry, small electrical size and easily tuned multi-band capabilities, the M-NURR topology should be expected to be useful in all microwave and terahertz applications such as metamaterial absorbers [83], band-pass filters [211], band-stop filters [212], and antennas [109, 213] which are already demonstrated for the ordinary SRR and complementary SRR topologies.

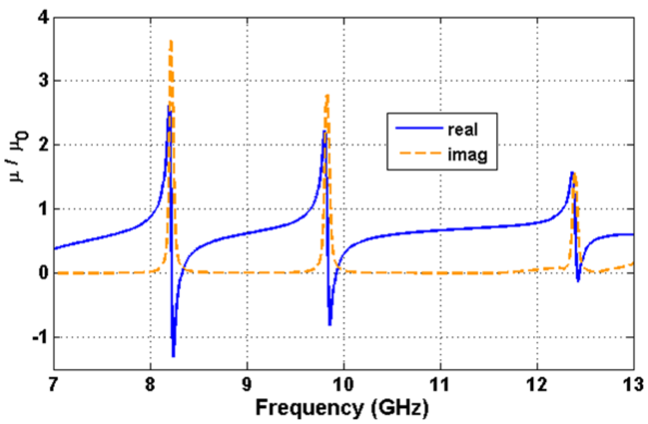

(a)

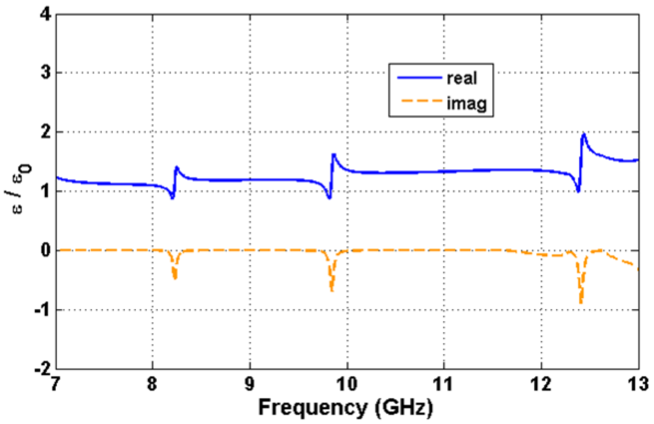

(b)

Figure 4.15: Complex effective medium parameters. (a) Relative permeability. (b) Relative permittivity.

Additional simulation results are presented in Figure 4.15 and Figure 4.16 to investigate the nature of resonances of the 3-NURR array. Real and imaginary parts of the complex valued retrieved relative permeability $\mu/\mu_0 = \mu' + j\mu''$ and relative permittivity $\varepsilon/\varepsilon_0 = \varepsilon' + j\varepsilon''$ are plotted as a function of frequency in Figure 4.15(a) and 4.15(b), respectively. Parameter retrieval approach described in [15] is used to obtain these results for exp(−jωt) time-dependence. Real part of relative permeability μ' is obtained to be negative over three distinct resonance bands around frequencies 8.24 GHz, 9.86 GHz and 12.42 GHz as seen in Figure 4.15(a) indicating the magnetic nature of the associated resonances. In the meantime, imaginary part of permeability μ'' is obtained to be positive (i.e. $\mu'' > 0$) over these resonance bands as expected for a passive medium. The slight, negligible “anti-resonance” features observed in Figure 4.15(b) in the effective permittivity curves in resonance regions may be explained by the general theory of effective media [205] as an artefact resulting from the inhomogeneous nature of this sparse 3-NURR array (see Figure 4.13(a) for the values of spatial periods). Regarding the bandwidths of resonance curves and the associated negative-permeability (MNG) regions, the 3-NURR design of this paper (see Figure 4.14(c) and Figure 4.15) and the super-cell type SRR based design reported in [35] (see Fig. 14(a) and Fig. 15 in that reference) have quite similar performances. MNG bands of both multi-band metamaterial structures are found narrow having bandwidths around 100 MHz. This comparison is particularly meaningful as the same X-band rectangular waveguide setup is used in the characterization of both metamaterial topologies leading to the same sparse array design. Use of denser metamaterial arrays is known to be helpful to increase the metamaterial bandwidth for both SRR-based and M-NURR type structures. It should also be emphasized that geometrically simpler design of the 3-NURR structure is superior to the SRR based triple-band metamaterial of reference [35] for the concerns of ease of fabrication.

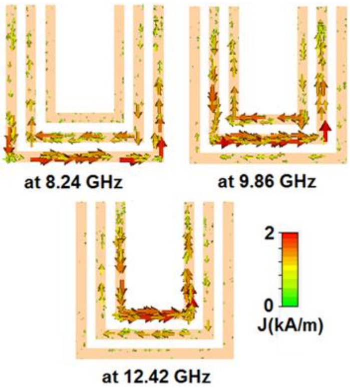

Figure 4.16: Surface current densities computed at each resonance frequency for the 3-NURR array.

As the final result of this section, Figure 4.16 demonstrates the circulating behavior of surface currents at each resonance frequency of the 3-NURR structure revealing the *LC* nature of these resonances. These current density plots also show that the resonance at f_1 = 8.24 GHz is strongly related to the current activity in the outermost U-ring while its value may be somewhat sensitive to the coupling effects caused by the presence of the middle ring. Similarly, the next resonance at f_2 = 9.86 GHz is primarily related to the currents flowing in the middle ring but also affected by the coupling effects introduced by the inner ring. The highest resonance at f_3 = 12.42 GHz is strongly associated with the innermost U-ring and it is very slightly affected by the coupling effects due to the middle ring.

4.3.2 Effects of Design Parameters on Resonance Frequencies

In this section, we will demonstrate the effects of the changing design parameters h_{1L}, h_{1R}, h_{2L}, h_{2R}, h_{3L}, h_{3R}, s_{kL}, s_{kR} and w on resonance frequencies f_1, f_2 and f_3 of the 3-NURR structure.

4.3.2.1 Effects of changing ring-to-ring separation distances on resonance frequencies

As the first parametric study, we will simulate the effects of inter-ring couplings on the values of resonance frequencies. Transmission spectra shown in Figure 4.17 are obtained for different values of s_{kL} and s_{kR} (i.e. the horizontal separation distances between the U-rings) while keeping the size of the outer ring fixed. As the value for $s_{kL} = s_{kR}$ is increased from 0.24 mm to 0.32 mm symmetrically on both left and right sides of the 3-NURR cell, capacitive coupling between neighboring rings decreases leading to lower equivalent capacitance values and hence higher resonance frequencies for the *LC* resonances, as expected. In fact, the shifts occurring in the lowest resonance frequency f_1 reflect the true inter-ring coupling effects in this parametric investigation scenario because only the outer ring does not experience any length change as $s_{kL} = s_{kR}$ varies. The base lengths of the middle and inner rings decrease as $s_{kL} = s_{kR}$ increases leading to smaller effective inductance values and hence, more pronounced increases in f_2 and especially in f_3 as observed in Figure 4.17. This parametric study is also helpful to explain the differences between the numerical and experimental values of resonance frequencies observed in Figure 4.14(b) and Figure 4.14(c) for 2-NURR and 3-NURR arrays, respectively.

Next, the ring-to-ring distance parameters are assigned asymmetrically to be $s_{kL} = 0.4$ mm between the ring arms on the left side and $s_{kR} = 0.16$ mm on the right side of the *asymmetrical 3-NURR* cell, which is shown as the inset in Figure 4.17. When we specifically choose to have $s_{kL} + s_{kR} = 2s_k = 0.56$ mm instead of having $s_{kL} = s_{kR} = s_k = 0.28$ mm, the middle and inner U-rings are simply pushed to the right without changing the overall lengths of individual U-rings. Therefore, any shifts observed in resonance frequencies would be entirely due to the induced left/right asymmetry of ring-to-ring distances. As seen in Figure 4.17, the simulated transmission spectra for these comparable symmetrical and asymmetrical 3-NURR topologies are very close to each other with negligible shifts (less than 0.7 percent) in resonance frequencies.

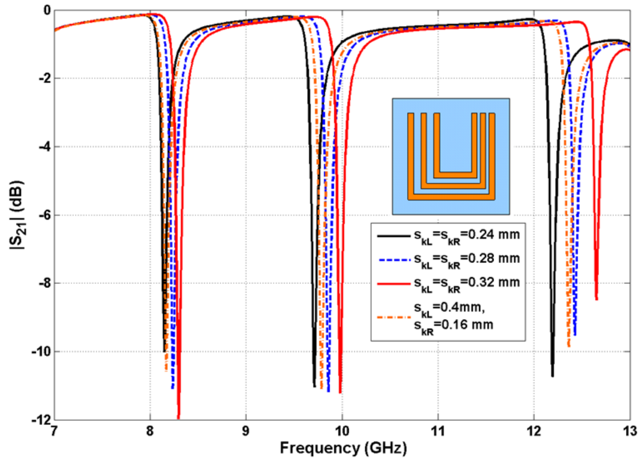

Figure 4.17: Transmission spectra of the symmetrical and asymmetrical 3-NURR topologies for different values of the ring-to-ring spacing parameter (the asymmetrical cell is shown in the inset).

4.3.2.2 Effects of changing the metal line width on resonance frequencies

Second, we have investigated the effects of changing metal strip width *w* on the resonance frequencies. The transmission spectra shown in Figure 4.18 are obtained for different values of *w* while keeping the outer boundary of the largest ring fixed. When *w* is increased from 0.24 mm to 0.32 mm, self-inductances of the U-rings decrease resulting in higher resonance frequencies as shown in the figure. More pronounced increases in f_2 and especially in f_3 are observed in Figure 4.18 because the lengths of the middle and inner rings are somewhat decreased while *w* is increased in this demonstration. This, in turn, makes equivalent inductances decrease more and hence resonance frequencies f_2 and f_3 increase more evidently.

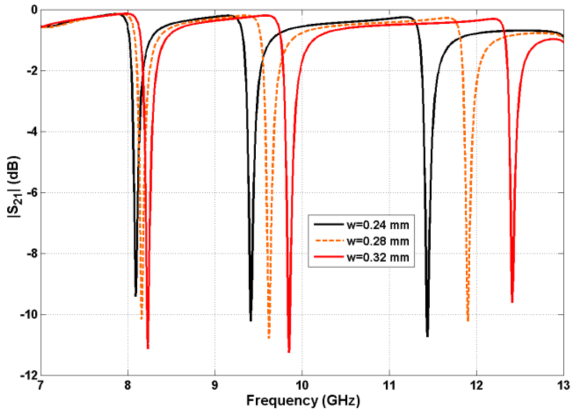

Figure 4.18 : Transmission spectra of the 3-NURR for different values of metal line width.

4.3.2.3 Effects of changing the arm lengths on resonance frequencies

In sections 4.3.2.1 and 4.3.2.2, we have shown that changing either metal strip width or separation between the neighboring metal strips causes variations in all resonance frequencies of a symmetrically designed 3-band U-ring resonator. Actually, this is a typical behavior demonstrated in numerous metamaterial papers. In this section, however, we demonstrate that an arbitrarily selected resonance frequency of this 3-NURR structure can be shifted to higher or lower frequencies by changing the arm length of the associated U-ring with negligible effects on the rest of the resonances. Because of this important property, resonances of an *M*-NURR metamaterial can be adjusted almost independently and in a highly controlled manner.

For the proof of concept, transmission spectra of 3-NURR are simulated for three different $h_{1L} = h_{1R}$ (arm lengths of the outer U-ring) values and the results are plotted in Figure 4.19(a). It is clearly seen that increasing $h_{1L} = h_{1R}$ from 4.8 mm to 5.0 mm (or to 5.2 mm) on both sides symmetrically makes the lowest resonance frequency f_1 decrease while the other two resonance frequencies are affected negligibly. Similarly, increasing $h_{2L} = h_{2R}$ (arm lengths of the middle U-ring) affects only the second resonance frequency f_2 as seen in Figure 4.19(b). Finally, increases in $h_{3L} = h_{3R}$ (arm lengths of the inner U-ring) cause reductions in the highest resonance frequency f_3 only, without affecting the other resonances, as shown in Figure 4.19(c). These results are important as they clearly show that value of each resonance frequency can be adjusted almost independently and in a highly controlled manner by changing the arm length of the associated U-ring. This behavior of the *M*-NURR topology would be impaired if the resonance frequencies are too close to each other with almost overlapping resonance curves.

Effect of asymmetry in the left/right arm lengths of the 3-NURR cell is additionally investigated in this section as follows: The asymmetrical 3-NURR cell having unequal outer arm lengths h_{1L} = 4.8 mm and h_{1R} = 5.2 mm has the same overall outer ring length as the symmetrical 3-NURR cell that has $h_{1L} = h_{1R}$ = 5.0 mm. These two length-wise equivalent topologies have almost identical transmission spectra as shown in Figure 4.19(a). Similar results are presented in the same figure for the asymmetrical cell with h_{1L} =4.8 mm and h_{1R} =5.6 mm, and its symmetrical equivalent with $h_{1L} = h_{1R}$=5.2 mm. Additional simulation results for asymmetrical 3-NURR cells with unequal left/right arm lengths in the middle and in the inner U-rings are demonstrated in Figure 4.19(b) and 4.19(c), respectively. Based on all these simulation results, it is concluded that resonance frequencies of the 3-NURR structure are negligibly affected by the left/right asymmetry as long as the individual ring lengths are kept the same.

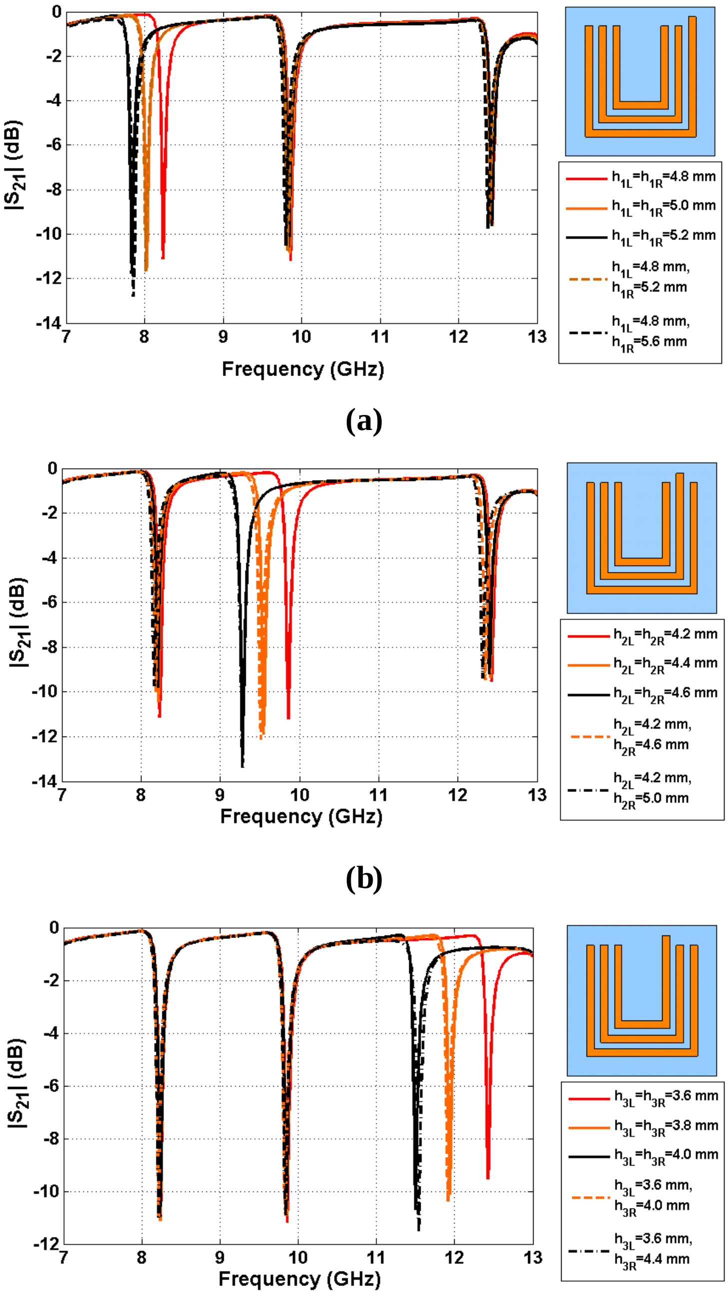

Figure 4.19: Transmission spectra of the symmetrical and asymmetrical 3-NURR topologies for different arm lengths (views of asymmetrical U-ring cells are shown as insets). **(a)** Varying h_{1L} and h_{1R} only. **(b)** Varying h_{2L} and h_{2R} only. **(c)** Varying h_{3L} and h_{3R} only.

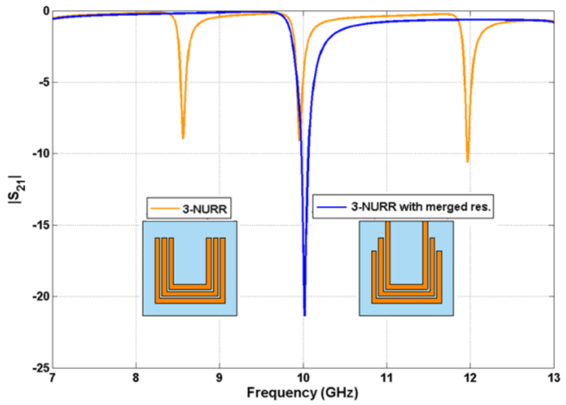

(a)

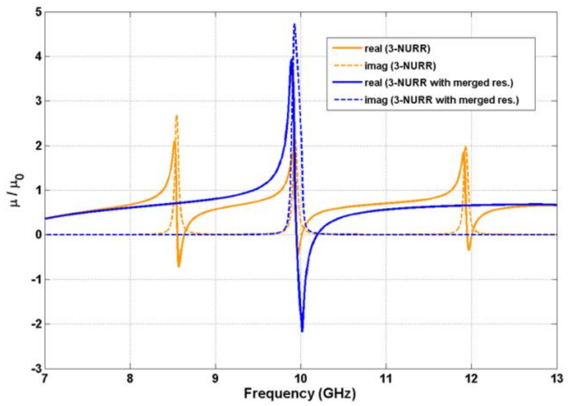

(b)

Figure 4.20: Transmission spectra and relative permeability curves for two different 3-NURR designs with distinct and merged frequencies. **(a)** Transmission spectra. **(b)** Relative permeability curves.

4.3.2.4 Merging Distinct Resonances for Improved MNG Behavior

Finally, by adjusting arm lengths of the individual U-rings, three distinct resonances of the 3-NURR structure are merged into one for the purpose of enhancing the MNG bandwidth. In this application, arm lengths of the outer, middle and inner rings of the 3-NURR cell are chosen to be $h_{1L} = h_{1R} = 4.5$ mm, $h_{2L} = h_{2R} = 4.02$ mm and $h_{3L} = h_{3R} = 3.54$ mm, respectively, to realize three distinct resonances at 8.56 GHz, 9.96 GHz and 11.97 GHz as seen in Figure 4.20(a). Then, while keeping the value $h_{2L} = h_{2R} = 4.02$ mm fixed, the arm length of the outer ring is decreased to $h_{1L} = h_{1R} = 3.58$ mm and the arm length of the inner ring is increased to $h_{3L} = h_{3R} = 4.64$ mm to merge all three resonances around 10 GHz as shown in Figure 4.20(a). In this parametric design process, the ring-to-ring separation parameters are chosen to be $s_e = s_{kL} = s_{kR} = 0.16$ mm to keep the elongated inner ring arms within the unit cell boundaries without changing the substrate dimensions. The transmission spectra for the original and tuned 3-NURR structures are plotted in Figure 4.20(a) while the corresponding retrieved relative permeability curves are shown in Figure 4.20(b). As seen in these results, the merged resonance at 10 GHz is much stronger than each of the original distinct resonances, leading to an almost three times wider MNG bandwidth with much deeper negative permeability values extending up to a level of -2.

4.4 Miniaturization of U-Shaped Multi-Band Metamaterial Structures

In this section, transmission characteristics of single-sided and double-sided (in broadside-coupled configuration) versions of M-NURR are investigated on a comparative basis for the purpose of improved miniaturization. Transmission spectra (i.e. $|S_{21}|$ versus frequency curves) of both single and double sided M-NURR topologies are computed by CST Microwave Studio for the special cases of unit cells with single ring (1-NURR) and double concentric rings (2-NURR). Exactly same physical sizes for all unit cells are used during the simulations to compute and compare their electrical sizes. Although, M-NURR topology has inherently a smaller electrical size as compared to super-cell type multi-band magnetic resonators, simulation results have revealed that broadside-coupled M-NURR topologies provide further miniaturization. In other words, broadside-coupled (BC) M-NURR has much smaller resonance frequencies (hence considerably smaller electrical sizes) as compared to their single-sided counterparts.

4.4.1 Design and Simulation Setup

The schematic top view and design parameters of the single-sided, double-ring unit cell (called 2-NURR) are shown in Figure 4.21. The corresponding broadside-coupled topology is called BC 2-NURR which has the same conducting strip pattern printed on both faces of the dielectric substrate in the anti-parallel fashion (see Figure 4.22(a).

Two more unit cell topologies (named as 1-NURR I and 1-NURR II) as well as their broadside-coupled versions (called BC 1-NURR I and BC 1-NURR II, respectively) are also shown in Figure 4.22(a). During all simulations, unit cell (UC) boundary conditions are applied at the boundary surfaces of computational volume (which is represented as the red rectangular box in Figure 4.22(b)) perpendicular to the E field and H field.

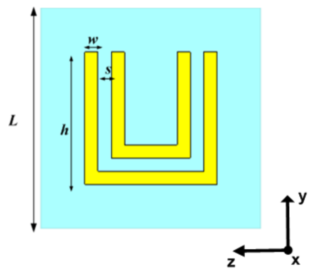

Figure 4.21: Schematic top view and design parameters of the single-sided double ring structure (called 2-NURR).

The unit cell 1-NURR I has a single U-ring which is the same as the outer (larger) ring of the unit cell 2-NURR. Similarly, the only U-ring of the unit cell 1-NURR II is the same as the inner (smaller) ring of 2-NURR. In other words, the double-band structure 2-NURR is the combination of the single-band structures 1-NURR I and 1-NURR II. The proposed *M*-NURR unit cells are designed on a planar dielectric substrate with relative permittivity ε_r = 3 and loss tangent $tan\delta$ = 0.002. Metallic inclusions are made of copper with the thickness t_{metal} = 0.035 mm and conductivity σ_{cu} = 5.8 $\times 10^7$ S/m. Dimensions of the substrate in the x, y and z directions are 2 mm, 10 mm and 10 mm respectively. The gap distance (g) and strip width (w) are both 0.6 mm.

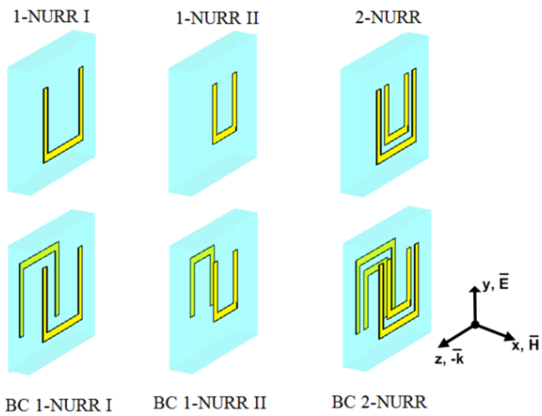

(a)

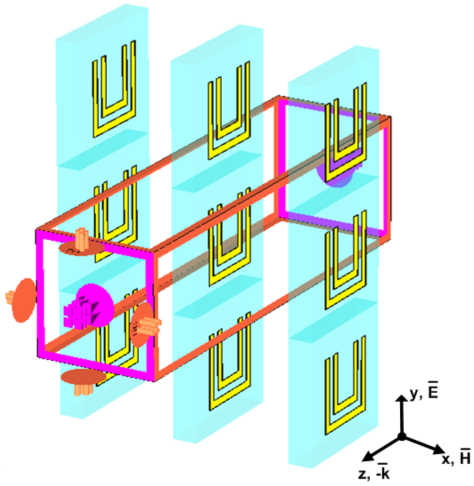

(b)

Figure 4.22: (a) Unit cell topologies of simulated M-NURRs. (b) Simulated array under UC boundary condition and field excitations in CST MWS.

4.4.2 Numerical Results

Transmission spectra for the 1-NURR I (blue curve) and BC 1-NURR I (red curve) topologies are shown in Figure 4.23 having single magnetic resonance dips at 7.42 GHz and 5.29 GHz, respectively. The electrical size (u) of a resonator structure is found by the expression $u = D/\lambda_0$ where D is the maximum linear dimension of the unit cell structure (i.e. $D = \sqrt{2}\,L$ for our square shaped unit cells with side length L) and λ_0 is the free space wavelength at resonance frequency. Therefore, the electrical sizes of the 1-NURR I and BC 1-NURR I are calculated to be 0.350 and 0.249. In other words, the double-sided BC 1-NURR I structure is electrically smaller than the single-sided 1-NURR I structure by 28.86 percent.

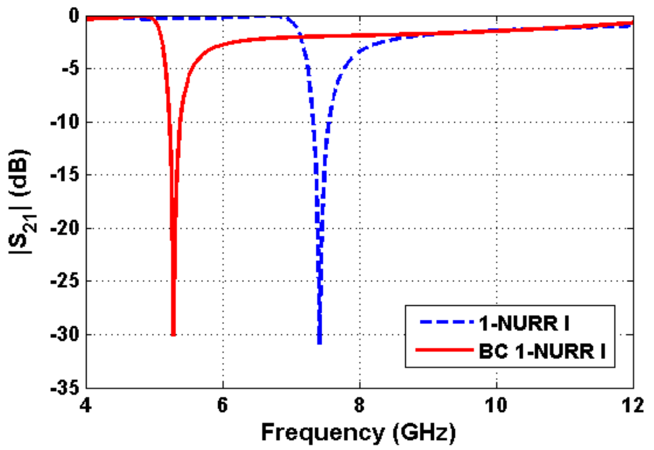

Figure 4.23: Magnitude spectra for the 1-NURR I and BC 1-NURR I arrays.

Similarly, the transmission spectra of the 1-NURR II (blue curve) and BC 1-NURR II (red curve) structures are shown in Figure 4.24 with single magnetic resonance dips at 9.54 GHz and 7.94 GHz, respectively. Accordingly, the electrical sizes of the single-sided and double-sided topologies are calculated to be 0.450 and 0.374 which means that the broadside-coupled structure is electrically smaller as compared to the 1-NURR II structure by 16.89 percent.

Finally, transmission spectra of the double-ring topologies 2-NURR (blue curve) and BC 2-NURR (red curve) are shown in Figure 4.25. As expected, each of these structures has two magnetic resonances. First resonance dips of 2-NURR and BC 2-NURR are observed at 7.06 GHz and 5.36 GHz, respectively, with the corresponding electrical sizes of 0.333 and 0.253. In other words, at the first resonance, the BC 2-NURR is electrically smaller than the 2-NURR structure by 24.02 percent. Second resonance dips of 2-NURR and BC 2-NURR are observed at 9.54 GHz and 8.51 GHz, respectively. Therefore, the electrical sizes of the 2-NURR and BC 2-NURR at their second resonances are calculated to be 0.450 and 0.401. The broadside-coupled structure is again found electrically smaller by 10.88 percent as compared to the single-sided 2-NURR structure concerning the second resonances. Computed values of resonance frequencies (f_{res}) and the corresponding electrical sizes (u) of all structures under investigation are summarized in Table 4.1.

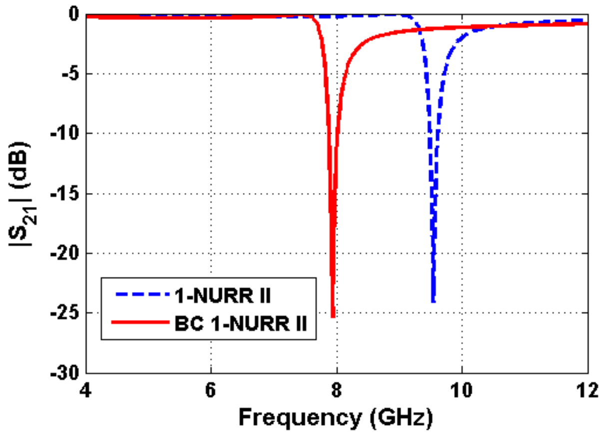

Figure 4.24: Magnitude spectra for the 1-NURR II and BC 1-NURR II arrays.

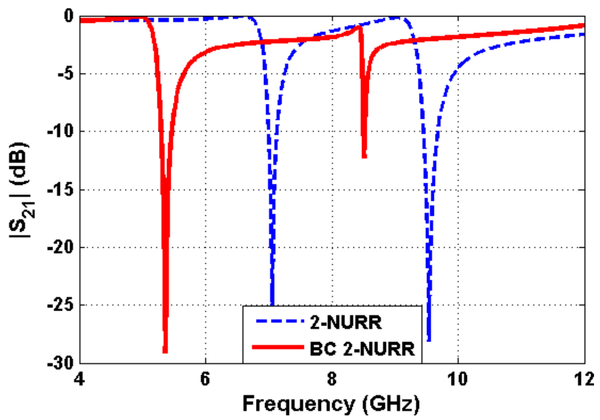

Figure 4.25: Magnitude spectra for the 2-NURR and BC 2-NURR arrays.

Table 4.1: Resonance frequencies (f_{res}) and electrical sizes (u) for the simulated M-NURR topologies.

Structure	Resonance 1		Resonance 2	
	f_{res} (GHz)	u	f_{res} (GHz)	u
1-NURR I	7.42	0.350	N/A	N/A
BC 1-NURR I	5.29	0.249	N/A	N/A
1-NURR II	9.54	0.450	N/A	N/A
BC 1-NURR II	7.94	0.374	N/A	N/A
2-NURR	7.06	0.333	9.54	0.450
BC 2-NURR	5.36	0.253	8.51	0.401

4.5 Comparison of the Nested Ring Resonators in Different Shapes as Multi-Band MNG Metamaterial

In this section, the nested ring resonators in different shapes are simulated in a comparative manner using exactly the same simulation setup and the same substrate parameters described in detail in section 4.2.1 (see Figure 4.1(b)). The same gap distance g = 0.25 mm, metal strip width w = 0.2 mm and ring-to-ring distance s=0.3 mm as well as substrate side length D =7.5 mm are used in all designs. The 3-NSRR structure given in Figure 4.3(b) is used as the initial design. The side lengths (L) of the outermost ring of the 3-NSRR is 6 mm. The diagonal length of the biggest ring of the 3-NSRR is $L_{di} = L\sqrt{2}$ as in Figure 4.26(a). Then, its modified versions are designed as presented in Figure 4.26(b-f). Thus, to be able to make a meaningful comparison, the biggest ring of the each nested ring resonator topology is printed on the area bounded by a square having side lengths L=6 mm. Thus, the diagonal length of the biggest regular hexagonal-shaped ring of the nested hexagonal-ring resonator (3-NHRR) is chosen as L as in Figure 4.26(b). L is defined as the diameter of the biggest circular-shaped ring of the nested circular-ring resonator (3-NCRR) as in Figure 4.26(c). Using the similar analogy, the side lengths (L) of the nested U-ring resonator

(3-NURR), nested triangular-ring resonator (3-NTRR) and nested V-ring resonator (3-NVRR) are presented in Figures 4.26(d-f).

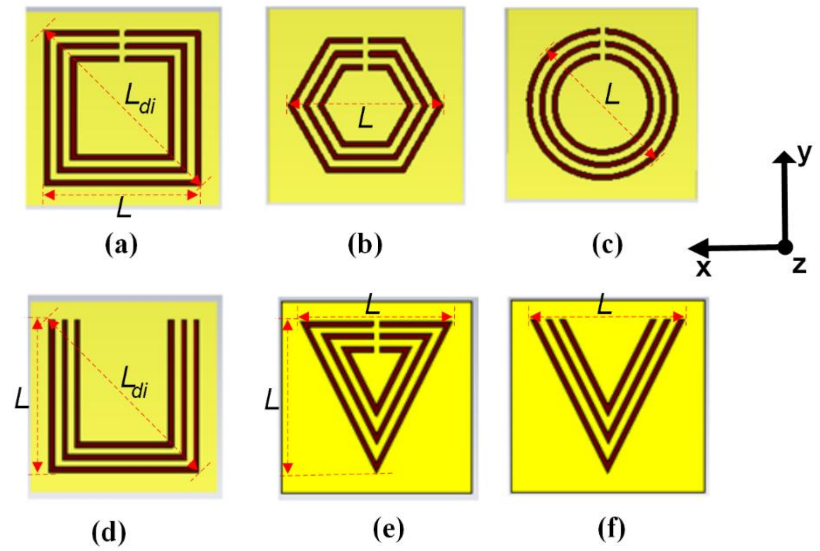

Figure 4.26: Triple-band nested ring resonators in different shapes: **(a)** 3-NSRR, **(b)** (3-NHRR), **(c)** 3-NCRR, **(d)** 3-NURR, **(e)** 3-NTRR, **(f)** 3-NVRR.

First, the transmission spectra for the 3-NSRR and 3-NURR are given in Figure 4.27. As we know, each resonance frequency of the nested ring resonators is primarily associated with the current activities in an individual ring. Its value is mainly defined the self-inductance (L_{self}) of the corresponding metallic ring and capacitance (C_{self}) between the gap of the same ring. The resulting resonance frequency can be approximately given as $\omega_0 = 2\pi f_0 = (L_{self}\, C_{self})^{-1/2}$. If 3-NSRR is turned into the 3-NURR while keeping the design parameters w and s both L_{self} and C_{gap} of each ring will become smaller. Since, L_{self} of a metallic ring is directly proportional to its total length (i.e. the perimeter of the ring), the square-shaped ring having a bigger perimeter leads to a higher L_{self} as presented in Table 4.2. In the meantime, large g will cause a smaller C_{gap}. As a result, the U-shaped ring will have a larger LC-type resonance frequency as compared to the square-shaped ring. As predicted, the 3-NSRR has lower LC resonances compared to the 3-NURR as seen in Figure 4.27. Although the 3-NSRR is electrically smaller as compared to the 3-NURR, the 3-NURR provides more simplicity in design which is a desirable asset for the design and fabrication of the new multi-band metamaterial topologies especially at THz frequencies.

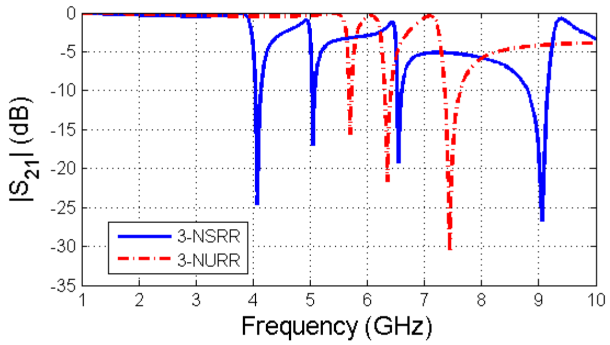

Figure 4.27: Magnitude spectra for the 3-NSRR and 3-NURR.

Then, as the modified versions of 3-NSRR topology, 3-NHRR [214] and 3-NCRR structures are simulated and compared to the 3-NSRR. The transmission spectra for these resonators are given in Figure 4.28. As expected, the 3-NSRR has lower resonance frequencies compared to the 3-NHRR and 3-NCRR since each square-shaped ring has the higher L_{self} compared to the regular hexagonal- and circular-shaped counterparts.

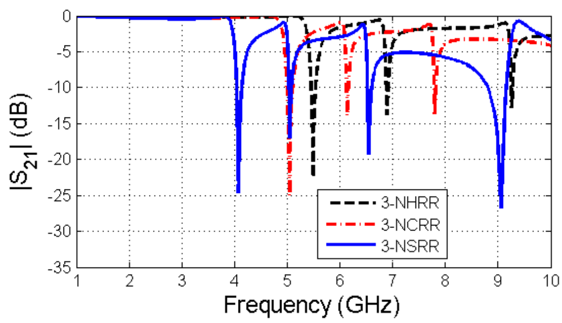

Figure 4.28: Magnitude spectra for the 3-NSRR, 3-NHRR and 3-NCRR.

Finally, the other possible modifications to the 3-NSRR topology are 3-NTRR [215] and 3-NVRR [48] structures which are simulated and compared to the 3-NSRR in the similar way. The transmission spectra for these resonators are shown in Figure 4.29. As expected, the 3-NSRR has lower resonance frequencies compared to the 3-NTRR and 3-NVRR since each square-ring have the higher L_{self} compared to the isosceles triangle- and V-shaped counterparts. It should be mentioned that the third LC resonances of 3-NTRR and 3-NVRR structures develop beyond 10 GHz due to small L_{self} and C_{gap} values of the isosceles triangular-shaped ring and V-shaped ring.

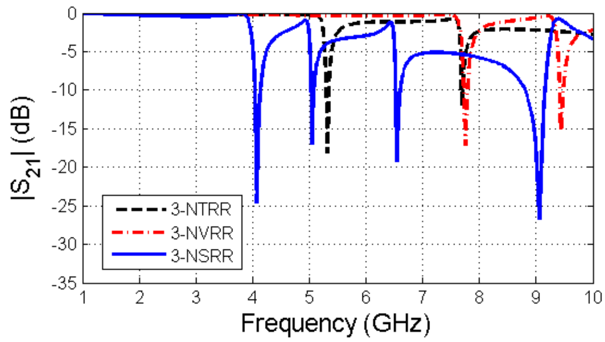

Figure 4.29: Magnitude spectra for the 3-NSRR, 3-NTRR and 3-NVRR.

Perimeter length (*P*) for the outer ring (neglecting narrow gap widths), lowest resonance frequencies (f_{res1}) and computed electrical sizes (u) at f_{res1} of all triple-band nested ring resonators under investigation are summarized in Table 4.2. The electrical size (u) of a resonator structure is found by the expression $u = D_{max} / \lambda_0$ where D_{max} is the maximum linear dimension of the unit cell structure (i.e. $D_{max} = \sqrt{2}D$ for our square shaped unit cells with side length D) and λ_0 is the free space wavelength at f_{res1}.

Table 4.2: Perimeter length (*P*) for the outer ring (neglecting narrow gap widths), lowest resonance frequencies (f_{res1}) and electrical sizes (u) for the triple-band nested ring resonators under investigation.

Topology	3-NSRR	3-NURR	3-NCRR	3-NHRR	3-NTRR	3-NVRR
P (mm)	$4L$	$3L$	πL	$3L$	$(1+\sqrt{5})$L=3.24L	$\sqrt{5}$L=2.24L
f_{res1} (GHz)	4.10	5.70	5.04	5.50	5.32	7.75
u	0.103	0.143	0.126	0.138	0.133	0.194

In summary, as seen in the Table 4.2, NSRR has the largest ring length and hence the largest self inductance L_{self} for each ring. Besides, it has a large C_{gap} due to small gap width "*g*". Therefore, it has the smallest resonance frequency and hence it is decided to be the electrically smallest topology among all six alternatives. Although NSRR has electrically smallest topology, the 3-NURR and 3-NVRR both have a simplified geometry, which is a desirable value for the design and fabrication of the new multi-band metamaterial topologies especially at THz frequencies. Besides simple in its design, the 3-NURR provides additional merit of having electrically smaller geometry compared to the 3-NVRR. As a result, it is shown that the alternative topologies such as NHRR, NCRR and NTRR have no superiorities over the NSRR topology in terms of miniaturization. Also, among the similar topologies, NVRR has no superiorities over the NURR topology in terms of miniaturization and design simplicity.

CHAPTER 5

SINGLE-, DUAL- AND TRIPLE-BAND METAMATERIAL-INSPIRED ELECTRICALLY SMALL ANTENNAS

In this chapter, metamaterial-inspired electrically small, single-, dual- and triple-band antennas with steerable radiation patterns and high radiation efficiencies at the GSM (1.93-1.99GHz), ISM (2.43-2.4835GHz), and WIMAX (3.3-3.6GHz) frequencies are introduced. Firstly, performance characteristics of these single-band and multi-band antennas are investigated numerically. Then, three different single-band antennas having their maximum directivities in the vertical, diagonal and horizontal directions at the GSM (1.93-1.99GHz) frequencies are fabricated as the exemplars of the antennas with steerable radiation patterns and experimental results from these antennas are reported. Finally, experimental results for fabricated dual- and triple-band antennas having their maximum directivities in the vertical directions are demonstrated as examples to multi-band metamaterial antenna applications. This chapter is mainly constructed by combining our results which have been already published in [115, 190] as the outcomes of this thesis research.

5.1 Introduction

The interest in and demand for wireless and mobile platforms has grown dramatically. Applications include bio-sensors, RFID tags, radars, health and crop monitoring, and communication systems. Consequently, the need and desire for multi-functional, electrically small antennas (ESAs) have also blossomed, and research in this area has flourished.

Metamaterials are artificial materials that can be designed to exhibit unusual electromagnetic properties, such as simultaneous negative permittivity and permeability [216]. These unusual properties have been shown to provide unconventional paths to novel and improved antennas with interesting and desirable performance characteristics [112, 114]. Different classes of metamaterial-inspired antennas, which are electrically small, efficient and matched intrinsically to the source, have been designed to have multi-functional properties, e.g., multi-band and circular polarization, using near-field resonant parasitic (NFRP) elements [111]. These include the introduction of capacitively loaded loop (CLL) elements as the NFRP elements [104, 106-109, 111-112] and as local resonators to achieve notched filters in an UWB antenna [110, 113, 217]. Furthermore, a related metamaterial topology with an electrically small and geometrically simple unit cell, which consists of multiple nested U-Rings to achieve multi-frequency operation, was proposed in previous studies [49].

Several single-, dual- and triple-band antennas based on NFRP elements composed of these metamaterial-inspired CLL elements are proposed and, are investigated both numerically and experimentally in the following subsections. During the all numerical simulations performed in this chapter, a commercial full-wave electromagnetic solver which is the ANSYS-ANSOFT high frequency structure simulator (HFSS) is used. In contrast to many of the previous multi-band SRR based designs [108, 112, 114], these antennas are all planar and are integrated into a compact footprint. While simple in their designs, these antennas provide multi-band operation with high radiation efficiencies above 77 percent in simulations and steerable radiation patterns in an electrically small topology. Design procedures of the proposed antennas combine the feeding and excitation mechanisms employed in [111-112] with the metamaterial design concepts reported in [111-112] and [49]. All of the proposed antennas are designed in a planar configuration having a coaxially-fed printed dipole integrated with capacitively loaded loops (CLLs) acting as near-field resonant parasitic radiators. In the proposed topology, the number of operation frequencies is determined by the number of CLLs.

5.2 Single-, Dual- and Triple-Band Antennas with Vertically Directed Radiation Patterns

In this section, the design and performance characteristics of metamaterial-inspired electrically small, single-, dual- and triple-band antennas are reported with vertically directed radiation patterns at the GSM (1.93-1.99GHz), ISM (2.43-2.4835GHz), and WIMAX (3.3-3.6GHz) frequencies.

5.2.1 Design

Topologies of the proposed single-, dual- and triple-band antennas are shown in Figures. 5.1 (a)-(c), respectively. The single-band antenna shown in Figure 5.1(a) is designed to operate at GSM frequencies with one CLL element (a metallic rectangular large ring with a gap). A ground strip is printed on the front side of a rectangular piece of low loss, copper clad substrate, 0.5oz, 31 mil (0.7874 mm) thick Rogers Duroid™ 5880. A coaxial-fed monopole is printed on the back side of the substrate. The dual-band antenna topology is shown in Figure 5.1 (b). This design is an extension of the single-band antenna topology obtained by adding another substrate layer, which has a second CLL element printed on its outside surface. In the resulting three metal-two dielectric layered structure, the monopole is on the second metal layer, which is sandwiched between the dielectric substrates. This antenna is designed to operate at the GSM and ISM frequencies. Finally, the triple-band antenna shown in Figure 5.1 (c) is designed by adding a third CLL element (the smallest CLL) on the front side of the dual-band antenna, i.e., the largest and smallest CLL elements are printed on the same side of the first substrate. A perspective view of this triple-band antenna is given in Figure 5.2 (a) to provide a clearer view of the overall design. This antenna is designed to operate at the GSM, ISM and WiMAX frequencies.

The design parameters for the triple-band antenna are given in Figure 5.2 (b). The arm lengths of the CLL elements (l_{out}, l_{mid}, l_{in}) along the x direction and (h_{out}, h_{mid}, h_{in}) along the z direction together with their widths (w_{out}, w_{mid} , w_{in}); the lengths of their gaps (w_{gout}, w_{gmid} , w_{gin}); and the gap positions (p_{gout}, p_{gmid}, p_{gin}), as well as the monopole position (p_m), are defined as the antenna parameters. Also, u_{mid} and u_{in} are used to represent the vertical placement of the middle and inner rings with respect to the large, lowest frequency ring. b_{out} , b_{mid} *and* b_{in} are devoted to the vertical placement of the outer, middle and inner rings with respect to the antenna input. The symbol h_g represents the height (with respect to the coax feed line) of the ground strip. The symbols w_m and h_m represent the dimensions of the monopole along the x and z directions, respectively. The symbols l_{sub} and h_{sub} are the lengths of the substrate along the x and z directions, respectively.

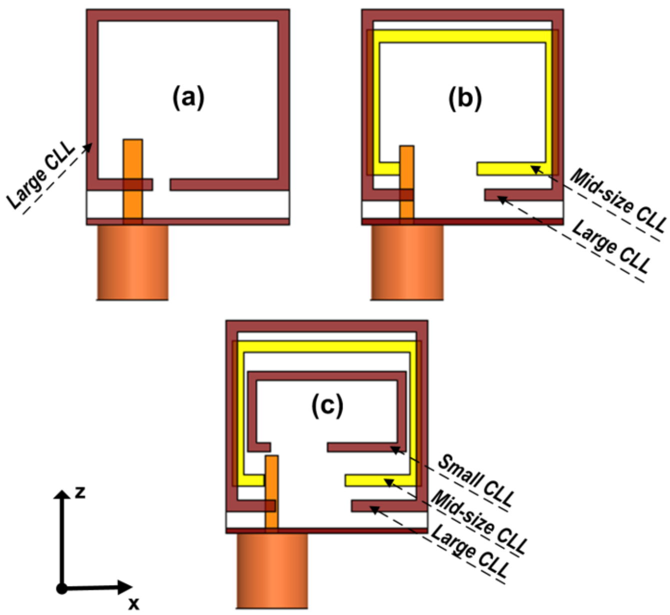

Figure 5.1: CLL-based NFRP antennas designs. (a) Single-band; (b) dual-band; and (c) triple-band.

Additional design parameters include the conductivity (σ) and thickness (t_m) of the metal parts (i.e., the brown, orange and yellow parts in the figures), as well as the relative permittivity (ε_r), thickness (t_{sub}), and loss tangent ($\tan\delta$) of the substrate (i.e., the blue rectangular part in the Figure 5.2 (a). In all of the designs, the Rogers 5880 Duroid substrate is used with parameters ε_r = 2.2, t_{sub} = 0.7874 mm, $tan\ \delta$ = 0.0009, σ

= 5.8×10 S/m, t_m = 0.017 mm (0.5 oz copper metallization), l_{sub} = 18 mm, and h_{sub} = 19 mm.

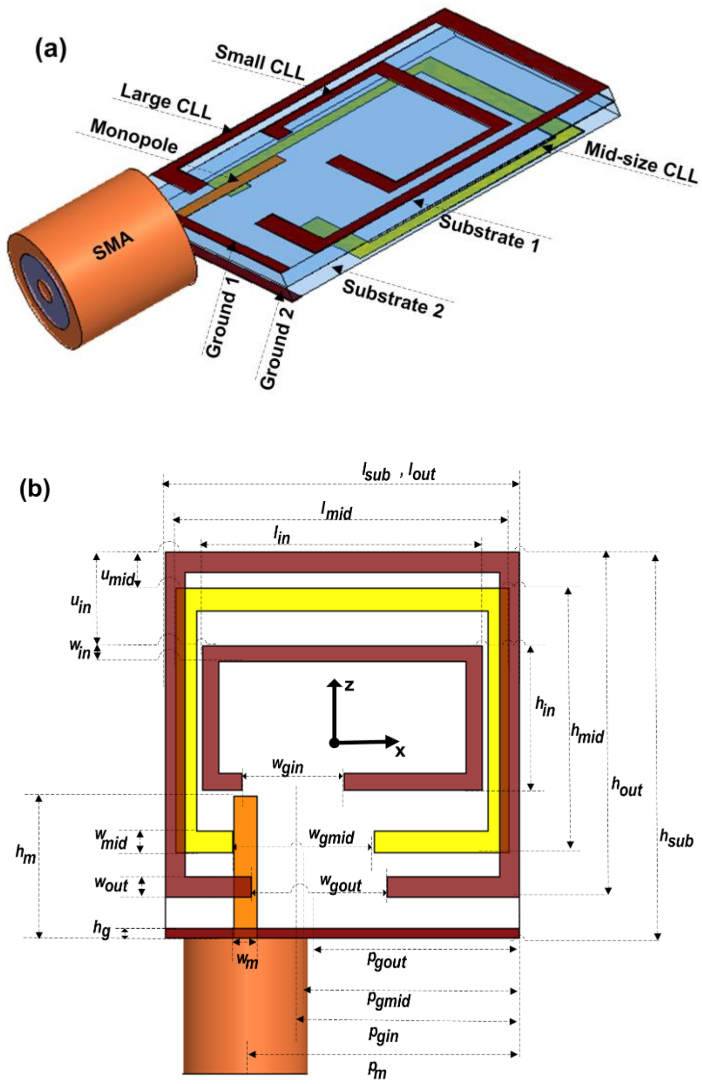

Figure 5.2: The triple-band antenna. (a) Perspective view and (b) schematic view in the xz plane.

The dimensions of the substrates were fixed for all of the designs. The design parameters are given for the proposed antennas in Table 5.1.

The coaxial feed (i.e., the cylindrical parts in the figures) was included in all of the design simulations. The diameter of the center conductor was 1.244 mm. The coax region was filled with teflon, $\varepsilon_r = 2.08$. The diameter of the teflon region was selected to be 4.16 mm to match it to the assumed 50 Ω impedance of the source. The diameter of the outer conductor wall was 6.35 mm thick.

Table 5.1: Design parameters.

Parameters (mm)	Single-band antenna	Dual-band antenna	Triple-band antenna
l_{out}	18	18	18
h_{out}	16	16.9	17
w_{gout}	1.6	6.4	6.9
w_{out}	1	1	1
p_{gout}	11.4	10.2	10.2
l_{mid}		17	17
h_{mid}		12.8	13
w_{gmid}		6.5	7.2
w_{mid}		1.1	1.1
p_{gmid}		11	11
u_{mid}		1.8	1.8
l_{in}			14.2
h_{in}			7.1
w_{gin}			5.2
w_{in}			0.8
p_{gin}			11.5
u_{in}			4.6
w_m	1.7	1.2	1.2
h_m	7.5	7	7
p_m	13.95	13.95	13.95
h_g	0.5	0.5	0.5

5.2.2 Simulation Results

We begin with an explanation of the working principles of the designed antennas using the single-band antenna and its properties as the exemplar. We will then give the simulated performance characteristics of the dual- and triple-band antennas. Nuances of each design will be highlighted.

5.2.2.1 Single-Band Antenna

As with the protractor antenna designs [111], the printed monopole is coupled to the CLL element through its electric field and excites the lowest order magnetic resonance of the CLL element leading to the circulating current on the ring as shown in Figure 5.3. The offset position of the driven monopole relative to the CLL element and its capacitive gap enables the excitation of this loop mode. The frequency of the resonance is determined primarily by the gap capacitance (C), which is determined by the trace width and the gap length, and the CLL inductance (L), which is determined by the width and length of the metallic trace. As is well-known from the original CLL studies [103], the resonance frequency is basically inversely proportional to the square root of the total LC product.

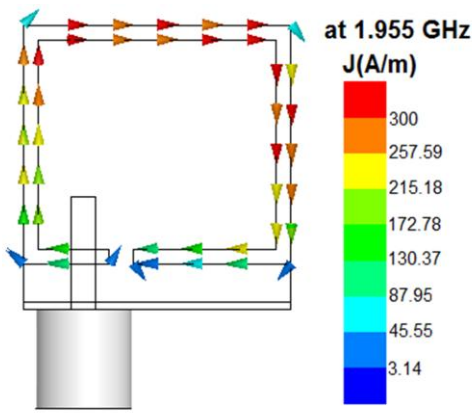

Figure 5.3: Surface current density on the CLL element of the single-band antenna at its resonance frequency.

The $|S_{11}|$ values of this single-band antenna as a function of the excitation frequency are shown in Figure 5.4. The $|S_{11}|_{min}$ value at the resonance frequency, 1.955 GHz, in the GSM frequency band is equal to -21.93 dB. Consequently, this antenna is very well matched to the assumed 50Ω source without any matching network. Because of the loop mode at resonance, it radiates as a magnetic dipole and has its maximum directivity at $\theta = 0^\circ$ as shown in Figure 5.5. Note that the placement of the gap position relative to the monopole is critical to achieve this directivity. Other gap placements allow one to adjust the maximum directivity angle of the pattern as demonstrated in [115]. The ka = 2π a / λ_{res} value, where a is the radius of the smallest sphere enclosing the entire antenna, is 0.54. Furthermore, the radiation efficiency, maximum realized gain and peak directivity of this antenna are 0.89, 1.40 and 1.57, respectively. The maximum directivity value is consistent with the antenna being electrically small and radiating as a magnetic dipole.

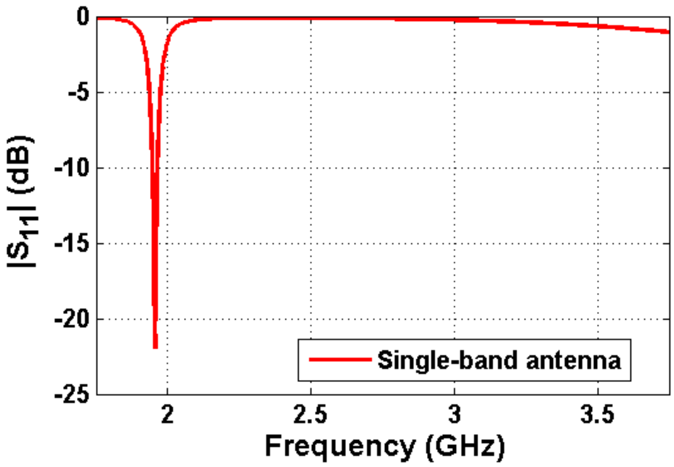

Figure 5.4: Simulated $|S_{11}|$ values (dB) versus frequency for the single-band antenna.

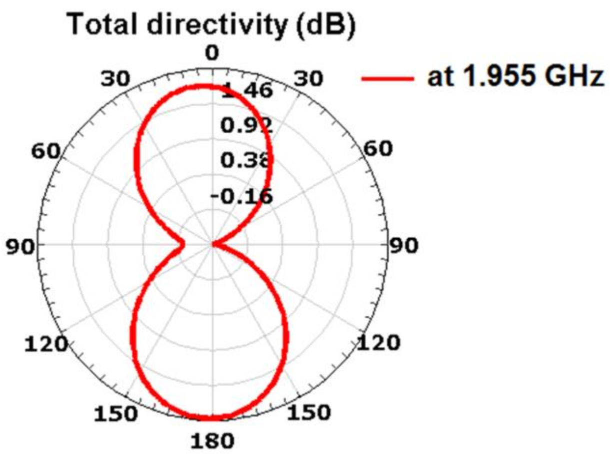

Figure 5.5: Simulated total directivity pattern (dB) of the single-band antenna in the *xz* plane at its resonance frequency.

5.2.2.2 Multi-Band Antennas

The $|S_{11}|$ values of the dual-band antenna versus frequency are shown in Figure 5.6. The total directivity patterns are shown in Figure 5.7 at its two resonance frequencies: 1.953 GHz in the GSM band and 2.454 GHz in the ISM band. Each resonance frequency is determined by the LC value defined by the dimensions of the corresponding CLL element. In other words, the resonance in the lower band is determined by the large CLL element since it has the larger inductance. The second, higher frequency resonance is determined by the LC value of the smaller, second CLL element. It should be noted that while the main impact on the resonance frequency of each CLL element is due to its individual LC value, there are coupling effects between the rings. However, it was found in this case that these coupling effects only had a very small impact on the values of the resonance frequencies.

It should also be noted that to arrive at the final dual-band design, several parametric studies were performed using single and double substrate layers with different placements of the CLLs, their gaps and the monopole. Initially, it was planned to print the two CLLs on the same side of a single substrate with the monopole on the other side. However, after several trials, we realized that using two substrates helped to minimize the coupling between the CLLs, which in turn provided higher radiation efficiencies, while providing additional flexibility for their placement. The substrate losses, which arise from the large localized fields within them, increase significantly if there is a strong coupling between the CLLs or large fields in the gap regions. For example, the choices: $u_{mid} = 0$, $b_{mid} = b_{out}$ or $l_{mid} = l_{out}$, have to be avoided since these make the coupling between the CLLs stronger. Similarly, when $b_{mid} = b_{out}$, the radiation efficiency at the first resonance decreases significantly because of the localized field around the gaps. Consequently, b_{mid} and b_{out} have different values in the design. Substrate losses are further suppressed by the obvious choice of a low loss substrate. It was determined that a dual sided version of the single-band design having two low-loss substrates with the monopole sandwiched in between them is preferred for a high radiation efficiency in the dual-band antenna design. Furthermore, this particular arrangement of the substrates and CLL elements also provided us with the ability to maintain the electrically small nature of the antenna for each of its operating bands. These dual-band design considerations encouraged us to continue using the 5 layer structure for the triple-band designs. Finally, it was found that the position of the monopole and the gap position of each CLL could be adjusted to control the directivity. For instance, if the gap position is moved toward the *+x* direction (i.e., having smaller p_{gout}, p_{gmid} and p_{gin}) for a fixed monopole position (p_m), the maximum radiation direction is tilted counterclockwise in the *xz* plane. For the cases reported herein, the position of the monopole and the gap position of each CLL were adjusted to achieve the maximum directivity around $\theta = 0^o$.

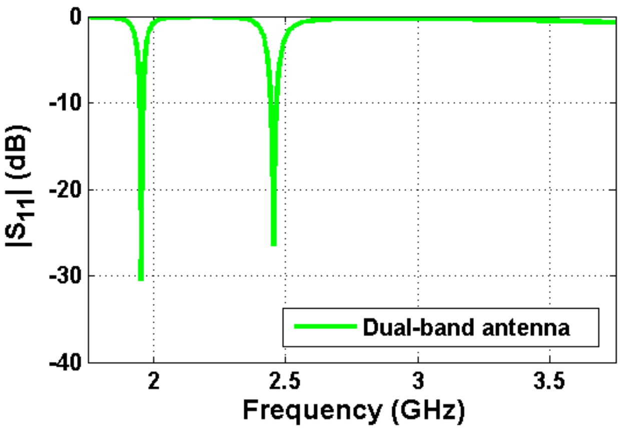

Figure 5.6: Simulated $|S_{11}|$ values (dB) of the dual-band antenna versus frequency.

The $|S_{11}|$ values and total directivity pattern for the dual-band antenna are given, respectively, in Figures 5.6 and 5.7. From Figure 5.6, $|S_{11}|_{min}$ (1.953 GHz) = -30.52 dB and $|S_{11}|_{min}$ (2.454 GHz) = -26.45 dB. One finds ka equals 0.54 at 1.953 GHz and 0.68 at 2.454 GHz. The radiation efficiency, maximum realized gain and peak directivity values of this electrically small antenna are 0.81 and 0.88; 1.29 and 1.55; 1.60 and 1.77 at its first and second resonance frequencies, respectively.

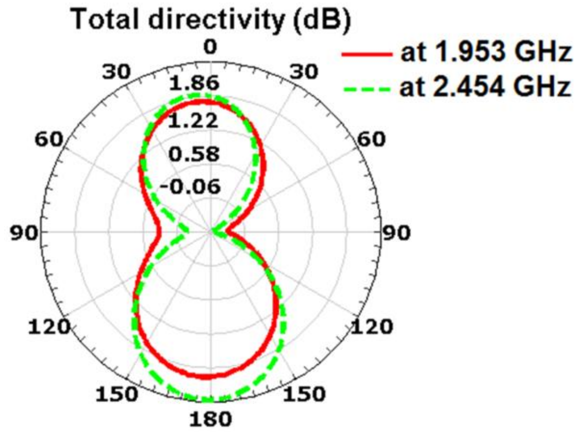

Figure 5.7: Simulated total directivity patterns (dB) of the dual-band antenna in the *xz* plane at its two distinct resonance frequencies.

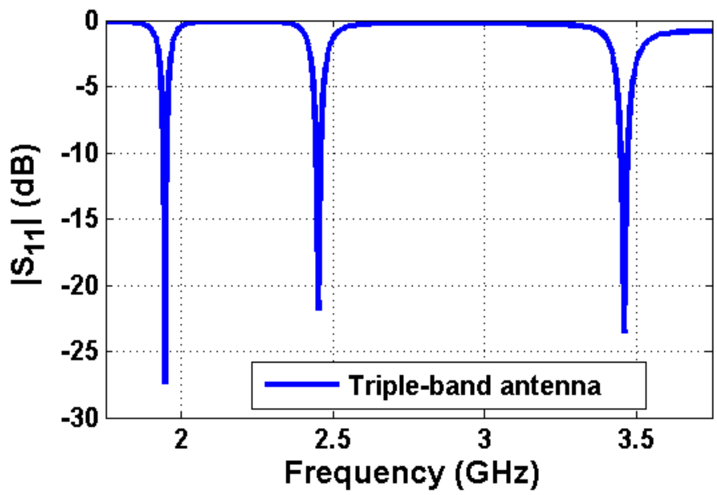

Figure 5.8 : Simulated $|S_{11}|$ values (dB) of the of the triple-band antenna in the *xz* plane versus frequency.

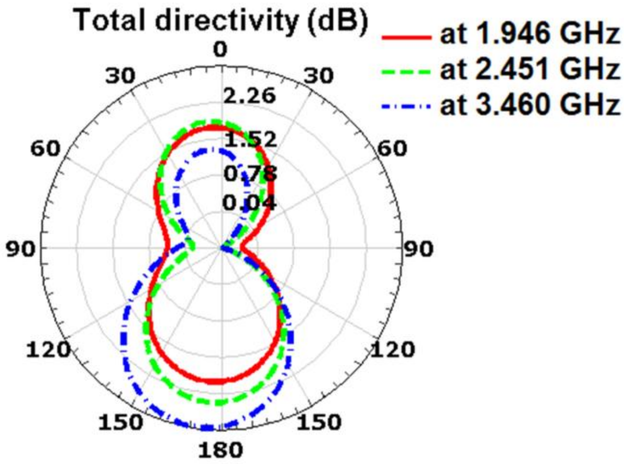

Figure 5.9: Simulated total directivity patterns (dB) of the triple-band antenna in the *xz* plane at its three resonance frequencies.

As noted, the triple-band antenna closely follows the dual-band design concepts. An additional smaller CLL element is incorporated to achieve the yet higher, third resonance. This smallest CLL element is placed on the same layer as the largest one instead of placing it in a middle layer. During the design process, this choice was found to be optimal to minimize the undesired couplings between this third CLL and the other elements i.e., the monopole, large CLL and medium size CLL. This choice also averted a space constraint and consequent coupling problem that occurs when the mid-size and small-size CLLs, being of a similar overall size, are introduced on the same layer. With the smallest and largest CLL elements being on the same layer, their mutual coupling could be minimized and the softened space constraints afforded some additional flexibility in their designs. Finally, this choice also allowed l_{in} to be as large as possible, which was found to be necessary to achieve the maximum directivity along $\theta = 0^{\circ}$.

In a similar manner, the $|S_{11}|$ values and total directivity patterns of the triple-band antenna are shown in Figures 5.8 and 5.9, respectively. As shown in Figure 5.8, the triple-band antenna has resonance frequencies at 1.946 GHz in the GSM band, at 2.451 GHz in the ISM band, and at 3.460 GHz in the WiMAX band. As indicated for the dual-band antenna, the first, second, and third resonance frequencies of the triple-band antenna are associated with the large-, medium-, and small-sized CLL elements, respectively. From Figure 5.8, one finds that $|S_{11}|_{min}$ is equal to -27.47 dB, -21.84, and -23.56 dB at the first, second and third resonance frequency; with ka equals 0.54, 0.68, and 0.96, respectively. Consequently, the triple-band antenna is electrically small for all of its operational frequencies. Furthermore, the radiation efficiency, maximum realized gain and peak directivity at those frequencies are 0.80, 0.83 and 0.81; 1.27, 1.45 and 1.60; and 1.60, 1.77 and 1.99, respectively. Clearly, the maximum directivity is increasing for a fixed overall size as the resonance wavelength decreases.

Till this point in section 5.2, metamaterial-inspired electrically small, single-, dual- and triple-band antennas having radiation patterns in the vertical direction and high radiation efficiencies at the GSM (1.93-1.99GHz), ISM (2.43-2.4835GHz), and WIMAX (3.3-3.6GHz) frequencies are designed and investigated numerically in detail. In order to show the capability of steering the maximum directivity angle of the antenna patterns, modified versions of these antennas (having the maximum directivity angle of the pattern in the diagonal and vertical directions) will be demonstrated in sections 5.3 and 5.4, respectively. It will be shown that the desired maximum directivity angle of the patterns can be achieved by adjusting the placement of the gap position relative to the monopole [115].

5.3 Single-, Dual- and Triple-Band Antennas with Diagonally Directed Radiation Pattern

In this section, the single-, dual- and triple-band antennas having their maximum directivities in the diagonal directions at the GSM (1.93-1.99GHz), ISM (2.43-2.4835GHz), and WIMAX (3.3-3.6GHz) frequencies are introduced.

5.3.1 Design

The antenna topologies shown in Figure 5.1 are modified to obtain the radiation pattern in the xz plane directed toward the diagonal ($\theta = 45°$) instead of the vertical ($\theta = 0°$) direction. The same design procedures given in section 5.2.1 are followed to design these modified antennas. The same substrate and coax feed are used for all of the designs. At the light of the explanations given in section 5.2.2.2, several parametric studies are performed using different relative placements of the monopole and the gaps of CLLs. The proper gap positions (p_{gout}, p_{gmid}, p_{gin}) and the monopole position (p_m) are adjusted to achieve maximum directivity around θ = 45º by modifying the initial antenna designs which have their maximum directivities around θ = 0º (see Figure 5.1). The gap positions of the antennas in these initial designs are moved toward the +*x* direction (i.e., having smaller p_{gout}, p_{gmid}, and p_{gin}) for a fixed monopole position (p_m) to result in new antenna designs having their maximum directivities around θ = 45º, as presented in Figure 5.10. Then other design parameters are also tuned to fix resonance frequencies and to obtain good matching with high radiation efficiencies. The resulting antenna design parameters are given in Table 5.2.

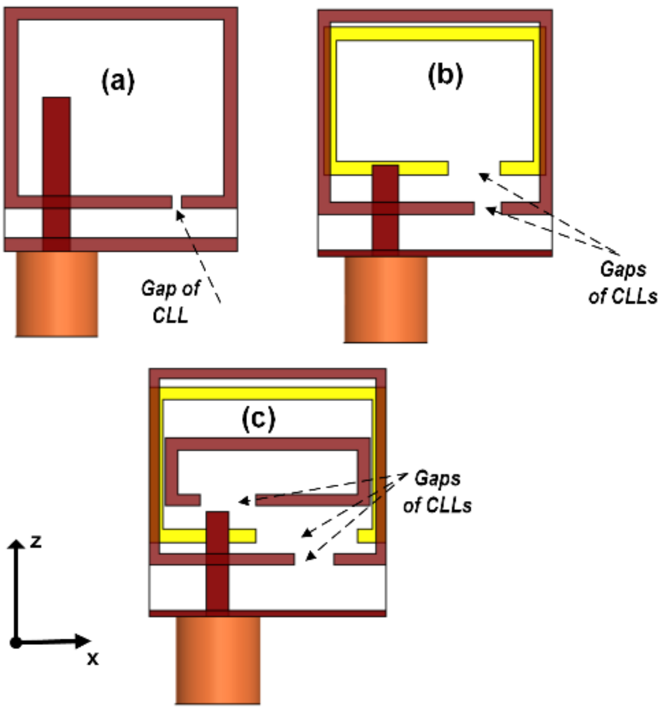

Figure 5.10: CLL-based NFRP antennas designs with diagonally directed (θ = 45º) radiation patterns. (a) Single-band, (b) dual-band, and (c) triple-band.

Table 5.2: Design parameters for the antennas (shown in Figure 5.10) having diagonally directed radiation pattern.

Parameters (mm)	Single-band antenna	Dual-band antenna	Triple-band antenna
l_{out}	18	18	18
h_{out}	15.7	15.8	15
w_{gout}	0.8	2.1	3
w_{out}	1	1	0.8
p_{gout}	4.7	5	5.5
l_{mid}		17	18
h_{mid}		11.3	11.9
w_{gmid}		4	7.7
w_{mid}		1	1
p_{gmid}		6	6
u_{mid}		1.4	1.4
l_{in}			15.5
h_{in}			5.2
w_{gin}			4.2
w_{in}			0.9
p_{gin}			12
u_{in}			5.3
w_m	2.2	2	1.7
h_m	12	7	8
p_m	14	12.8	12.8
h_g	1	0.5	0.5

5.3.2 Simulation Results

The simulated performance characteristics of the single-, dual- and triple-band antennas having their maximum directivities around $\theta = 45^{o}$ are given in this section.

5.3.2.1 Single-Band Antenna

In this section, the simulated performance characteristics of the single-band antenna operating at GSM frequency band (see the Figure 5.10 (a)) are presented. The $|S_{11}|$ values of this antenna as a function of the excitation frequency are shown in Figure 5.11. The $|S_{11}|$ displays a single resonance at 1.953 GHz in the GSM frequency band. The $|S_{11}|_{min}$ value at the resonance frequency is equal to -24.63 dB. Consequently, this antenna is very well matched to the assumed 50Ω source without any matching network. The simulated total directivity pattern (dB) of this antenna in the xz plane, at its resonance frequency, are shown in Figure 5.12. The antenna has its maximum directivity around θ = 45° as shown in Figure 5.12. The ka value is 0.53 displaying the electrically small size of the proposed antenna. Furthermore, the radiation efficiency, maximum realized gain and peak directivity of this antenna are 0.91, 1.33, and 1.46, respectively. It should be noted that, while this antenna have similar performance characteristics to the one proposed in section 5.2.2.1, there is approximately 45° shift between their maximum directivity angles.

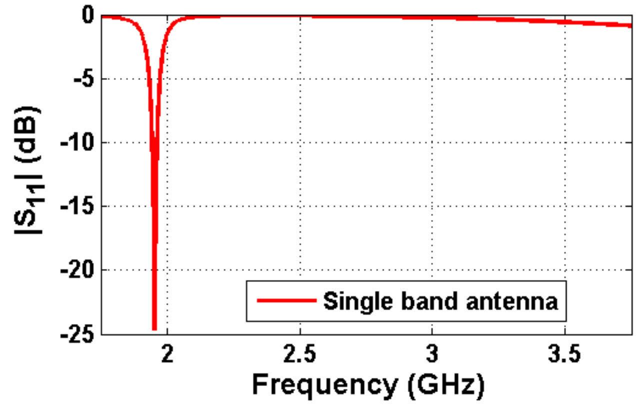

Figure 5.11: Simulated $|S_{11}|$ values (dB) versus frequency of the single-band antenna.

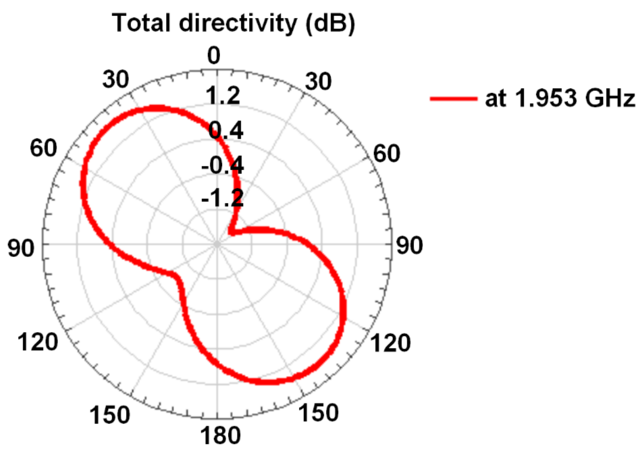

Figure 5.12: Simulated total directivity pattern (dB) of the single-band antenna in the *xz* plane at its resonance frequency.

5.3.2.2 Multi-Band Antennas

In this section, the simulated performance characteristics of the dual-band antenna (see Figure 5.10 (b)) and triple-band antenna (see Figure 5.10 (c)) are presented.

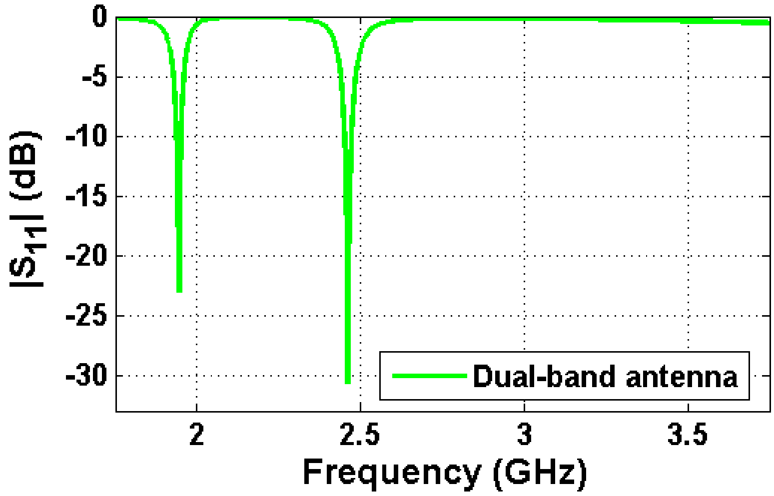

Figure 5.13: Simulated $|S_{11}|$ values (dB) for the dual-band antenna versus frequency.

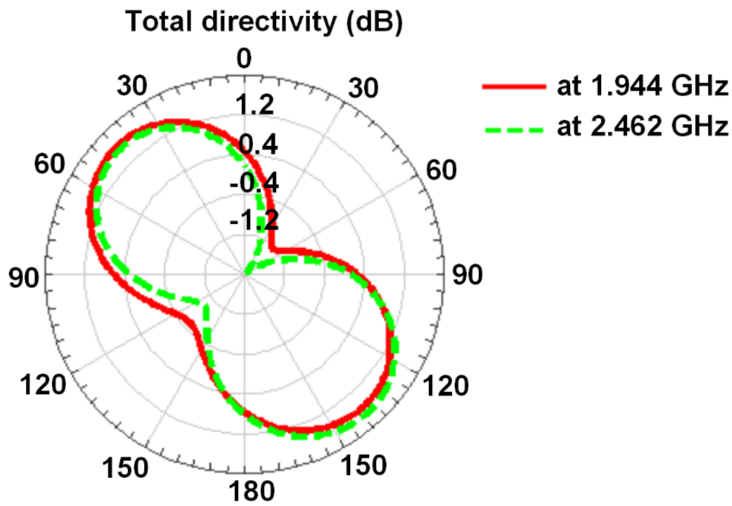

Figure 5.14: Simulated total directivity patterns (dB) of the dual-band antenna in the *xz* plane at its two resonance frequencies.

Figure 5.13 represents the $|S_{11}|$ values of the dual-band antenna versus frequency. The $|S_{11}|$ displays two resonance frequencies: 1.944 GHz in the GSM band and 2.462 GHz in the ISM band. The $|S_{11}|_{min}$ values are equal to -23.03 dB and -30.69 dB at the first and second resonance frequencies, respectively. The total directivity patterns are shown in Figure 5.14, revealing the maximum directivities around θ = 45º at both resonance frequencies. The ka values are equal to 0.53 at 1.944 GHz and 0.68 at 2.462 GHz. The radiation efficiency, maximum realized gain and peak directivity values of this electrically small antenna are 0.86 and 0.86; 1.25 and 1.28; 1.45 and 1.45 at its first and second resonance frequencies, respectively. It should be noted that while this dual-band antenna have similar performance characteristics to the one proposed in section 5.2.2.2, there is approximately 45º shift between their maximum directivity angles.

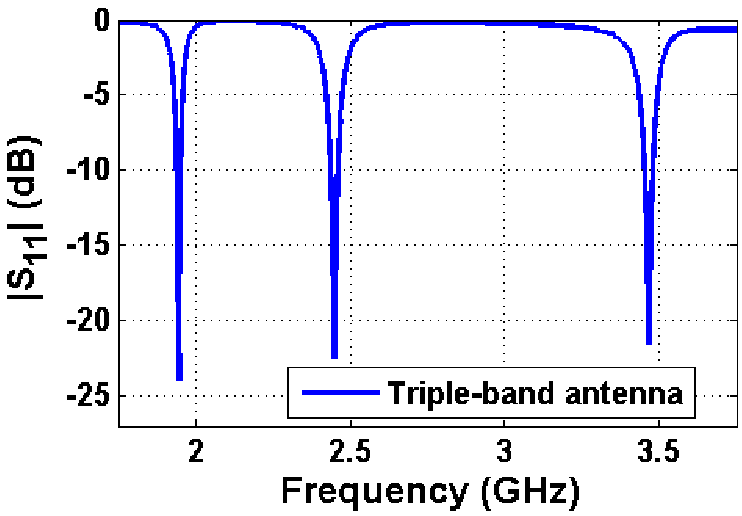

Figure 5.15: Simulated $|S_{11}|$ values (dB) for the triple-band antenna in the *xz* plane versus frequency.

In a similar manner, the $|S_{11}|$ values and total directivity patterns of the triple-band antenna are shown in Figures 5.15 and 5.16, respectively. As shown in Figure 5.15, the triple-band antenna has resonance frequencies at 1.945 GHz in the GSM band, at 2.448 GHz in the ISM band, and at 3.466 GHz in the WiMAX band. From Figure 5.15, one finds that $|S_{11}|_{min}$ is equal to -23.95 dB, -22.43, and -21.51 dB at the first, second and third resonance frequencies; and, ka equals 0.53, 0.67, and 0.95, respectively. Consequently, the triple-band antenna is electrically small at all of its operational frequencies. Furthermore, the radiation efficiency, maximum realized gain and peak directivity at those frequencies are 0.80, 0.86 and 0.87; 1.16, 1.25 and 1.24; and 1.46, 1.47 and 1.44, respectively. It should be noted that triple-band antenna proposed in section 5.2.2.2 and the modified antenna proposed in this section have similar antenna performances. However, while the former one has its maximum directivity angles around θ = 0º, the latter one has its maximum directivity angles around θ = 45º.

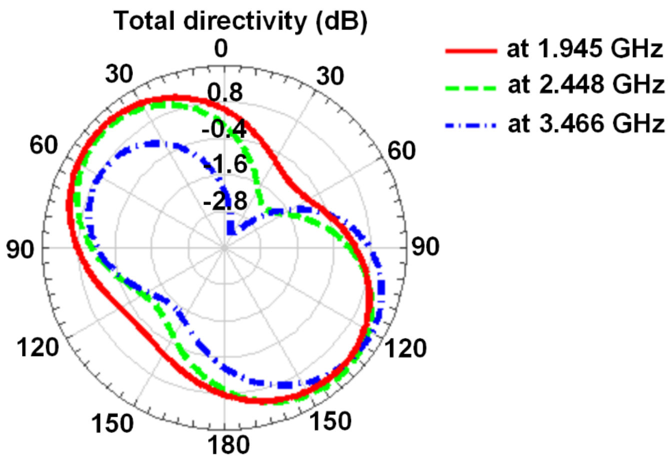

Figure 5.16: Simulated total directivity patterns (dB) of the triple-band antenna in the *xz* plane at its three distinct resonance frequencies.

5.4 Single- and Dual-Band Antennas with Horizontally Directed Radiation Patterns

In this section, the design and performance characteristics of metamaterial-inspired electrically small, single- and dual-band antennas with horizontally directed radiation pattern at the GSM (1.93-1.99GHz) and ISM (2.43-2.4835GHz) frequencies are reported.

5.4.1 Design

The single- and dual-band antennas presented in this section are designed to oporate at the GSM (1.93-1.99GHz) and ISM (2.43-2.4835GHz) frequencies by using similar design procedures outlined in Section 5.2.1 and Section 5.3.1. Antenna topologies shown in Figure 5.17 are optimized to have their maximum radiation along the horizontal (θ= 90º) direction. The gaps are placed on the vertical right arm of the antennas to obtain the maximum directivity at θ = 90º. The imaginary part of the antenna input impedance becomes highly capacitive by this special placement of the gaps. By printing an additional strip having strip width w_{in} =2mm for the single-band antenna (see the Figure 5.17 (a)) and for the dual-band antenna (see Figure 5.17 (b)) behind the gap of the larger CLL, the highly capacitive imaginary parts of the input impedances are compensated to obtain good matching. Then, other parameters are adjusted to fix resonance frequencies and to obtain good matching while keeping the radiation efficiencies as high as possible. The design parameters are listed for the resulting antenna designs in Table 5.3.

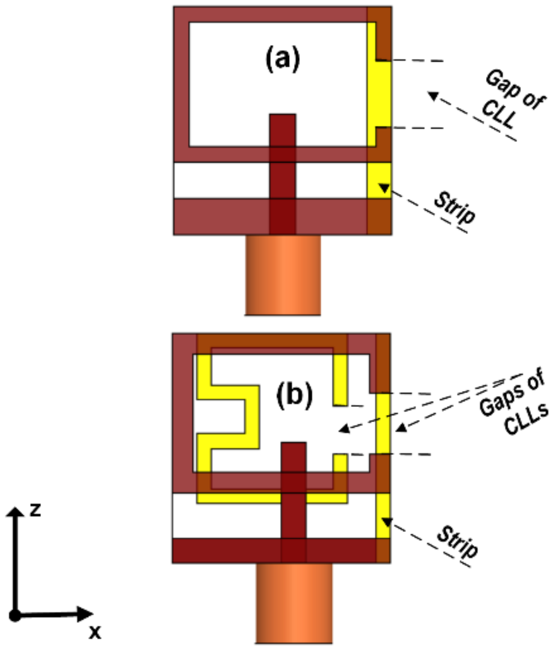

Figure 5.17 : CLL-based NFRP antennas designs with horizontally directed radiation pattern. (a) Single-band and (b) dual-band.

Table 5.3: Design parameters for the antennas (shown in Figure 5.17) having horizontally directed radiation pattern.

Parameters (mm)	Single-band antenna	Dual-band antenna
l_{out}	18	18
h_{out}	13	13.2
w_{gout}	5.5	5
w_{out}	1.3	1.7
l_{mid}		12.5
h_{mid}		14.05
w_{gmid}		4
w_{mid}		1.2
u_{mid}		0
w_m	2.2	2
h_m	10	10
p_m	9	8
h_g	3	2

5.4.2 Simulation Results

The simulated performance characteristics of the single- and dual-band antennas having their maximum directivities around θ = 90º are given in this section.

5.4.2.1 Single-Band Antenna

In this section, the simulated performance characteristics of the single-band antenna operating at GSM frequency band (see the Figure 5.17 (a)) are presented. The $|S_{11}|$ values of this antenna as a function of the excitation frequency are shown in Figure 5.18. The $|S_{11}|$ displays one resonance at 1.951 GHz in the GSM frequency band. The $|S_{11}|_{min}$ value at the resonance frequency is equal to -21.91 dB. Consequently, this antenna is very well matched to the assumed 50Ω source without any matching network. The simulated total directivity pattern (dB) of this antenna are shown in Figure 5.19 in the xz plane at its resonance frequency. The antenna has its maximum directivity around θ = 90º as shown in Figure 5.19. The ka is 0.54 displaying the electrically small topology of the proposed antenna. Furthermore, the radiation efficiency, maximum realized gain and peak directivity of this antenna are 0.82, 1.30 and 1.58, respectively.

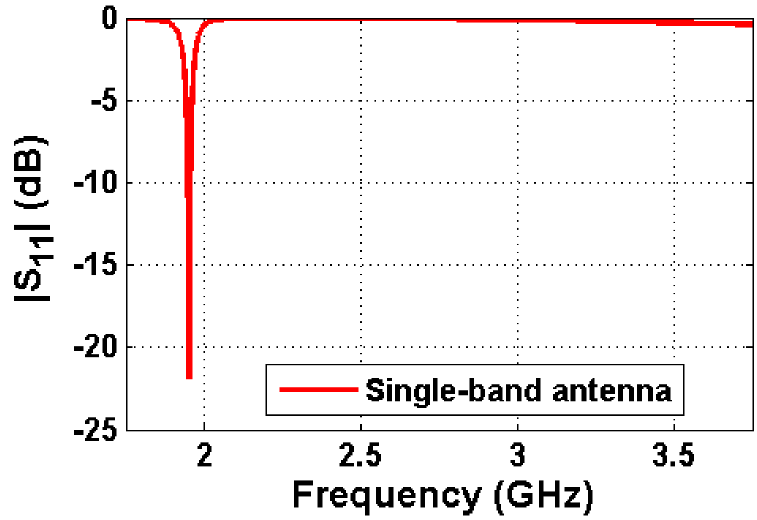

Figure 5.18: Simulated $|S_{11}|$ values (dB) versus frequency for the single-band antenna.

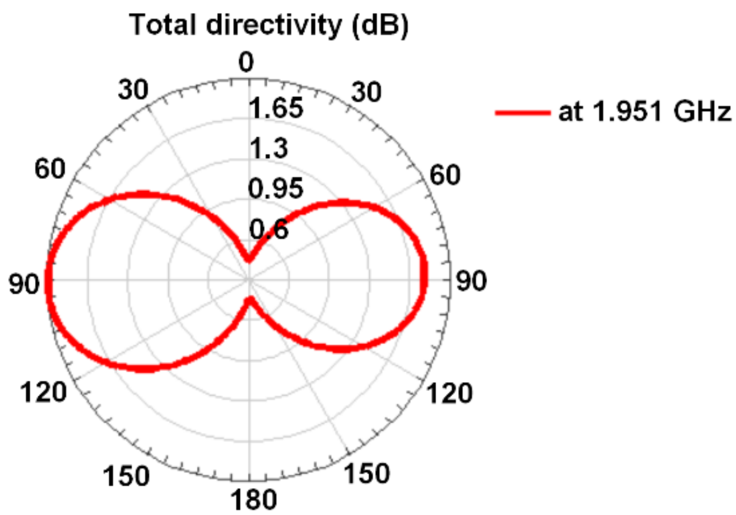

Figure 5.19: Simulated total directivity pattern (dB) of the single-band antenna in the *xz* plane at its resonance frequency.

It should be noted that, when the additional strip is placed behind the gap of the larger CLL, the first resonance frequency which is mainly defined by the larger CLL shifted to lower frequencies due to the increased capacitive coupling effects between the larger CLL and the strip. Since the resonance frequency is basically inversely proportional to the square root of the total LC (inductance and capacitance) product, smaller h_{out} (hence the smaller inductance) and larger w_{gout} (hence smaller capacitance) is needed to obtain the resonance frequency in the GSM band compared to the h_{out} and w_{gout} values of the single-band antennas having their maximum directivities around θ = 0º and θ = 45º.

It should also be noted that this antenna has relatively small radiation efficiency (equal to 0.82) compared to the radiation efficiencies of its counterparts having maximum directivity around θ = 0º (equal to 0.89) and having maximum directivity around θ = 45º (equal to 0.91). This relatively smaller radiation efficiency can be explained by the increased coupling effects between the CLL and the strip.

5.4.2.2 Dual-Band Antenna

In this section, the simulated performance characteristics of the dual-band antenna (see Figure 5.17 (b)) are presented.

Figure 5.20 represents the $|S_{11}|$ values of the dual-band antenna versus frequency. The $|S_{11}|$ displays two resonance frequencies: 1.956 GHz in the GSM band and 2.45 GHz in the ISM band. The $|S_{11}|_{min}$ values are equal to -28.71 dB and -33.41 dB at the first and second resonance frequencies, respectively. The total directivity patterns are shown in Figure 5.21 revealing the maximum directivities around θ = 90º at both resonance frequencies. The ka values are equal to 0.54 at 1.956 GHz and 0.67 at 2.45 GHz. The radiation efficiency, maximum realized gain and peak directivity values of this electrically small antenna are 0.77 and 0.81; 1.22 and 1.36; 1.59 and 1.68 at its first and second resonance frequencies, respectively.

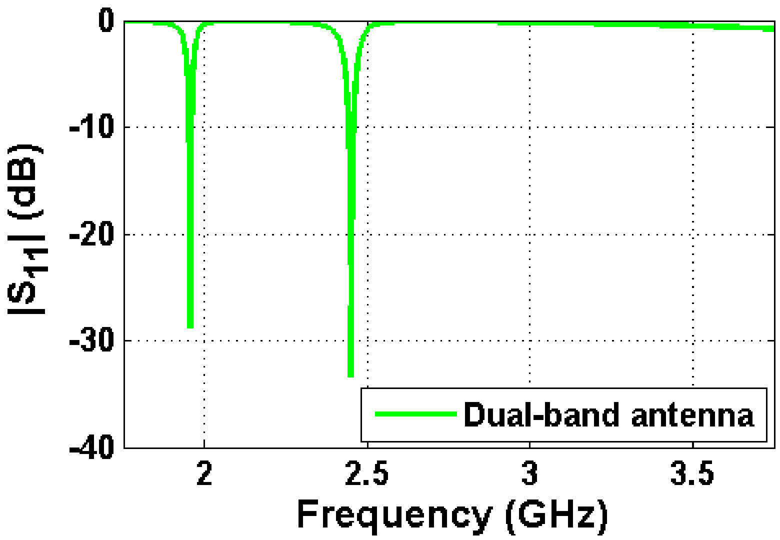

Figure 5.20: Simulated $|S_{11}|$ values (dB) for the dual-band antenna versus frequency.

It should be noted that the vertical left arm of the second CLL (i.e., the yellow CLL in the Figure 5.17 (b)) is meandered to obtain the second resonance in the ISM band. This choice makes the coupling between the CLLs as small as possible and hence the radiation efficiency as high as possible.

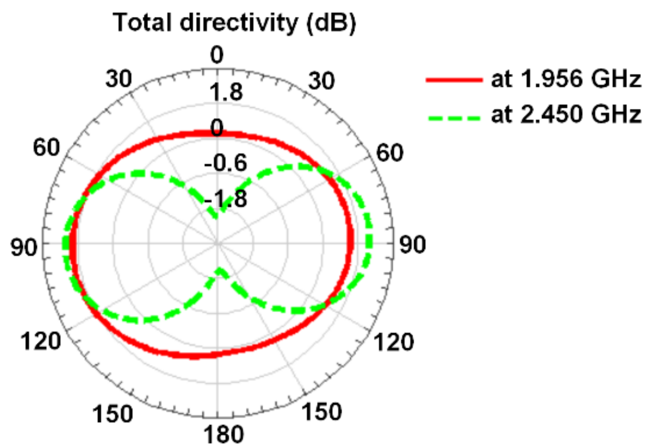

Figure 5.21: Simulated total directivity patterns (dB) of the dual-band antenna in the *xz* plane at its two distinct resonance frequencies.

It should be also noted that several parametric studies were performed to obtain a similar antenna with triple-band operation. However, the triple-band antenna could not be achieved without losing the radiation efficiency or electrically small topology. Thus, the results of the triple-band antenna is not included in this section.

In summary, the choice of a low loss substrate and the proper placements of the CLL elements relative to each other and relative to the monopole are the key points that had to be considered in the design of proposed antennas to achieve high radiation efficiencies, maximum directivity at selected directions, and small electrical size with simple geometry.

In the next section, experimental results of three different single-band antennas having their maximum directivities in the vertical, diagonal and horizontal directions as well as experimental results of dual- and triple-band antennas having their maximum directivities in the vertical direction will be demonstrated.

5.5 Experimental Results

In this section, three different single-band antennas operating at the GSM (1.93-1.99GHz) frequencies and having their maximum directivities at $\theta = 0^o$, $\theta = 45^o$ and $\theta = 90^o$ directions in the x-z plane are fabricated and measured as the exemplars of the antennas with steerable radiation patterns. Then, experimental results for fabricated dual- and triple-band antennas having their maximum directivities in the vertical directions (at $\theta = 0^o$ in the x-z plane) are demonstrated as examples to multi-band metamaterial antenna applications. All these antennas are first simulated by HFSS and then fabricated by using LPKF-ProtoMat-H100 circuit board plotter. The design parameters are summarized for all of fabricated antennas in Table 5.4. Since the surface mount SMA connector of Johnson Components (part number:142-0711-201) is inserted into the input of the antenna during the measurements, the antenna simulations given in the previous sections are repeated using this specific SMA connector. Newly simulated antenna parameters are found slightly modified as presented in Table 5.4.

(a) (b) (c)

Figure 5.22: The photographs from the antenna measurement setups: (a) Return loss (S_{11}) measurement setup, (b) the placement of the AUT and (c) the horn antenna in the anechoic chamber.

Fabrication and measurement tasks are completed using the facilities in the EEE Antenna Measurement Laboratory of METU. A photograph from the return loss (S_{11}) measurements of the proposed antennas performed by using a vector network analyzer (VNA), Agilent 8750D, is shown in Figure 5.22 (a). It is seen that, the antenna under test (AUT) is connected to the VNA input through a rigid coaxial cable with the sleeve balun. Far field measurements are performed within the anechoic chamber in the laboratory. Two photographs from the far field measurements are presented: the placement of the antenna under test (AUT) in Figure 5.22 (b) and the horn antenna in Figure 5.22 (c) in the anechoic chamber.

5.5.1 Experimental Results for Single-Band Antennas with Steerable Radiation Patterns

In this section, experimental results for three different single-band antennas having their maximum directivities in the vertical, diagonal and horizontal directions in the xz plane at the GSM (1.93-1.99GHz) frequencies will be reported. Before presenting the measurement results, a brief explanation will be given about the balun design that had to be used in our antenna measurements. When a small antenna with unbalanced feed line such as a coaxial cable is in use, the shield side of the cable radiates in addition to the antenna itself. This situation leads to lower efficiencies and also distorts the radiation pattern of the antenna asymmetrically. To present these undesired radiations caused by the surface currents flowing through the outer shield of the RF feed cable, the antenna needs to be fed by a coaxial cable having a balun. The balun helps to convert the unbalanced signal provided by the coaxial cable to a balanced symmetrical signal for the antenna.

The sleeve balun design [218-220] is found to be useful in our single-band antenna applications. Using the approach given in [221], the balun design is accomplished. The length (l_b), diameter (R_b) and thickness (w_b) of the balun, the distance between the open end of the balun and the input of the antenna (p) as well as the coaxial cable diameter (R_{coax}) are design parameters of the sleeve balun as shown in Figure 5.23. After several numerical trials, the optimal design values are found as l_b= 36mm, R_b= 12mm, w_b= 1mm, p= 17mm and R_{coax}= 4.6mm.

Three different simulations are performed to reveal the effect of the coaxial cable and the balun on the antenna performances. In the first simulation, a short coaxial cable having L_{coax} =6.69 mm is used. Then, the second simulation is performed with a long coaxial cable having L_{coax} = 57 mm. In the third simulation, a long coaxial cable having L_{coax} = 57 mm with the sleeve balun is used. Return loss values and total directivity pattern in the xz plane are presented in Figure 5.24 and 5.25 respectively**.**

As shown in Figure 5.24, the minimum return loss values are computed to be $|S_{11}|_{min}$ (1.948 GHz) = -21.98 dB, $|S_{11}|_{min}$ (1.949 GHz) = -7.12 dB and $|S_{11}|_{min}$ (1.948 GHz) = -25.53 dB for the first, second and third simulations. It is seen that while $|S_{11}|_{min}$ values of the simulations with the short coax and with the balun are very similar (smaller than -20 dB), $|S_{11}|_{min}$ value of the simulation with the long coax is much larger (around -7 dB).

Table 5.4: Design parameters for the fabricated antennas.

Parameters (mm)	Single-band	Single-band	Single-band	Dual-band	Triple-band
	antenna having its maximum directivity at				
	at θ=0⁰	at θ=45⁰	at θ=90⁰	at θ=0⁰	at θ=0⁰
l_{out}	18	18	18	18	18
h_{out}	15.9	16	12.9	17	17
w_{gout}	1.6	0.8	5.5	5.1	5.9
w_{out}	1	1.1	1.3	1	1
p_{gout}	11.4	4.7	on the vertical right arm	10.6	10.6
l_{mid}	-	-	-	17	17
h_{mid}	-	-	-	12.7	12.9
w_{gmid}	-	-	-	3.6	3.9
w_{mid}	-	-	-	1.2	1.1
p_{gmid}	-	-	-	11.1	11.6
u_{mid}	-	-	-	2.1	1.8
l_{in}	-	-	-		14.4
h_{in}	-	-	-		7.5
w_{gin}	-	-	-		5.2
w_{in}	-	-	-		0.8
p_{gin}	-	-	-		9.8
u_{in}	-	-	-		4.2
w_m	1.7	2.2	2.2	1.2	1.2
h_m	7	16	10	5.5	6
p_m	13.95	14.7	9	13.95	13.95
h_g	0.5	0.5	3	0.5	0.5

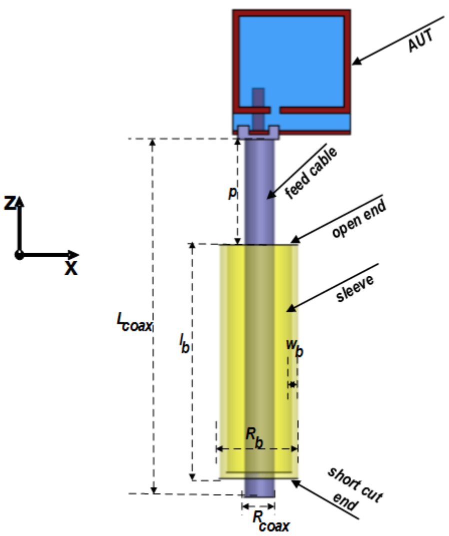

Figure 5.23: The single-band antenna having its maximum directivity in the vertical direction with a coaxial feed cable and a sleeve balun.

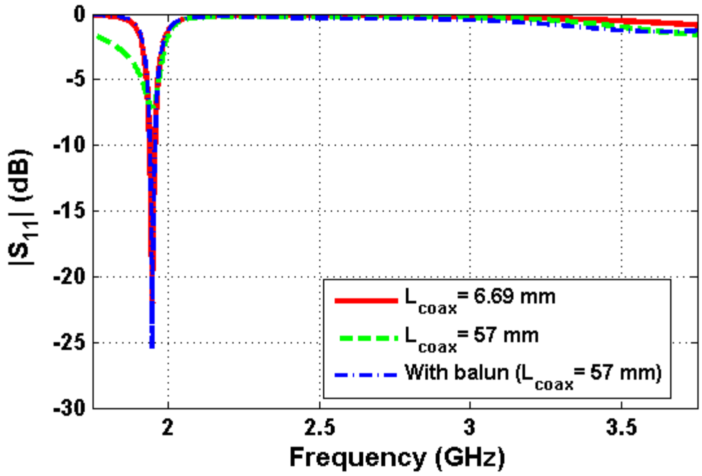

Figure 5.24: Simulated return loss ($|S_{11}|$) of the single-band antenna (having its maximum directivity in the vertical direction) for different coaxial feed conditions with and without a sleeve balun.

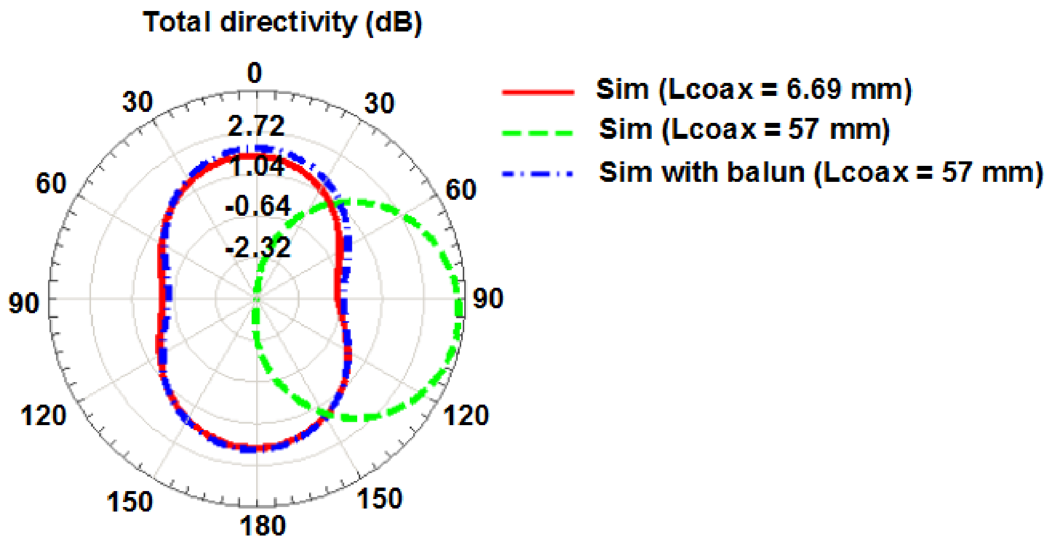

Figure 5.25: Total directivity pattern simulated for the single-band antenna (having its radiation patterns in the xz plane directed towards the vertical direction ($\theta = 0°$)) for three different coaxial feed configurations.

Similarly, as seen in Figure 5.25, total directivity pattern simulated in the presence of the long coax (dashed green curve) is totally different as compared to the simulation results obtained with the short coax (solid red line) and with the balun (dashed dotted blue line). These results reveal that the presence of the long coaxial cable in such small antenna measurements strongly affects the performance charactesteristics of the antenna while the balun can compansate for these undesired effects of the long coaxial cable.

First, measurement results will be reported for the antenna shown in Figure 5.26(a-d). The simulated and measured return loss and the normalized radiation pattern (in the xz plane directed towards the vertical (θ = 0º) direction)) for this electrically small antenna are shown in Figure 5.27 and 5.28, respectively. First of all, the single-band antenna designed to have radiation maxima along the vertical direction is fabricated and measured by a coaxial feed line without using any balun. The simulated and measured resonance frequencies for this case are found to be 1.948 GHz and 2.065 GHz with the corresponding $|S_{11}|_{min}$ values being -21.98 dB and -6.23 dB. Then, the sleeve balun design given in the Figure 5.23 is included in both simulation and measurement procedures. For this case, the simulated and measured resonance frequencies for the antenna with the sleeve balun are found to be 1.948 GHz and 2.05 GHz with the corresponding $|S_{11}|_{min}$ values being -25.53 dB and -9.66 dB, respectively. The error between the simulated and measured resonance frequencies is 5.24 percent for this antenna with balun. It is also seen that the measured return loss is improved from -6.23 dB to -9.66 dB due to the use of balun. Finally, the simulated and measured normalized radiation patterns of this antenna with the sleeve balun are obtained in the as shown in Figure 5.28 with very good agreement. Thus, the antenna design with vertically directed radiation pattern in the xz plane (θ = 0º) is verified experimentally.

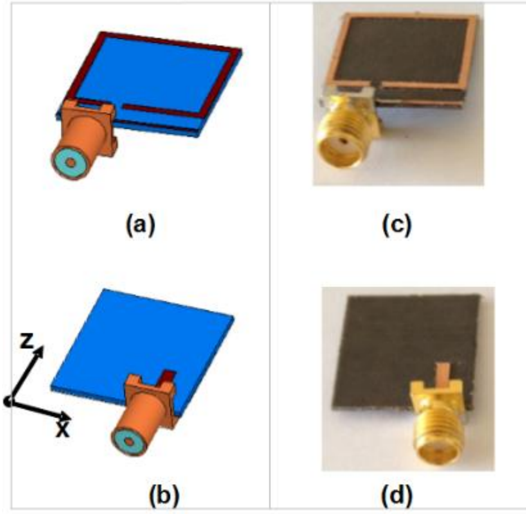

Figure 5.26: Designed and fabricated single-band antennas having their radiation patterns directed towards vertical direction ($\theta = 0^{o}$) in the xz plane: **(a)** Front and **(b)** back views of the designed antenna; **(c)** front and **(d)** back views of the fabricated antenna.

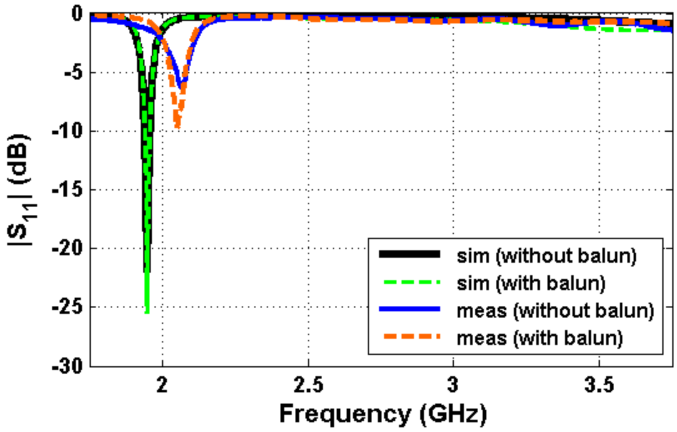

Figure 5.27: Simulated and measured return loss ($|S_{11}|$ versus frequency) for the single-band antenna (shown in Figure 5.26) with and without the balun.

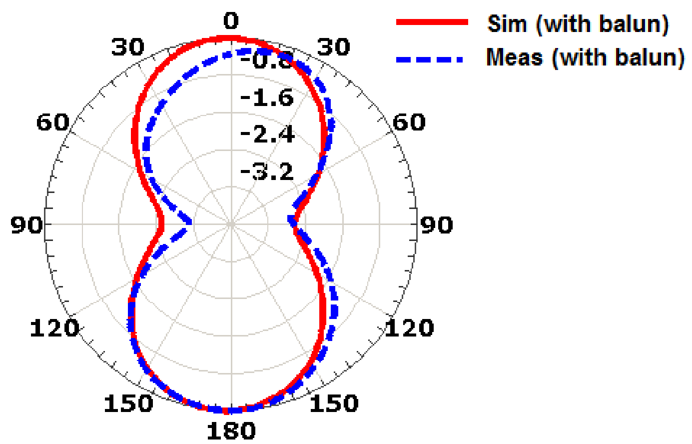

Figure 5.28: Normalized radiation pattern of the single-band antenna having its radiation patterns in the xz plane directed towards vertical (θ = 0º).

Second, measurement results will be reported for the antenna shown in Figure 5.29(a-d). The simulated and measured return loss and the normalized radiation pattern (in the xz plane directed towards the diagonal (θ = 45º) direction)) for this electrically small antenna are shown in Figure 5.30 and 5.31, respectively. First of all, the single-band antenna designed to have radiation maxima along the diagonal direction is fabricated and measured by a coaxial feed line without using any balun. The simulated and measured resonance frequencies for this case are found to be 1.951 GHz and 1.968 GHz with the corresponding $|S_{11}|_{min}$ values being -27.31 dB and -5.97 dB. Then, the sleeve balun design given in the Figure 5.23 is included in both simulation and measurement procedures. For this case, the simulated and measured resonance frequencies for the antenna with the sleeve balun are found to be 1.942 GHz and 1.945 GHz with the corresponding $|S_{11}|_{min}$ values being -27.64 dB and -14.69 dB, respectively. The error between the simulated and measured resonance frequencies is 0.15 percent for this antenna with balun. It is also seen that the measured return loss is improved from -5.97 dB to -14.69 dB due to the use of balun. Finally, the simulated and measured normalized radiation patterns of this antenna with the sleeve balun are obtained in the as shown in Figure 5.31 with very good agreement. Thus, the antenna design with diagonally directed radiation pattern in the xz plane (θ = 45º) is verified experimentally.

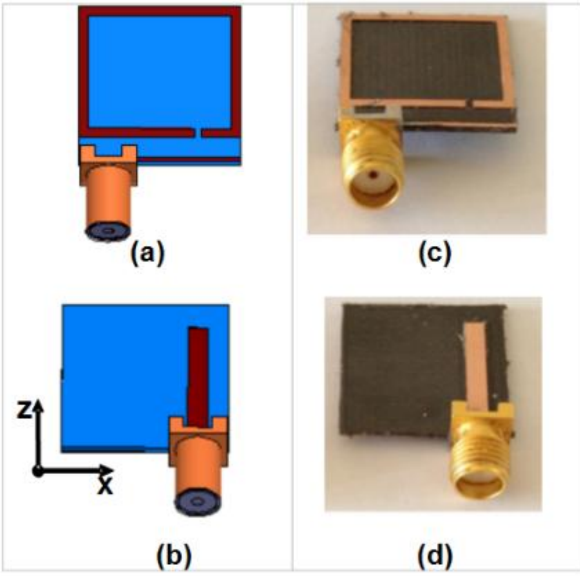

Figure 5.29: Designed and fabricated single-band antennas having their radiation patterns directed towards diagonal direction (θ = 45º) in the xz plane: **(a)** Front and **(b)** back views of the designed antenna; **(c)** front and **(d)** back views of the fabricated antenna.

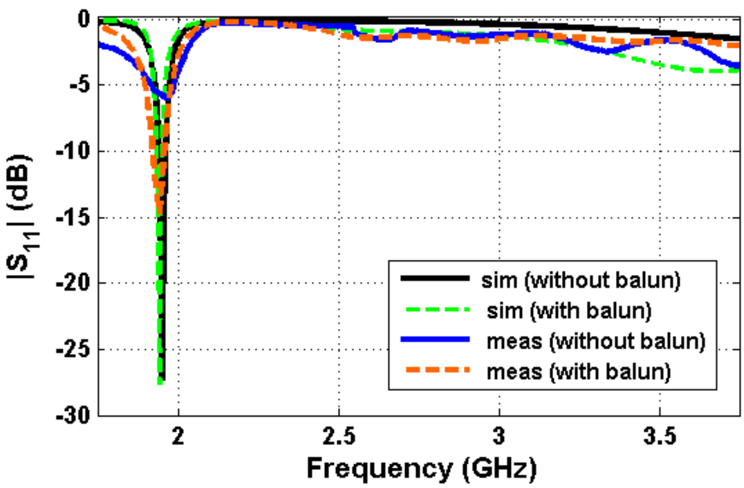

Figure 5.30: Simulated and measured return loss ($|S_{11}|$ versus frequency) for the single-band antenna (shown in Figure 5.29) with and without the balun.

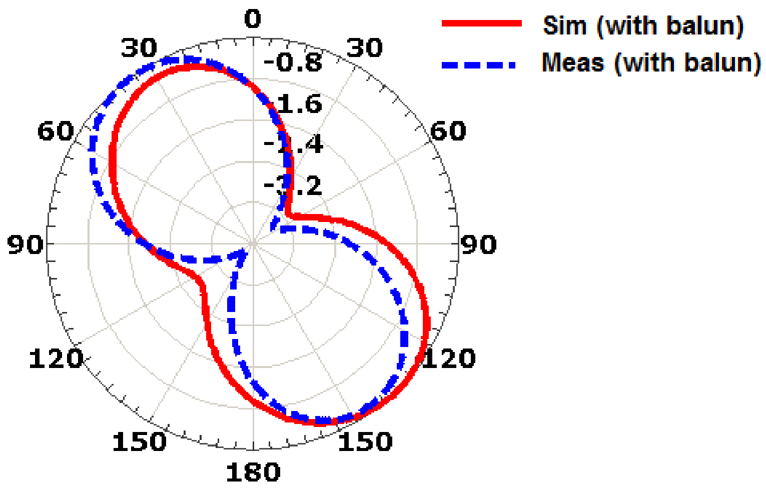

Figure 5.31: Normalized radiation pattern of the single-band antenna having its radiation patterns in the xz plane directed towards diagonal (θ = 45º).

Finally, measurement results will be reported for the antenna shown in Figure 5.32(a-d). The simulated and measured return loss and the normalized radiation pattern (in the xz plane directed towards the horizontal (θ = 90º) direction)) for this electrically small antenna are shown in Figure 5.33 and 5.34, respectively. First of all, the single-band antenna designed to have radiation maxima along the horizontal direction is fabricated and measured by a coaxial feed line without using any balun. The simulated and measured resonance frequencies for this case are found to be 1.957 GHz and 1.998 GHz with the corresponding $|S_{11}|_{min}$ values being -22.82 dB and -8.08 dB. Then, the sleeve balun design given in the Figure 5.23 is included in both simulation and measurement procedures. For this case, the simulated and measured resonance frequencies for the antenna with the sleeve balun are found to be 1.937 GHz and 1.99 GHz with the corresponding $|S_{11}|_{min}$ values being -27.03 dB and -10.84 dB, respectively. The error between the simulated and measured resonance frequencies is 2.74 percent for this antenna with balun. It is also seen that the measured return loss is improved from -8.08 dB to -10.84 dB due to the use of balun. Finally, the simulated and measured normalized radiation patterns of this antenna with the sleeve balun are obtained in the as shown in Figure 5.34 with an acceptable error. Thus, the antenna design with horizontally directed radiation pattern in the xz plane (θ = 90º) is verified experimentally.

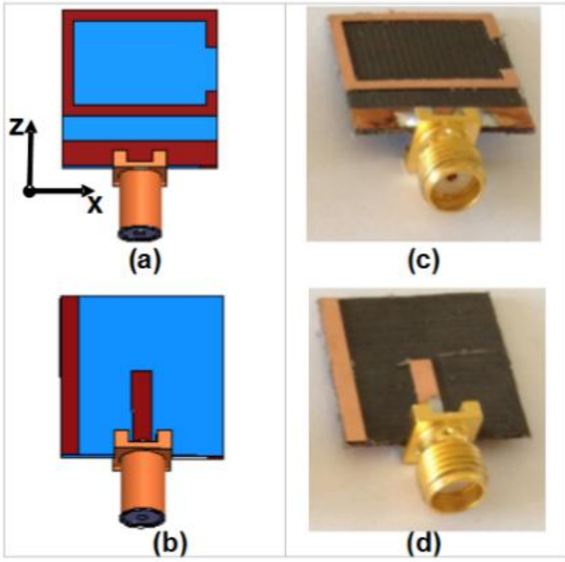

Figure 5.32: Designed and fabricated single-band antennas having their radiation patterns directed towards horizontal direction (θ = 90º) in the xz plane: **(a)** Front and **(b)** back views of the designed antenna; **(c)** front and **(d)** back views of the fabricated antenna.

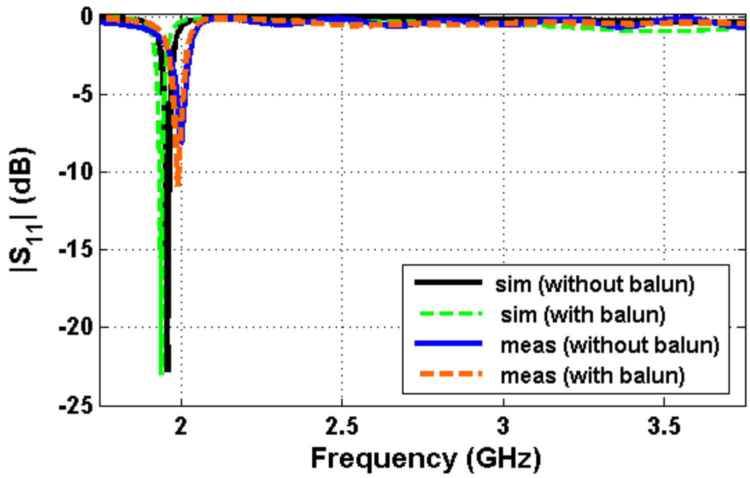

Figure 5.33: Simulated and measured return loss ($|S_{11}|$ versus frequency) for the single-band antenna (shown in Figure 5.32) with and without the balun.

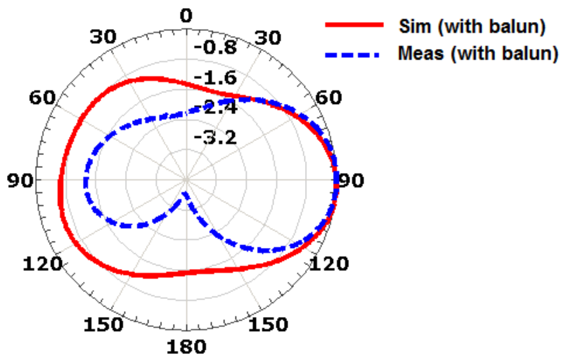

Figure 5.34: Normalized radiation pattern of the single-band antenna having its radiation patterns in the xz plane directed towards horizontal ($\theta = 90^{o}$).

In summary, steerability of the radiation pattern is demonstrated in this subsection for the novel single-band metamaterial inspired antenna.

5.6 Experimental Results for the Dual- and Triple-Band Antennas with Vertically Directed Radiation Patterns

In this section, the return loss spectra for the dual-band and triple-band metamaterial inspired antennas having their radiation patterns in the xz plane directed towards vertical ($\theta = 0^{o}$) are reported both numerically and experimentally.

Firstly, the simulated and measured $|S_{11}|$ values for the dual-band antenna, which is shown in Figure 5.35(a-d), are reported in Figure 5.36 with resonance frequencies of 1.952 GHz and 2.461 GHz in simulations; 2.02 GHz and 2.516 GHz in measurements. One finds that errors between simulated and measured resonance frequencies are 3.5 percent and 2.23 percent at the first and the second resonance frequencies, respectively. Furthermore, while $|S_{11}|_{min}$ (1.952 GHz) = -26.64 dB and $|S_{11}|_{min}$ (2.461 GHz) = -27.54 dB are obtained in the simulations, $|S_{11}|_{min}$ (2.02 GHz) = -15.14 dB and $|S_{11}|_{min}$ (2.516 GHz) = -14.25 dB are obtained in the measurements. Therefore, the simulated and measured return loss values are found in good agreement.

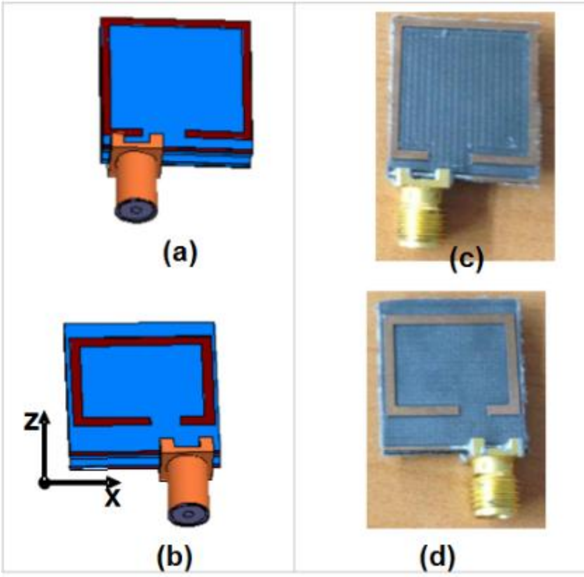

Figure 5.35: Designed and fabricated dual-band antennas having their radiation patterns directed towards vertical direction (θ = 0º) in the xz plane: **(a)** Front and **(b)** back views of the designed antenna; **(c)** front and **(d)** back views of the fabricated antenna.

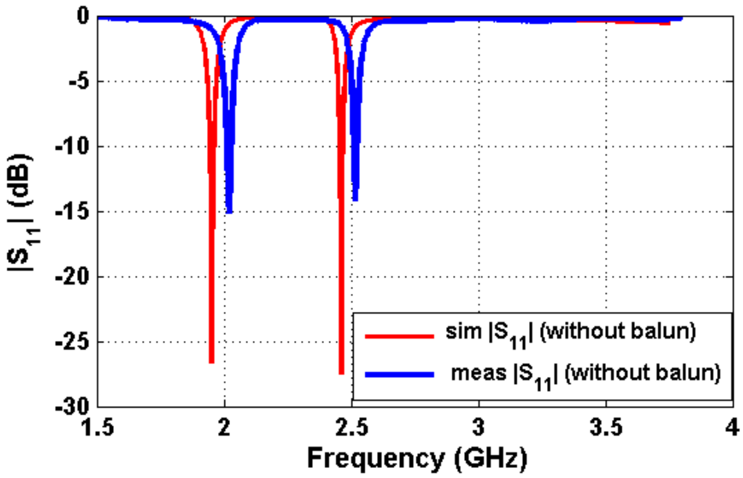

Figure 5.36: Simulated and measured return loss (|S_{11}| versus frequency) for the dual-band antenna (shown in Figure 5.35) without the balun.

Next, the simulated and measured $|S_{11}|$ values for the triple-band antenna, which is shown in Figure 5.37(a-d), are reported in Figure 5.38 with resonance frequencies of 1.944 GHz, 2.46 GHz and 3.454 GHz in simulations; 1.956 GHz, 2.482 GHz and 3.494

GHz in measurements. One finds that errors between simulated and measured resonance frequencies are 3.5 percent, 2.23 percent and 1.16 percent at the first, second and the third resonance frequencies, respectively. Furthermore, while $|S_{11}|_{min}$ (1.944 GHz) = -26.87 dB, $|S_{11}|_{min}$ (2.46 GHz) = -26.72 dB and $|S_{11}|_{min}$ (3.454 GHz) = -34.96 dB are obtained in the simulations, $|S_{11}|_{min}$ (1.956 GHz) = -20.48 dB, $|S_{11}|_{min}$ (2.482 GHz) = -16.38 dB and $|S_{11}|_{min}$ (3.494 GHz) = -18.51 dB are obtained in the measurements. Therefore, the simulated and measured return loss values are found in good agreement.

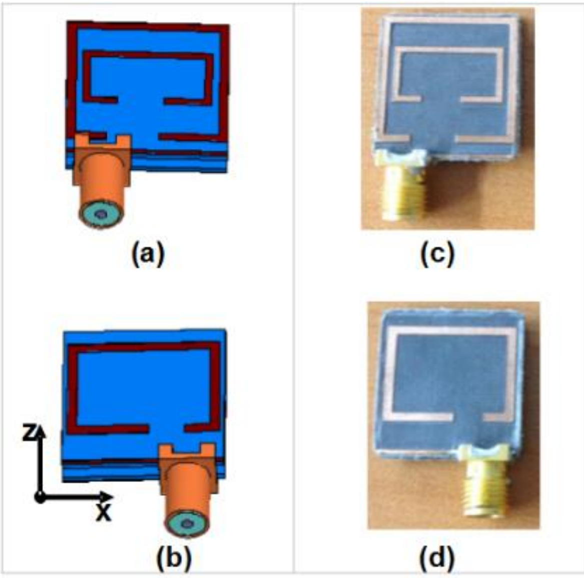

Figure 5.37: Designed and fabricated triple-band antennas having their radiation patterns directed towards vertical direction (θ = 0º) in the xz plane: **(a)** Front and **(b)** back views of the designed antenna; **(c)** front and **(d)** back views of the fabricated antenna.

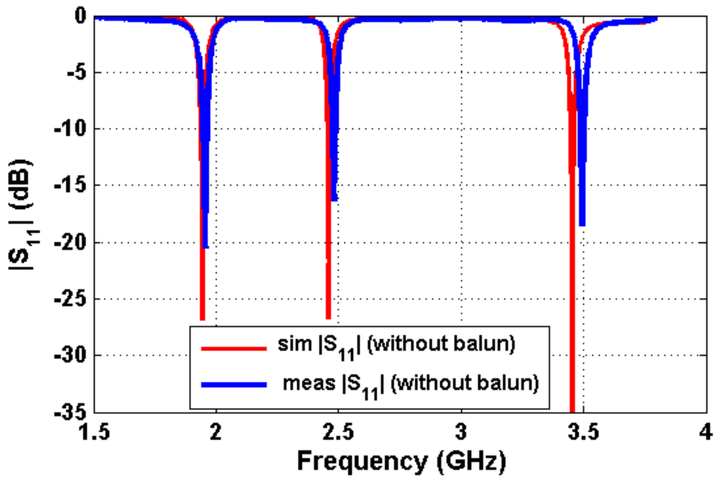

Figure 5.38: Simulated and measured return loss ($|S_{11}|$ versus frequency) for the triple-band antenna (shown in Figure 5.37) without the balun.

It should be also noted that radiation patterns of the dual-band and triple-band antennas were measured without using the balun. The agreement between the simulations and experimental results were not good enough due to the problems caused long coaxial cable, as expected. It is well known that the baluns are useful in narrow-band applications, in general. Therefore, the use of simple sleeve balun was not appropriate to correct the radiation pattern of a multi-band antenna at all operation frequencies at the same time. Design of a wideband or multi-band balun needs to be used in such applications. Therefore, only the return loss measurement results are provided for the multi-band antennas.

CHAPTER 6

CONCLUSIONS AND FUTURE STUDIES

In this dissertation, different aspects of metamaterials are studied with a particular focus on multi-band metamaterials with novel applications in antennas.

Main conclusions of this dissertation can be summarized as follows:

In the second section of Chapter 3, effects of using different boundary conditions and different computational volume dimensions in numerical simulations of periodic metamaterial arrays are presented. It is shown that use of different boundary conditions may result in the simulation of dissimilar periodic array topologies with totally different electromagnetic responses, especially in the case of unit cells having structural asymmetry with respect to the boundaries. It is also demonstrated that, as a result of variations in electromagnetic coupling between the array elements, response of the metamaterial structure may be affected strongly by changing the dimensions of the computational volume. One international journal paper [189] and one international conference paper [191] have already been published based on this study.

In the third section of Chapter 3, parameter retrieval methods reported in literature are studied with a special focus on the widely used NRW parameter retrieval method. This section aims at demonstrating the presence of unphysical results produced by NRW retrieval approach. These unphysical results are usually referred as the "anti-resonant effects" in literature, which manifest themselves as negative valued imaginary parts of permittivity and/or permeability parameters contradicting with the "passivity" requirement under the exp(-iωt) convention. Another indication for the unphysical parameter retrieval results is the violation of the Kramers-Kronig (KK) relations (i.e. the violation of the "causality" requirement) by the real and imaginary parts of the retrieved parameters. It is demonstrated in this dissertation that the parameter retrieval results given by the NRW method violates the passivity and causality requirements more strongly as the metamaterial array becomes denser. One international conference paper [178] has already been published based on this study. There is also one manuscript in preparation to be submitted to an international journal.

In the first part of Chapter 4, two novel MNG-type multi-band metamaterial designs are presented in microwave region; an M-band nested split ring resonator (M-NSRR) and an M-band nested U-ring resonator (M-NURR). The proposed topologies have M nested and unconnected metal rings printed on a dielectric substrate with aligned gaps. Single-, dual- and triple-band versions of the M-NURR topology are fabricated and measured. It is demonstrated that the number of magnetic resonances can easily be adjusted by the number of concentric rings. It has also been shown that, as compared to the alternative supercell type multi-band topologies, the proposed M-NSRR and M-NURR turn out to be electrically small designs. More importantly, any individual resonance of the M-NURR metamaterial can be adjusted in a very controlled manner without affecting the other resonances of the metamaterial. It is demonstrated that the 3-NURR design with merged frequencies further improves the MNG bandwidth. One international journal paper [49] and two international conference papers [43], [45] have already been published based on this study. There is also one manuscript in preparation to be submitted to an international journal.

In the second part of Chapter 4, single-sided and double-sided (in broadside-coupled configuration) versions of the M-NURR are investigated in order to get improved miniaturization. The results show that, in comparison with their single-sided counterparts, broadside-coupled (BC) M-NURR has much smaller resonance frequencies (hence considerably smaller electrical sizes). One international conference paper [44] has already been published based on this study.

In Chapter 5, metamaterial-inspired electrically small multi-band antennas are proposed as novel practical applications of the dissertation. These antennas are based on a coaxially-fed printed dipole integrated in a planar configuration with capacitively loaded conducting loops (CLLs). Performance characteristics of the proposed antennas are examined both numerically and experimentally. It is revealed that the number of CLLs in the proposed antenna topology determines the number of operating frequencies. It is successfully demonstrated that the novel single-band and multi-band antennas proposed in this dissertation attain high radiation efficiencies (above 77 percent) while having geometrically simple and electrically small topologies. Results show that just by adjusting the gap locations of CLLs relative to the position of feed point, radiation patterns can be steered to desired directions. One international journal paper [190] and one international conference paper [115] have already been published based on this study. There is also one manuscript in preparation to be submitted to an international journal.

Following research topics are planned as future studies:

- Developing more reliable alternative approaches to the commonly used retrieval methods based on the NRW algorithm.

- Applications of the proposed multi-band metamaterial topologies in THz and optical frequencies.

- Designing multi-band baluns to improve the measured radiation patterns of the proposed electrically small multi-band antennas.

- Use of MEMS switches for adaptive tuning of the direction of the radiation pattern maximum for proposed antennas.

- Integrate the proposed antenna designs with artificial magnetic conductor (AMC) structures to cancel the back radiation and to achieve a V-type radiation pattern.

REFERENCES

[1] V. G. Veselago, “The electrodynamics of substances with simultaneously negative values of ε and μ,” Sov Pyhs-Usp, vol. 10, no.4, pp. 509–514, 1968.

[2] D. F. Sievenpiper, M. E. Sickmiller, and E. Yablonovitch, “3D wire mesh photonic crystals,” Phys. Rev. Lett., vol. 76, no. 14, pp. 2480-2483, 1996.

[3] J. B. Pendry, A. J. Holden, W. J. Stewart, and I. Youngs, “Extremely low frequency plasmons in metallic mesostructures,” Phys. Rev. Lett., vol. 76, no. 25, pp. 4773–4776, 1996.

[4] D. F. Sievenpiper, E. Yablonovitch, J. N. Winn, S. Fan, P. R. Villeneuve, and J. D. Joannopoulos, “3D metallo-dielectric photonic crystals with strong capacitive coupling between metallic islands,” Phys. Rev. Lett., vol. 80, no. 13, pp. 2829-2832, 1998.

[5] J. B. Pendry, A. J. Holden, D. J. Robbins, and W. J. Stewart, “Low frequency plasmons in thin-wire structures,” J. Phys. Condens. Matter, vol. 10, no. 22, pp. 4785-4809, 1998.

[6] A. N. Lagarkov, V. N. Semenenko, V. A. Chistyaev, D. E. Ryabov, S. A. Tretyakov, and C. R. Simovski, “Resonance properties of bi-helix media at microwaves,” Electromagnetics, vol. 17, no. 3, pp. 213–237, 1997.

[7] J. B. Pendry, A. J. Holden, D. J. Robbins, and W. J. Stewart, “Magnetism from conductors and enhanced nonlinear phenomena,” IEEE Trans. Microw. Theory Tech., vol. 47, no. 11, pp. 2075–2084, 1999.

[8] D. R. Smith, W. J. Padilla, D. C. Vier, S. C. Nemat-Nasser, and S. Schultz, “Composite medium with simultaneously negative permeability and permittivity,” Phys. Rev. Lett., vol. 84, no. 18, pp. 4184–4187, 2000.

[9] R. A. Shelby, D. R. Smith, S. C. Nemat-Nasser, and S. Schultz, “Microwave transmission through a two-dimensional, isotropic, left-handed metamaterial,” Appl. Phys. Lett., vol. 78, no. 4, pp. 489-491, 2001.

[10] R. A. Shelby, D. R. Smith, S. Schultz, “Experimental verification of a negative index of refraction,” Science, vol. 292, no. 5514, pp. 77–79, 2001.

[11] R. W. Ziolkowski and E. Heyman, “Wave propagation in media having negative permittivity and permeability,” Phys. Rev. E, vol. 64, no. 5, pp. 56625(1)-(15), 2001.

[12] D. R. Smith, P. Kolinko, and D. Schurig, “Negative refraction in indefinite media,” J. Opt. Soc. Am. B, vol. 21, no. 5, pp. 1032–1043, 2004.

[13] S. A. Ramakrishna, “Physics of negative refractive index materials,” Rep. Prog. Phys., vol. 68, no. 2, pp. 449–521, 2005.

[14] A. B. Kozyrev and D. W. Van Der Weide, “Nonlinear wave propagation phenomena in left-handed transmission-line media,” IEEE Trans. Microw. Theory Tech., vol. 53, no. 1, pp. 238–245, 2005.

[15] Z. Szabo, G.-H. Park, R. Hedge, and E.-P. Li, “A unique extraction of metamaterial parameters based on Kramers–Kronig relationship,” IEEE Trans. Microw. Theory Tech., vol. 58, no. 10, pp. 2646–2653, 2010.

[16] A. Grbic and G. V. Eleftheriades, “Experimental verification of backward-wave radiation from a negative refractive index metamaterial,” J. Appl. Phys., vol. 92, no. 10, pp. 5930-5935, 2002.

[17] J. F. Woodley and M. Mojahedi, “Negative group velocity and group delay in left-handed media,” Phys. Rev. E, vol. 70, no. 4, pp. 46603(1)-(6), 2004.

[18] K. Aydin, K. Guven, C. M. Soukoulis, and E. Ozbay, “Observation of negative refraction and negative phase velocity in left-handed metamaterials,” Appl. Phys. Lett., vol. 86, no. 12, pp. 124102(1)-(3), 2005.

[19] G. M. Gehring, A. Schweinsberg, C. Barsi, N. Kostinski and R. W. Boyd, “Observation of backward pulse propagation through a medium with a negative group velocity,” Science, vol. 312, no. 5775, pp. 895–897, 2006.

[20] T. J. Yen, W. J. Padilla, N. Fang, D. C. Vier, D. R. Smith, J. B. Pendry, D. N. Basov, and X. Zhang, “Terahertz magnetic response from artificial materials,” Science, vol. 303, no. 5663, pp. 1494–1496, 2004.

[21] S. Linden, C. Enkrich, M. Wegener, J. Zhou, T. Koschny and C. M. Soukoulis , “Magnetic response of metamaterials at 100 terahertz,” Science, vol. 306, no. 5700, pp. 1351–1353, Nov. 2004.

[22] V. M. Shalaev, W. Cai, U. K. Chettiar, H.-K. Yuan, A. K. Sarychev, V. P. Drachev, and A. V. Kildishev, “Negative index of refraction in optical metamaterials,” Opt. Lett., vol. 30, no. 24, pp. 3356–3358, 2005.

[23] G. Dolling, C. Enkrich, M. Wegener, C. M. Soukoulis and S. Linden, “Simultaneous negative phase and group velocity of light in a metamaterial,” Science, vol. 312, no. 5775, pp. 892–894, 2006.

[24] S. Zhang, W. Fan, N. Panoiu, K. J. Malloy, R. M. Osgood, and S. Brueck, “Experimental demonstration of near-infrared negative-Index metamaterials,” Phys. Rev. Lett., vol. 95, no. 13, pp. 137404(1)-(4), 2005.

[25] D. R. Smith, D. C. Vier, W. Padilla, S. C. Nemat-Nasser, and S. Schultz, “Loop-wire medium for investigating plasmons at microwave frequencies,” Appl. Phys. Lett., vol. 75, no. 10, pp. 1425-1427, 1999.

[26] F. Falcone, T. Lopetegi, M. Laso, J. D. Baena, J. Bonache, M. Beruete, R. Marqués, F. Martín, and M. Sorolla, “Babinet principle applied to the design of metasurfaces and metamaterials,” Phys. Rev. Lett., vol. 93, no. 19, pp. 197401(1)-(4), 2004.

[27] D. Schurig, J. J. Mock, and D. R. Smith, “Electric-field-coupled resonators for negative permittivity metamaterials,” Appl. Phys. Lett., vol. 88, no. 4, pp. 041109(1)-(4), 2006.

[28] R. Liu, A. Degiron, J. J. Mock, and D. R. Smith, “Negative index material composed of electric and magnetic resonators,” Appl. Phys. Lett., vol. 90, no. 26, pp. 263504(1)-(3), 2007.

[29] A. Dhouibi, S. N. Burokur, A. de Lustrac, and A. Priou, “Comparison of compact electric-LC resonators for negative permittivity metamaterials,” Microw. Opt. Technol. Lett., vol. 54, no. 10, pp. 2287–2295, 2012.

[30] J. D. Baena, L. Jelinek, R. Marqués, and J. Zehentner, “Electrically small isotropic three-dimensional magnetic resonators for metamaterial design,” Appl. Phys. Lett., vol. 88, no. 13, pp. 134108(1)-(3), 2006.

[31] F. Bilotti, A. Toscano, and L. Vegni, “Design of spiral and multiple split-ring resonators for the realization of miniaturized metamaterial samples,” IEEE Trans. Antennas Propag., vol. 55, no. 8, pp. 2258–2267, 2007.

[32] F. Zhang, Q. Zhao, L. Kang, D. P. Gaillot, X. Zhao, J. Zhou, and D. Lippens, “Magnetic control of negative permeability metamaterials based on liquid crystals,” Appl. Phys. Lett., vol. 92, no. 19, pp. 193104(1)-(3), 2008.

[33] J. Wang, S. Qu, Z. Xu, H. Ma, Y. Yang, and C. Gu, “A controllable magnetic metamaterial: split-ring resonator with rotated inner ring,” IEEE Trans. Antennas Propag., vol. 56, no. 7, pp. 2018–2022, 2008.

[34] O. Kasyutich, A. Sarua, and W. Schwarzacher, “Bioengineered magnetic crystals,” J. Phys. D: Appl. Phys., vol. 41, no. 13, pp. 134022(1)-(3), 2008.

[35] E. Ekmekci, K. Topalli, T. Akin, and G. Turhan-Sayan, “A tunable multi-band metamaterial design using micro-split SRR structures,” Opt. Express, vol. 17, no. 18, pp. 16046–16058, 2009.

[36] S. Xiao, U. K. Chettiar, A. V. Kildishev, V. Drachev, I. C. Khoo, and V. M. Shalaev, “Tunable magnetic response of metamaterials,” Appl. Phys. Lett., vol. 95, no. 3, pp. 033115(1)-(3), 2009.

[37] E. Ekmekci and G. Turhan-Sayan, “Single loop resonator: dual-band magnetic metamaterial structure,” Electron. Lett., vol. 46, no. 5, pp. 324–325, 2010.

[38] F. Zhang, Q. Zhao, W. Zhang, J. Sun, J. Zhou, and D. Lippens, “Voltage tunable short wire-pair type of metamaterial infiltrated by nematic liquid crystal,” Appl. Phys. Lett., vol. 97, no. 13, pp. 134103(1)-(3), 2010.

[39] Q. Li, W. Lin, and G. P. Wang, “An optical magnetic metamaterial working at multiple frequencies simultaneously,” Appl. Phys. Lett., vol. 99, no. 4, pp. 041109(1)-(3), 2011.

[40] X. He, Z. Lv, B. Liu, and Z. Li, “Tunable magnetic metamaterial based multi-split-ring resonator (MSRR) using MEMS switch components,” Microsyst. Technol., vol. 17, no. 8, pp. 1263–1269, 2011.

[41] Y.-H. Yang, I.-W. Un, H.-C. Lee, and T.-J. Yen, “Magnetic surface polariton in a planar biaxial metamaterial with dual negative magnetic permeabilities,” Plasmonics, vol. 7, no. 1, pp. 87–92, 2011.

[42] F.-Y. Meng, F. Zhang, K. Zhang, Q. Wu, J.-Y. Kim, J.-J. Choi, B. Lee, and J.-C. Lee, “Low-loss magnetic metamaterial based on analog of electromagnetically induced transparency,” IEEE Trans. Magn., vol. 47, no. 10, pp. 3347–3350, 2011.

[43] O. Turkmen, E. Ekmekci, and G. Turhan-Sayan, “Parametric investigation of a new multi-band metamaterial design: U-shaped multiple ring magnetic resonators,” 2011 IEEE International Symposium on Antennas and Propagation (APSURSI), Spokane, USA, 2011, pp. 1516–1518.

[44] O. Turkmen, E. Ekmekci, and G. Turhan-Sayan, “Miniaturization of U-shaped multi-band metamaterial structures,” 2011 XXXth URSI General Assembly and Scientific Symposium , Istanbul, Turkey, 2011, pp. 1–4.

[45] O. Turkmen, E. Ekmekci, and G. Turhan-Sayan, “A new multi-ring SRR type metamaterial design with multiple magnetic resonances,” Progress In Electromagnetics Research Symposium Proceedings (PIERS), Marrakesh, Morocco, 2011, pp. 315-319.

[46] A. Agrawal, W. Park, and R. Piestun, “Negative permeability with arrays of aperiodic silver nanoclusters,” Appl. Phys. Lett., vol. 101, no. 8, pp. 083109(1)-(4), 2012.

[47] H. Nemec, C. Kadlec, F. Kadlec, P. Kuzel, R. Yahiaoui, U.-C. Chung, C. Elissalde, M. Maglione, and P. Mounaix, “Resonant magnetic response of TiO_2 microspheres at terahertz frequencies,” Appl. Phys. Lett., vol. 100, no. 6, pp. 061117(1)–(4), 2012.

[48] C. Sabah, “Multi-resonant metamaterial design based on concentric V-shaped magnetic resonators,” J. Electromagn. Waves Appl., vol. 26, no. 8–9, pp. 1105–1115, 2012.

[49] O. Turkmen, E. Ekmekci, and G. Turhan-Sayan, “Nested U-ring resonators: a novel multi-band metamaterial design in microwave region,” IET Microw. Antennas Propag., vol. 6, no. 10, pp. 1102-1108, 2012.

[50] K. Fan, A. C. Strikwerda, R. D. Averitt, and X. Zhang, “Three-dimensional magnetic terahertz metamaterials using a multilayer electroplating technique,” J. Micromechanics Microengineering, vol. 22, no. 4, pp. 045011(1)-(9), 2012.

[51] F. Chen, L. Yuan, and R. L. Johnston, “Low-loss optical magnetic metamaterials on Ag–Au bimetallic fishnets,” Jounal of Magnetism and Magnetic Materials, vol. 324, no. 17, pp. 2625–2630, 2012.

[52] K. Zhang, Q. Wu, J.-H. Fu, F.-Y. Meng, and L.-W. Li, “Metamaterials with tunable negative permeability based on mie resonance,” IEEE Trans. Magn., vol. 48, no. 11, pp. 4289–4292, 2012.

[53] H.-X. Xu, G.-M. Wang, and M.-Q. Qi, “Hilbert-shaped magnetic waveguided metamaterials for electromagnetic coupling reduction of microstrip antenna array,” IEEE Trans. Magn., vol. 49, no. 4, pp. 1526–1529, 2013.

[54] C. Sabah and F. Urbani, “Experimental analysis of Λ-shaped magnetic resonator for mu-negative metamaterials,” Opt. Commun., vol. 294, pp. 409–413, 2013.

[55] J. Huangfu, L. Ran, H. Chen, X. Zhang, K. Chen, T. M. Grzegorczyk, and J. A. Kong, “Experimental confirmation of negative refractive index of a metamaterial composed of Ω-like metallic patterns,” Appl. Phys. Lett., vol. 84, no. 9, pp. 1537-1539, 2004.

[56] R. X. Wu, “Effective negative refraction index in periodic metal–ferrite–metal film composite,” J. Appl. Phys., vol. 97, no. 7, pp. 076105(1)-(3), 2005.

[57] S. M. Rudolph and A. Grbic, “Volumetric negative-refractive-index medium exhibiting broadband negative permeability,” J. Appl. Phys., vol. 102, no. 1, pp. 013904(1)-(6), 2007.

[58] C. M. Soukoulis, S. Linden and M. Wegener, “PHYSICS: Negative refractive index at optical,” Science, vol. 315, no. 5808, pp. 47-49, 2007.

[59] X. Wang, D.-H. Kwon, D. H. Werner, I.-C. Khoo, A. V. Kildishev, and V. M. Shalaev, “Tunable optical negative-index metamaterials employing anisotropic liquid crystals,” Appl. Phys. Lett., vol. 91, no. 14, pp. 143122(1)-(3), 2007.

[60] W. Zhu, X. Zhao, and N. Ji, “Double bands of negative refractive index in the left-handed metamaterials with asymmetric defects,” Appl. Phys. Lett., vol. 90, no. 1, pp. 011911(1)-(3), 2007.

[61] W. Wu, E. Kim, E. Ponizovskaya, Y. Liu, Z. Yu, N. Fang, Y. R. Shen, A. M. Bratkovsky, W. Tong, C. Sun, X. Zhang, S.-Y. Wang, and R. S. Williams, “Optical metamaterials at near and mid-IR range fabricated by nanoimprint lithography,” Appl. Phys. A, vol. 87, no. 2, pp. 143–150, 2007.

[62] Q. Wu and W. Park, “Negative index materials based on metal nanoclusters,” Appl. Phys. Lett., vol. 92, no. 15, pp. 153114(1)-(3), 2008.

[63] J. A. Bossard, X. Liang, L. Li, S. Yun, D. H. Werner, B. Weiner, T. S. Mayer, P. F. Cristman, A. Diaz, and I. C. Khoo, “Tunable frequency selective surfaces and negative-zero-positive index metamaterials based on liquid crystals,” IEEE Trans. Antennas Propag., vol. 56, no. 5, pp. 1308–1320, 2008.

[64] J. Valentine, S. Zhang, T. Zentgraf, E. Ulin-Avila, D. A. Genov, G. Bartal, and X. Zhang, “Three-dimensional optical metamaterial with a negative refractive index,” Nature, vol. 455, no. 7211, pp. 376–379, 2008.

[65] S. N. Burokur, T. Lepetit, and A. de Lustrac, “Incidence dependence of negative index in asymmetric cut wire pairs metamaterials,” Appl. Phys. Lett., vol. 95, no. 19, pp. 191114(1)-(3), 2009.

[66] B. Wang, J. Zhou, T. Koschny, and C. M. Soukoulis, “Nonplanar chiral metamaterials with negative index,” Appl. Phys. Lett., vol. 94, no. 15, pp. 151112(1)-(3), 2009.

[67] C. Zhu, J.-J. Ma, L. Chen, and C.-H. Liang, “Negative index metamaterials composed of triangular open-loop resonator and wire structures,” Microw. Opt. Technol. Lett., vol. 51, no. 9, pp. 2022–2025, 2009.

[68] D. Kim, W. Lee, and J. Choi, “A simple design method of negative refractive index metamaterials,” Appl. Phys. A, vol. 97, no. 2, pp. 461–467, 2009.

[69] Z. Li, R. Zhao, T. Koschny, M. Kafesaki, K. B. Alici, E. Colak, H. Caglayan, E. Ozbay, and C. M. Soukoulis, “Chiral metamaterials with negative refractive index based on four ‘U’ split ring resonators,” Appl. Phys. Lett., vol. 97, no. 8, pp. 081901(1)-(3), 2010.

[70] S. P. Burgos, R. de Waele, A. Polman, and H. A. Atwater, “A single-layer wide-angle negative-index metamaterial at visible frequencies,” Nat. Mater., vol. 9, no. 5, pp. 407–412, 2010.

[71] S. Xiao, V. P. Drachev, A. V. Kildishev, X. Ni, U. K. Chettiar, H.-K. Yuan, and V. M. Shalaev, “Loss-free and active optical negative-index metamaterials,” Nature, vol. 466, no. 7307, pp. 735–738, 2010.

[72] Z. Li, K. B. Alici, E. Colak, and E. Ozbay, “Complementary chiral metamaterials with giant optical activity and negative refractive index,” Appl. Phys. Lett., vol. 98, no. 16, pp. 161907(1)-(3), 2011.

[73] K. Lodewijks, N. Verellen, W. Van Roy, V. Moshchalkov, G. Borghs, and P. Van Dorpe, “Self-assembled hexagonal double fishnets as negative index materials,” Appl. Phys. Lett., vol. 98, no. 9, pp. 091101(1)-(3), 2011.

[74] K. J. Nicholson, W. S. T. Rowe, and K. Ghorbani, “Design and demonstration of a metamaterial with electronically tunable negative refraction across the C microwave band,” IET Microw. Antennas Propag., vol. 5, no. 6, pp. 631-636, 2011.

[75] A. Ourir and H. H. Ouslimani, “Negative refractive index in symmetric cut-wire pair metamaterial,” Appl. Phys. Lett., vol. 98, no. 11, p. 113505(1)-(3), 2011.

[76] L. Fok and X. Zhang, “Negative acoustic index metamaterial,” Phys. Rev. B, vol. 83, no. 21, pp. 214304(1)-(8), 2011.

[77] N.-H. Shen, L. Zhang, T. Koschny, B. Dastmalchi, M. Kafesaki, and C. M. Soukoulis, “Discontinuous design of negative index metamaterials based on mode hybridization,” Appl. Phys. Lett., vol. 101, no. 8, pp. 081913(1)-(3), 2012.

[78] M. Giloan and S. Astilean, “Designing polarization insensitive negative index metamaterial for operation in near infrared,” Opt. Commun., vol. 285, no. 8, pp. 2195–2200, 2012.

[79] S. M. Rudolph and A. Grbic, “A broadband three-dimensionally isotropic negative-refractive-index medium,” IEEE Trans. Antennas Propag., vol. 60, no. 8, pp. 3661–3669, 2012.

[80] L. Zhang, T. Koschny, and C. M. Soukoulis, “Creating double negative index materials using the Babinet principle with one metasurface,” Phys. Rev. B, vol. 87, no. 4, pp. 045101(1)-(5), 2013.

[81] Y. Z. Cheng, Y. Nie, Z. Z. Cheng, X. Wang, and R. Z. Gong, “Chiral metamaterials with giant optical activity and negative refractive index based on complementary conjugate-swastikas structure,” J. Electromagn. Waves Appl., vol. 27, no. 8, pp. 1068–1076, 2013.

[82] H. Tao, N. I. Landy, C. M. Bingham, X. Zhang, R. D. Averitt, and W. J. Padilla, “A metamaterial absorber for the terahertz regime: Design, fabrication and characterization,” Opt. Express, vol. 16, no. 10, pp. 7181–7188, 2008.

[83] N. I. Landy, S. Sajuyigbe, J. J. Mock, D. R. Smith, and W. J. Padilla, “Perfect metamaterial absorber,” Phys. Rev. Lett., vol. 100, no. 20, pp. 207402(1)-(3), 2008.

[84] H. Tao, C. Bingham, A. Strikwerda, D. Pilon, D. Shrekenhamer, N. I. Landy, K. Fan, X. Zhang, W. J. Padilla, and R. D. Averitt, “Highly flexible wide angle of incidence terahertz metamaterial absorber: design, fabrication, and characterization,” Phys. Rev. B, vol. 78, no. 24, pp. 241103(1)-(4), 2008.

[85] C. Hu, L. Liu, Z. Zhao, X. Chen, and X. Luo, “Mixed plasmons coupling for expanding the bandwidth of near-perfect absorption at visible frequencies,” Opt. Express, vol. 17, no. 19, pp. 16745–16749, 2009.

[86] C. Hu, Z. Zhao, X. Chen, and X. Luo, “Realizing near-perfect absorption at visible frequencies,” Opt. Express, vol. 17, no. 13, pp. 11039–11044, 2009.

[87] J. Hao, J. Wang, X. Liu, W. J. Padilla, L. Zhou, and M. Qiu, “High performance optical absorber based on a plasmonic metamaterial,” Appl. Phys. Lett., vol. 96, no. 25, pp. 251104(1)-(3), 2010.

[88] X. Liu, T. Starr, A. F. Starr, and W. J. Padilla, “Infrared Spatial and Frequency Selective metamaterial with near-unity absorbance,” Phys. Rev. Lett., vol. 104, no. 20, pp. 207403(1)-(4), 2010.

[89] N. Liu, M. Mesch, T. Weiss, M. Hentschel, and H. Giessen, “Infrared perfect absorber and its application as plasmonic sensor,” Nano Lett., vol. 10, no. 7, pp. 2342–2348, 2010.

[90] Y. Cheng, H. Yang, Z. Cheng, and B. Xiao, “A planar polarization-insensitive metamaterial absorber,” Photonics Nanostructures - Fundam. Appl., vol. 9, no. 1, pp. 8–14, 2011.

[91] L. Lu, S. Qu, H. Ma, F. Yu, S. Xia, Z. Xu, and P. Bai, “A polarization-independent wide-angle dual directional absorption metamaterial absorber,” Prog. Electromagn. Res. M, vol. 27, pp. 191–201, 2012.

[92] P. V. Tuong, V. D. Lam, J. W. Park, E. H. Choi, S. A. Nikitov, and Y. P. Lee, “Perfect-absorber metamaterial based on flower-shaped structure,” Photonics Nanostructures - Fundam. Appl., vol. 11, no. 1, pp. 89–94, 2013.

[93] M.-H. Li, S.-Y Liu, L.-Y. Guo, H. Lin, H.-L. Yang, and B. Xiao, “Influence of the dielectric-spacer thickness on the dual-band metamaterial absorber,” Opt. Commun., vol. 295, pp. 262–267, 2013.

[94] Y. Cheng, Y. Nie, and R. Gong, “A polarization-insensitive and omnidirectional broadband terahertz metamaterial absorber based on coplanar multi-squares films,” Opt. Laser Technol., vol. 48, pp. 415–421, 2013.

[95] Y. Song, C. Wang, Y. Lou, B. Cao, and X. Li, “Near-perfect absorber with ultrawide bandwidth in infrared region using a periodically chirped structure,” Opt. Commun., vol. 305, pp. 212–216, 2013.

[96] D. Sievenpiper, L. Zhang, R. F. Jimenez Broas, N. G. Alexopolous, and E. Yablonovitch, “High-impedance electromagnetic surfaces with a forbidden frequency band,” IEEE Trans. Microw. Theory Tech., vol. 47, no. 11, pp. 2059–2074, 1999.

[97] B. Temelkuran, M. Bayindir, E. Ozbay, R. Biswas, M. M. Sigalas, G. Tuttle, and K. M. Ho, “Photonic crystal-based resonant antenna with a very high directivity,” J. Appl. Phys., vol. 87, no. 1, pp. 603-605, 2000.

[98] Y. Zhang, J. von Hagen, and W. Wiesbeck, “Patch array as artificial magnetic conductors for antenna gain improvement,” Microw. Opt. Technol. Lett., vol. 35, no. 3, pp. 172–175, 2002.

[99] J. McVay, N. Engheta, and A. Hoorfar, “High impedance metamaterial surfaces using Hilbert-curve inclusions,” IEEE Microw. Wirel. Compon. Lett., vol. 14, no. 3, pp. 130–132, 2004.

[100] A.-K. Hamid, “Axially slotted antenna on a circular or elliptic cylinder coated with metamaterials,” Prog. Electromagn. Res., vol. 51, pp. 329–341, 2005.

[101] A. V. Kudrin, E. Y. Petrov, G. A. Kyriacou, and T. M. Zaboronkova, “Insulated cylindrical antenna in a cold magnetoplasma,” Prog. Electromagn. Res., vol. 53, pp. 135–166, 2005.

[102] B.-I. Wu, W. Wang, J. Pacheco, X. Chen, T. Grzegorczyk, and J. A. Kong, "A study of using metamaterials as antenna substrate to enhance gain," Prog. Electromagn. Res., vol. 51, pp. 295–328, 2005.

[103] A. Erentok, P. L. Luljak, and R. W. Ziolkowski, "Characterization of a volumetric metamaterial realization of an artificial magnetic conductor for antenna applications," IEEE Trans. Antennas Propag., vol. 53, no. 1, pp. 160–172, Jan. 2005.

[104] K. B. Alici and E. Ozbay, "Electrically small split ring resonator antennas," J. Appl. Phys., vol. 101, no. 8, pp. 083104(1)-(4), 2007.

[105] F. Zhang, S. Potet, J. Carbonell, E. Lheurette, O. Vanbesien, Xiaopeng Zhao, and D. Lippens, "Negative-zero-positive refractive index in a prism-like omega-type metamaterial," IEEE Trans. Microw. Theory Tech., vol. 56, no. 11, pp. 2566–2573, Nov. 2008.

[106] O. S. Kim and O. Breinbjerg, "Miniaturised self-resonant split-ring resonator antenna," Electron. Lett., vol. 45, no. 4, pp. 196–197, 2009.

[107] K. B. Alici, A. E. Serebryannikov, and E. Ozbay, "Radiation properties and coupling analysis of a metamaterial based, dual polarization, dual band, multiple split ring resonator antenna," J. Electromagn. Waves Appl., vol. 24, no. 8–9, pp. 1183–1193, 2010.

[108] O. S. Kim, "Low-Q electrically small spherical magnetic dipole antennas," IEEE Trans. Antennas Propag., vol. 58, no. 7, pp. 2210–2217, 2010.

[109] I. K. Kim and V. V. Varadan, "Electrically small, millimeter wave dual band meta-resonator antennas," IEEE Trans. Antennas Propag., vol. 58, no. 11, pp. 3458–3463, 2010.

[110] M.-C. Tang, S. Xiao, T. Deng, D. Wang, J. Guan, B. Wang, and G.-D. Ge, "Compact UWB antenna with multiple band-notches for WiMAX and WLAN," IEEE Trans. Antennas Propag., vol. 59, no. 4, pp. 1372–1376, 2011.

[111] P. Jin and R. W. Ziolkowski, "Multi-frequency, linear and circular polarized, metamaterial-inspired, near-field resonant parasitic antennas," IEEE Trans. Antennas Propag., vol. 59, no. 5, pp. 1446–1459, 2011.

[112] R. W. Ziolkowski, P. Jin, and C.-C. Lin, "Metamaterial-inspired engineering of antennas," Proc. IEEE, vol. 99, no. 10, pp. 1720–1731, 2011.

[113] C.-C. Lin, P. Jin, and R. W. Ziolkowski, "Single, dual and tri-band-notched ultrawideband (UWB) antennas using capacitively loaded loop (CLL) resonators," IEEE Trans. Antennas Propag., vol. 60, no. 1, pp. 102–109, 2012.

[114] Y. Dong and T. Itoh, “Metamaterial-based antennas,” Proc. IEEE, vol. 100, no. 7, pp. 2271–2285, 2012.

[115] O. Turkmen, G. Turhan-Sayan, and R. W. Ziolkowski, “Metamaterial inspired, electrically small, GSM antenna with steerable radiation patterns and high radiation efficiency,” Proc. of the 2013 IEEE AP-S International Symposium, Orlando, FL, 2013, pp. 770-771.

[116] H. Chen and C. T. Chan, “Acoustic cloaking in three dimensions using acoustic metamaterials,” Appl. Phys. Lett., vol. 91, no. 18, pp. 183518(1)-(3), 2007.

[117] W. Cai, U. K. Chettiar, A. V. Kildishev, and V. M. Shalaev, “Optical cloaking with metamaterials,” Nat. Photonics, vol. 1, no. 4, pp. 224–227, 2007.

[118] P. Alitalo and S. Tretyakov, “Electromagnetic cloaking with metamaterials,” Mater. Today, vol. 12, no. 3, pp. 22–29, 2009.

[119] J. Valentine, J. Li, T. Zentgraf, G. Bartal, and X. Zhang, “An optical cloak made of dielectrics,” Nat. Mater., vol. 8, no. 7, pp. 568–571, 2009.

[120] J. Hao, W. Yan, and M. Qiu, “Super-reflection and cloaking based on zero index metamaterial,” Appl. Phys. Lett., vol. 96, no. 10, pp. 101109(1)-(3), 2010.

[121] A. Alù and N. Engheta, “Cloaking a receiving antenna or a sensor with plasmonic metamaterials,” Metamaterials, vol. 4, no. 2–3, pp. 153–159, 2010.

[122] S. Hrabar, I. Krois, and A. Kiricenko, “Towards active dispersionless ENZ metamaterial for cloaking applications,” Metamaterials, vol. 4, no. 2–3, pp. 89–97, 2010.

[123] P. Alitalo and C. A. Valagiannopoulos, “Demonstration of electromagnetic cloaking of conducting object by dielectric material cover,” Electron. Lett., vol. 48, no. 17, pp. 1056–1057, 2012.

[124] D. Rainwater, A. Kerkhoff, K. Melin, J. C. Soric, G. Moreno, and A. Alù, “Experimental verification of three-dimensional plasmonic cloaking in free-space,” New J. Phys., vol. 14, no. 1, pp. 013054(1)-(13), 2012.

[125] S. V. Savić, A. B. Manić, M. M. Ilić, and B. M. Notaroš, “Efficient higher order full-wave numerical analysis of 3-D cloaking structures,” Plasmonics, vol. 8, no. 2, pp. 455–463, 2012.

[126] N. Cohen, “Body-sized wideband high fidelity invisibility cloak,” Fractals, vol. 20, no. 03n04, pp. 227–232, 2012.

[127] T. Ergin, J. Fischer, and M. Wegener, “Detailed optical characterization of three-dimensional visible-frequency polarization-independent carpet invisibility cloak,” Phys. B Condens. Matter, vol. 407, no. 20, pp. 4075–4077, 2012.

[128] M. Danaeifar, M. Kamyab, and A. Jafargholi, “Broadband cloaking with transmission-line networks and metamaterial,” Int. J. RF Microw. Comput.-Aided Eng., vol. 22, no. 6, pp. 663–668, 2012.

[129] S. Xu, X. Cheng, S. Xi, R. Zhang, H. O. Moser, Z. Shen, Y. Xu, Z. Huang, X. Zhang, F. Yu, B. Zhang, and H. Chen, “Experimental demonstration of a free-space cylindrical cloak without superluminal propagation,” Phys. Rev. Lett., vol. 109, no. 22,pp. 223903(1)-(5), 2012.

[130] Y. Wu and J. Li, “Total reflection and cloaking by zero index metamaterials loaded with rectangular dielectric defects,” Appl. Phys. Lett., vol. 102, no. 18, pp. 183105(1)-(4), 2013.

[131] J. B. Pendry, “Negative refraction makes a perfect lens,” Phys. Rev. Lett., vol. 85, no. 18, pp. 3966-3969, 2000.

[132] S. A. Ramakrishna, J. B. Pendry, M. C. K. Wiltshire, and W. J. Stewart, “Imaging the near field,” J. Mod. Opt., vol. 50, no. 9, pp. 1419–1430, 2003.

[133] J. Pendry, “Comment on ‘Left-handed materials do not make a perfect lens,” Phys. Rev. Lett., vol. 91, no. 9,pp. 099701(1), 2003.

[134] A. N. Lagarkov and V. Kissel, “Near-perfect imaging in a focusing system based on a left-handed-material plate,” Phys. Rev. Lett., vol. 92, no. 7, pp. 77401(1)-(4), 2004.

[135] A. Grbic and G. Eleftheriades, “Overcoming the diffraction limit with a planar left-handed transmission-line lens,” Phys. Rev. Lett., vol. 92, no. 11, pp. 117403(1)-(4), 2004.

[136] N. Fang, H. Lee, C. Sun, and X. Zhang, “Sub–diffraction-limited optical imaging with a silver superlens,” Science, vol. 308, pp. 534-537, 2005.

[137] F. Mesa, M. J. Freire, R. Marqués, and J. Baena, “Three-dimensional superresolution in metamaterial slab lenses: experiment and theory,” Phys. Rev. B, vol. 72, no. 23, pp. 235117(1)-(6), 2005.

[138] P. A. Belov, Y. Hao, and S. Sudhakaran, “Subwavelength microwave imaging using an array of parallel conducting wires as a lens,” Phys. Rev. B, vol. 73, no. 3, pp. 033108(1)-(4), 2006.

[139] A. O. Pinchuk and G. C. Schatz, “Focusing a beam of light with left-handed metamaterials,” Solid-State Electron., vol. 51, no. 10, pp. 1381–1386, 2007.

[140] C. Imhof and R. Zengerle, “Strong birefringence in left-handed metallic metamaterials,” Opt. Commun., vol. 280, no. 1, pp. 213–216, 2007.

[141] X. Zhang and Z. Liu, “Superlenses to overcome the diffraction limit,” Nat. Mater., vol. 7, no. 6, pp. 435–441, 2008.

[142] W. X. Jiang, J. Y. Chin, and T. J. Cui, “Anisotropic metamaterial devices,” Mater. Today, vol. 12, no. 12, pp. 26–33, 2009.

[143] S. Guenneau and S. A. Ramakrishna, “Negative refractive index, perfect lenses and checkerboards: Trapping and imaging effects in folded optical spaces,” Comptes Rendus Phys., vol. 10, no. 5, pp. 352–378, 2009.

[144] N. Kundtz and D. R. Smith, “Extreme-angle broadband metamaterial lens,” Nat. Mater., vol. 9, no. 2, pp. 129–132, 2009.

[145] M. J. Freire, L. Jelinek, R. Marques, and M. Lapine, “On the applications of μ_r = -1 metamaterial lenses for magnetic resonance imaging,” J. Magn. Reson., vol. 203, no. 1, pp. 81–90, 2010.

[146] B.-R. Lu, Y. Chen, S.-W. Wang, E. Huq, E. Rogers, T. S. Kao, X.-P. Qu, R. Liu, and N. I. Zheludev, “A novel 3D nanolens for sub-wavelength focusing by self-aligned nanolithography,” Microelectron. Eng., vol. 87, no. 5–8, pp. 1506–1508, 2010.

[147] M. Navarro-Cía, M. Beruete, M. Sorolla, and I. Campillo, “Viability of focusing effect by left-handed stacked subwavelength hole arrays,” Phys. B Condens. Matter, vol. 405, no. 14, pp. 2950–2954, 2010.

[148] T. A. Morgado and M. G. Silveirinha, “Focusing of electromagnetic radiation by a flat slab of a crossed wire mesh metamaterial,” Metamaterials, vol. 4, no. 2–3, pp. 112–118, 2010.

[149] M. Navarro-Cía, M. Beruete, I. Campillo, and M. Sorolla, “Fresh metamaterials ideas for metallic lenses,” Metamaterials, vol. 4, no. 2–3, pp. 119–126, 2010.

[150] D. Shreiber, M. Gupta, and R. Cravey, “Comparative study of 1-D and 2-D metamaterial lens for microwave nondestructive evaluation of dielectric materials,” Sens. Actuators Phys., vol. 165, no. 2, pp. 256–260, 2011.

[151] J. M. Algarín, M. J. Freire, and R. Marqués, “Comparative analysis of the transfer function of closed and open split-ring metamaterial slab lenses,” Metamaterials, vol. 5, no. 2–3, pp. 107–111, 2011.

[152] S. Xiao, Q. He, X. Huang, and L. Zhou, "Super imaging with a plasmonic metamaterial: Role of aperture shape," Metamaterials, vol. 5, no. 2–3, pp. 112–118, 2011.

[153] F. Chen, X. Wang, and E. Semouchkina, "Formation of resonance states due to interaction between resonators in arrays used in dielectric metamaterials," Microw. Opt. Technol. Lett., vol. 54, no. 3, pp. 555–560, 2012.

[154] N. Liu and H. Giessen, "Coupling Effects in Optical Metamaterials," Angew. Chem. Int. Ed., vol. 49, no. 51, pp. 9838–9852, 2010.

[155] R. S. Penciu, K. Aydin, M. Kafesaki, T. Koschny, E. Ozbay, E. N. Economou, and C. M. Soukoulis, "Multi-gap individual and coupled split-ring resonator structures," Opt Express, vol. 16, no. 22, pp. 18131–18144, 2008.

[156] D. R. Chowdhury, R. Singh, M. Reiten, J. Zhou, A. J. Taylor, and J. F. O'Hara, "Tailored resonator coupling for modifying the terahertz metamaterial response," Opt Express, vol. 19, no. 11, pp. 10679-10685, 2001.

[157] CST STUDIO SUITE^{TM} , CST AG, Germany, www.cst.com, (accessed 2014).

[158] D. R. Smith, D. C. Vier, N. Kroll, and S. Schultz, "Direct calculation of permeability and permittivity for a left-handed metamaterial," Appl. Phys. Lett., vol. 77, no. 14, pp. 2246–2248, 2000.

[159] D. R. Smith and J. B. Pendry, "Homogenization of metamaterials by field averaging," J. Opt. Soc. Am. B, vol. 23, no. 3, pp. 391–403, 2006.

[160] O. Acher, J.-M. Lerat, and N. Mallějac, "Evaluation and illustration of the properties of Metamaterials using field summation," Opt Express, vol. 15, no. 3, pp. 1096-1106, 2007.

[161] G. Lubkowski, R. Schuhmann, and T. Weiland, "Extraction of effective metamaterial parameters by parameter fitting of dispersive models," Microw. Opt. Technol. Lett., vol. 49, no. 2, pp. 285–288, 2007.

[162] A. M. Nicolson and G. F. Ross, "Measurement of the intrinsic properties of materials by time-domain techniques," IEEE Trans. Instrum. Meas., vol. IM-19, no. 4, pp. 377–382, 1970.

[163] W. B. Weir, "Automatic measurement of complex dielectric constant and permeability at microwave frequencies," Proc. IEEE, vol. 62, no. 1, pp. 33–36, 1974.

[164] D. K. Ghodgaonkar, V. V. Varadan, and V. K. Varadan, “Free-space measurement of complex permittivity and complex permeability of magnetic materials at microwave frequencies,” IEEE Trans. Instrum. Meas., vol. 39, no. 2, pp. 387–394, 1990.

[165] S. O’brien and J. B. Pendry, “Magnetic activity at infrared frequencies in structured metallic photonic crystals,” J. Phys. Condens. Matter, vol. 14, no. 25, pp. 6383-6394, 2002.

[166] D. R. Smith, S. Schultz, P. Markos and C. M. Soukoulis “Determination of effective permittivity and permeability of metamaterials from reflection and transmission coefficients,” Phys. Rev. B, vol. 65, no. 19, pp. 195104(1)-(5), 2002.

[167] X. Chen, T. M. Grzegorczyk, B.-I. Wu, J. Pacheco, Jr., and J. A. Kong, “Robust method to retrieve the constitutive effective parameters of metamaterials,” Phys. Rev. E, vol. 70, no. 1, pp. 016608(1)-(7), 2004.

[168] X. Chen, B.-I. Wu, J. A. Kong, and T. M. Grzegorczyk, “Retrieval of the effective constitutive parameters of bianisotropic metamaterials,” Phys. Rev. E, vol. 71, no. 4, pp. 46610(1)-(9), 2005.

[169] D. R. Smith, D. Schurig, and J. J. Mock, “Characterization of a planar artificial magnetic metamaterial surface,” Phys. Rev. E, vol. 74, no. 3, pp. 36604(1)-(5), 2006.

[170] V. V. Varadan and R. Ro, “Unique retrieval of complex permittivity and permeability of dispersive materials from reflection and transmitted fields by enforcing causality,” IEEE Trans. Microw. Theory Tech., vol. 55, no. 10, pp. 2224–2230, 2007.

[171] L. Li Hou, J. Y. Chin, X. M. Yang, X. Q. Lin, R. Liu, F. Y. Xu, and T. J. Cui, “Advanced parameter retrievals for metamaterial slabs using an inhomogeneous model,” J. Appl. Phys., vol. 103, no. 6, pp. 064904(1)-(6), 2008.

[172] C. Menzel, C. Rockstuhl, T. Paul, F. Lederer, and T. Pertsch, “Retrieving effective parameters for metamaterials at oblique incidence,” Phys. Rev. B, vol. 77, no. 19, pp. 195328(1)-(8), 2008.

[173] Z. Li, K. Aydin, and E. Ozbay, “Determination of the effective constitutive parameters of bianisotropic metamaterials from reflection and transmission coefficients,” Phys. Rev. E, vol. 79, no. 2, pp.026610(1)-(7), 2009.

[174] J. Qi, H. Kettunen, H. Wallen, and A. Sihvola, “Compensation of Fabry–Pérot resonances in homogenization of dielectric composites,” IEEE Antennas Wirel. Propag. Lett., vol. 9, pp. 1057–1060, 2010.

[175] C. R. Simovski and S. A. Tretyakov, “Local constitutive parameters of metamaterials from an effective-medium perspective,” Phys. Rev. B, vol. 75, no. 19, pp. 195111(1)-(10), 2007.

[176] A. I. Căbuz, D. Felbacq, and D. Cassagne, “Spatial dispersion in negative-index composite metamaterials,” Phys. Rev. A, vol. 77, no. 1, pp. 013807(1)-(11), 2008.

[177] A. Alù, “Restoring the physical meaning of metamaterial constitutive parameters,” Phys. Rev. B, vol. 83, no. 8, pp. 081102(1)-(4), 2011.

[178] G. Turhan-Sayan and O. Turkmen, “Effects of having dense metamaterial arrays on the retrieved parameter results for permittivity and permeability,” IEEE International Symposium on Antennas and Propagation and USNC-URSI National Radio Science Meeting, Chicago, USA, 2012, paper no: IF13.6.

[179] A. Alù, A. D. Yaghjian, R. A. Shore, and M. G. Silveirinha, “Causality relations in the homogenization of metamaterials,” Phys. Rev. B, vol. 84, no. 5, pp. 054305(1)-(16), 2011.

[180] A. Alù, “First-principles homogenization theory for periodic metamaterials,” Phys. Rev. B, vol. 84, no. 7, pp. 075153(1)-(18), 2011.

[181] Y. Yuan, C. Bingham, T. Tyler, S. Palit, T. H. Hand, W. J. Padilla, N. M. Jokerst, and S. A. Cummer, “A dual-resonant terahertz metamaterial based on single-particle electric-field-coupled resonators,” Appl. Phys. Lett., vol. 93, no. 19, pp. 191110(1)-(3), 2008.

[182] D. R. Chowdhury, R. Singh, M. Reiten, H.-T. Chen, A. J. Taylor, J. F. O’Hara, and A. K. Azad, “A broadband planar terahertz metamaterial with nested structure,” Opt. Express, vol. 19, no. 17, pp. 15817–15823, 2011.

[183] R. H. Geschke, B. Jokanovic, and P. Meyer, “Compact triple-band resonators using multiple split-ring resonators,” Proceedings of the 39th European Microwave Conference, Rome, Italy, 2009, pp. 366–369.

[184] O. Yurduseven, A. E. Yilmaz, and G. Turhan-Sayan, “Triangular-shaped single-loop resonator: a triple-band metamaterial with MNG and ENG regions in S/C bands,” IEEE Antennas Wirel. Propag. Lett., vol. 10, pp. 701–704, 2011.

[185] O. Yurduseven, A. E. Yilmaz, and G. Turhan-Sayan, “Hybrid-shaped single-loop resonator: a four-band metamaterial structure,” Electron. Lett., vol. 47, no. 25, pp. 1381–1382, 2011.

[186] H. Chen, L. Ran, J. Huangfu, X. Zhang, K. Chen, T. M. Grzegorczyk, and J. A. Kong, “Metamaterial exhibiting left-handed properties over multiple frequency bands,” J. Appl. Phys., vol. 96, no. 9, pp. 5338–5340, 2004.

[187] J. Wang, S. Qu, Y. Yang, H. Ma, X. Wu, and Z. Xu, “Multiband left-handed metamaterials,” Appl. Phys. Lett., vol. 95, no. 1, pp. 014105(1)-(3), 2009.

[188] C. Zhu, J.-J. Ma, L. Li, and C.-H. Liang, “Multiresonant metamaterial based on asymmetric triangular electromagnetic resonators,” IEEE Antennas Wirel. Propag. Lett., vol. 9, pp. 99–102, 2010.

[189] O. Turkmen, E. Ekmekci, and G. Turhan-Sayan, “Effects of using different boundary conditions and computational domain dimensions on modeling and simulations of periodic metamaterial arrays in microwave frequencies,” Int. J. RF Microw. Comput.-Aided Eng., vol. 23, no. 4, pp. 459-465, 2013.

[190] O. Turkmen, G. Turhan-Sayan, and R. W. Ziolkowski, “Single-, dual- and triple-band metamaterial-inspired electrically small planar magnetic dipole antennas,” Microw. Opt. Technol. Lett., vol. 56, no. 1, pp. 83–87, 2014.

[191] O. Turkmen, E. Ekmekci, and G. Turhan-Sayan, “Effects of using different boundary conditions and computational domain dimensions on modelling and simulations of metamaterial arrays in microwave frequencies,” 12th Mediterranean Microwave Symposium (MMS 2012), 2012, Istanbul, Turkey.

[192] C. Caloz and T. Itoh, “Electromagnetic Metamaterials: Transmission Line Theory and Microwave Applications,” 1st ed. John Wiley & Sons Inc, 2005.

[193] N. Engheta and R. W. Ziolkowski, “A positive future for double-negative metamaterials,” IEEE Trans. Microw. Theory Tech., vol. 53, no. 4, pp. 1535–1556, 2005.

[194] R. W. Ziolkowski, “Metamaterial-based antennas: research and developments,” IEICE Trans. Electron., vol. E89–C, no. 9, pp. 1267–1275, 2006.

[195] J.-M. Lourtioz, H. Benisty, V. Berger, J.-M. Gerard, D. Maystre, and A. Tchelnokov, “Photonic crystals: : towards nanoscale photonic devices,” Second Edition. Springer, 2008.

[196] R. Marqués, J. Martel, F. Mesa, and F. Medina, “Left-handed-media simulation and transmission of EM waves in subwavelength split-ring-resonator-loaded metallic waveguides,” Phys. Rev. Lett., vol. 89, no. 18, pp. 183901(1)-(4), 2002.

[197] F. Zhang, Q. Zhao, J. Sun, J. Zhou, and D. Lippens, “Coupling effect of split ring resonator and its mirror image,” Prog. Electromagn. Res., vol. 124, pp. 233–247, 2012.

[198] E. Ekmekci and G. Turhan-Sayan, "Multi-functional metamaterial sensor based on a broad-side coupled SRR topology with a multi-layer substrate," Appl. Phys. A, vol. 110, no. 1, pp. 189–197, 2012.

[199] D. R. Smith, D. C. Vier, Th. Koschny, and C. M. Soukoulis, "Electromagnetic parameter retrieval from inhomogeneous metamaterials," Phys. Rev. E, vol. 71, no. 3, pp. 36617(1)-(11), 2005.

[200] T. Koschny, P. Markoš, D. R. Smith, and C. M. Soukoulis, "Resonant and antiresonant frequency dependence of the effective parameters of metamaterials," Phys. Rev. E, vol. 68, no. 6, pp. 65602(1)-(4), 2003.

[201] T. Koschny, P. Markoš, D. R. Smith, and C. M. Soukoulis, "Reply to comments on " Resonant and antiresonant frequency dependence of the effective parameters of metamaterials"," Phys. Rev. E, vol. 70, no. 4, pp. 048603(1), 2004.

[202] J. Woodley and M. Mojahedi, "On the signs of the imaginary parts of the effective permittivity and permeability in metamaterials," J. Opt. Soc. Am. B, vol. 27, no. 5, pp. 1016–1021, 2010.

[203] S. Arslanagić, T. V. Hansen, N. A. Mortensen, A. H. Gregersen, O. Sigmund, R. W. Ziolkowski and O. Breinbjerg, "A review of the scattering parameter extraction method with clarification of ambiguity issues in relation to metamaterial homogenization," arXiv:1206.4801, 2012.

[204] J. J. Barroso and U. C. Hasar, "Constitutive parameters of a metamaterial slab retrieved by the phase unwrapping method," J. Infrared Milli. Terahertz Waves, vol. 33, no. 2, pp. 237–244, 2012.

[205] R. Liu, T. J. Cui, D. Huang, B. Zhao, and D. R. Smith, "Description and explanation of electromagnetic behaviors in artificial metamaterials based on effective medium theory," Phys. Rev. E, vol. 76, no. 2, pp. 026606(1)-(8), 2007.

[206] R. Marques, F. Mesa, J. Martel, and F. Medina, "Comparative analysis of edge- and broadside-coupled split ring resonators for metamaterial design - theory and experiments," IEEE Trans. Antennas Propag., vol. 51, no. 10, pp. 2572–2581, 2003.

[207] M. Kafesaki, T. Koschny, R. S. Penciu, T. F. Gundogdu, E. N. Economou, and C. M. Soukoulis, "Left-handed metamaterials: detailed numerical studies of the transmission properties," J. Opt. A: Pure Appl. Opt., vol. 7, no. 2, pp. S12–S22, 2005.

[208] M. T. Thompson, "M. T. Thompson. Inductance calculation techniques—Part II: Approximations and handbook methods," Power Contr Intell Motion Online, available at http://www.thompsonrd.com/induct2.pdf.

[209] N. P. Johnson, A. Z. Khokhar, H. M. H. Chong, R. M. De La Rue, and S. McMeekin, "Characterisation at infrared wavelengths of metamaterials formed by thin-film metallic split-ring resonator arrays on silicon," Electron. Lett., vol. 42, no. 19, pp. 1117–1119, 2006.

[210] S. G. McMeekin, A. Z. Khokhar, B. Lahiri, M. Richard, and N. P. Johnson, "Analysis of resonant responses of split ring resonators using conformal mapping techniques," in International Congress on Optics and Optoelectronics, vol. 6881, 2007.

[211] I. A. I. Al-Naib, C. Jansen, and M. Koch, "Miniaturized bandpass filter based on metamaterial resonators: a conceptual study," J. Phys. D: Appl. Phys., vol. 41, no. 20, pp. 205002(1)-(4), 2008.

[212] J. Garcia-Garcia, F. Martin, F. Falcone, J. Bonache, J. D. Baena, I. Gil, E. Amat, T. Lopetegi, M. A. G. Laso, J. A. M. Iturmendi, M. Sorolla, and R. Marques, "Microwave filters with improved stopband based on sub-wavelength resonators," IEEE Trans. Microw. Theory Tech., vol. 53, no. 6, pp. 1997–2006, 2005.

[213] J. Ghalibafan, A. R. Attari, and F. H. Kashani, "A new dual-band microstrip antenna with U-shaped slot," Prog Electromagn Res C, vol. 12, pp. 215-223, 2010.

[214] H. Benosman and N. Boukli Hacene, "Multi-band meta-material structures based on hexagonal shaped magnetic resonators," Int. J. Phys. Sci., vol. 8, no. 17, pp. 803–808, 2013.

[215] C. Sabah, "Multiband metamaterials based on multiple concentric open-ring resonators topology," IEEE J. Sel. Top. Quantum Electron., vol. 19, no. 1, pp. 8500808(1)-(8), 2013.

[216] N. Engheta and R. W. Ziolkowski, "Metamaterials: Physics and Engineering Explorations," Wiley-IEEE Press, 2006.

[217] Y. Zhang, W. Hong, C. Yu, Z.-Q. Kuai, Y.-D. Don, and J.-Y. Zhou, "Planar ultrawideband antennas with multiple notched bands based on etched slots on the patch and/or split ring resonators on the feed line," IEEE Trans. Antennas Propag., vol. 56, no. 9, pp. 3063–3068, 2008.

[218] C. Icheln, J. Krogerus, and P. Vainikainen, "Use of balun chokes in small-antenna radiation measurements," IEEE Trans. Instrum. Meas., vol. 53, no. 2, pp. 498–506, 2004.

[219] S. Pivnenko, J. Zhang, A. Khatun, T. Laitinen, and J. Carlsson, "Characterization of small antennas for hearing aids by several measurement techniques," in

Antennas and Propagation (EuCAP), 2010 Proceedings of the Fourth European Conference on, 2010, pp. 1–5.

[220] M.-C. Tang and R. W. Ziolkowski, “A study of low-profile, broadside radiation, efficient, electrically small antennas based on complementary split ring resonators,” IEEE Trans. Antennas Propag., vol. 61, no. 9, pp. 4419–4430, 2013.

[221] C. Icheln, M. Popov, P. Vainikainen, and S. He, “Optimal reduction of the influence of RF feed cables in small antenna measurements,” Microw Opt Technol Lett, vol. 25, no. 3, pp. 194-196, 2000.

VITA

PERSONAL INFORMATION

Surname, Name: (Türkmen) Küçüksarı, Öznur

Nationality: Turkish (TC)

Date and Place of Birth: 20 April 1981 , Malatya

email: oturkmen@metu.edu.tr, oznurturkmen@gmail.com

EDUCATION

Degree	**Institution**	**Year of Graduation**
M.Sc.	Yildiz Technical University, İstanbul Electronics & Telecommunications Engineering	2005
B.S	Yildiz Technical University, İstanbul Electronics & Telecommunications Engineering	2001
High School	H. Ahmet Akıncı Lisesi, Malatya	1997

WORK EXPERIENCE

Year	Place	Enrollment
2005-present	Middle East Technical University Dept. of Electrical and Electronics Engineering	Research Assistant
2012-2013	The University of Arizona, Arizona Dept. of Electrical and Computer Engineering Electromagnetics Laboratory	Visiting Researcher
07-09/2000	Türk Telekom, İstanbul (Turkey's Telecommunication Leaders)	Trainee
07-09/1999	Türk Telekom, İstanbul (Turkey's Telecommunication Leaders)	Trainee

PUBLICATIONS

International Refereed Journal Papers

1. **O. Turkmen**, E. Ekmekci, and G. Turhan-Sayan, "Nested U-ring resonators: a novel multi-band metamaterial design in microwave region," IET Microw. Antennas Propag., vol. 6, no. 10, pp. 1102-1108, 2012.

2. **O. Turkmen**, E. Ekmekci, and G. Turhan-Sayan, "Effects of using different boundary conditions and computational domain dimensions on modeling and simulations of periodic metamaterial arrays in microwave frequencies," Int. J. RF Microw. Comput.-Aided Eng., vol. 23, no. 4, pp. 459-465, 2013.

3. **O. Turkmen**, G. Turhan-Sayan, and R. W. Ziolkowski, “Single-, dual- and triple-band metamaterial-inspired electrically small planar magnetic dipole antennas,” Microw. Opt. Technol. Lett., vol. 56, no. 1, pp. 83–87, 2014

4. C. Sabah, **O. Turkmen-Kucuksari** and G. Turhan-Sayan, ” Metamaterial absorber-based sensor embedded into X-band waveguide,” Electronics Letters, vol. 50, no. 15, pp. 1074 – 1076, 2014.

International Refereed Conference Papers

1. **O. Turkmen**, E. Ekmekci, and G. Turhan-Sayan, “A new multi-ring SRR type metamaterial design with multiple magnetic resonances,” Progress In Electromagnetics Research Symposium Proceedings (PIERS), Marrakesh, Morocco, 2011, pp. 315-319.

2. **O. Turkmen,** E. Ekmekci, and G. Turhan-Sayan, “Parametric investigation of a new multi-band metamaterial design: U-shaped multiple ring magnetic resonators,” 2011 IEEE International Symposium on Antennas and Propagation (APSURSI), Spokane, USA, 2011, pp. 1516–1518.

3. **O. Turkmen**, E. Ekmekci, and G. Turhan-Sayan, “Miniaturization of U-shaped multi-band metamaterial structures,” 2011 XXXth URSI General Assembly and Scientific Symposium , Istanbul, Turkey, 2011, pp. 1–4.

4. G. Turhan-Sayan and **O. Turkmen**, “Effects of Having Dense Metamaterial Arrays on the Retrieved Parameter Results for Permittivity and Permeability,” IEEE International Symposium on Antennas and Propagation and USNC-URSI National Radio Science Meeting, Chicago, USA, 2012, paper no: IF13.6.

5. **O. Turkmen**, E. Ekmekci, G. Turhan-Sayan, "Effects of Using Different Boundary Conditions and Computational Domain Dimensions on Modelling and Simulations

of Metamaterial Arrays in Microwave Frequencies," 12th Mediterranean Microwave Symposium (MMS 2012), Istanbul, Turkey, September 2012.

6. **O. Turkmen**, G. Turhan-Sayan, and R. W. Ziolkowski, “Metamaterial inspired, electrically small, GSM antenna with steerable radiation patterns and high radiation efficiency,” IEEE AP-S International Symposium, Orlando, FL, 2013, pp. 770-771.

National Refereed Conference Papers (In Turkish)

1. **O. Turkmen** and G. Turhan-Sayan, “İç İçe Geçmiş Çok Halkalı Çok Bantlı Metamalzeme Rezonatörleri”, VII. URSI-Türkiye'2014 Bilimsel Kongresi, Elazığ, Turkey, Agust 2014, ID No. 12**.** (accepted)